

# **The FANDECT: Design of a Fixed-Wing Aircraft Networked with Deployable Engines for Cargo Transport**

a project presented to  
The Faculty of the Department of Aerospace Engineering  
San José State University

in partial fulfillment of the requirements for the degree  
*Master of Science in Aerospace Engineering*

by

**Glen Gieser**

December 2018

approved by

Dr. Jeanine Hunter  
Faculty Advisor



# The FANDECT: Design of a Fixed-Wing Aircraft Networked with Deployable Engines for Cargo Transport

Glen Gieser

*Student, San Jose State University, San Jose, CA 95192*

Jeanine Hunter

*Project Advisor, Professor, San Jose State University, San Jose, CA 95192*

The FANDECT is a fixed wing electric aircraft capable of deploying and retrieving multi-role engines that may operate as independent VTOL cargo delivery aircraft. The design benefits from the use of various subsystems operating independently to achieve a flight profile that minimizes the range penalty associated with rotary wing aircraft and the maneuverability penalty associated with fixed wing aircraft. The majority of the aircraft remains in flight while one propulsion unit vertically descends to deliver a package prior to returning to the aircraft. The result is a long range aircraft capable of delivering a lightweight package to an area large enough for a person to stand in.

**Keywords:** networked subsystems, autonomous flight, fixed wing, VTOL, contra-rotating, detachable propulsion system, electric, multi-motor, inflight recharging, endurance, drone delivery, small payload, PixyCam, Raspberry Pi, 3D printing

## Nomenclature

Symbol	Definition	Units
A	current, electric	A
d	diameter	m
E	endurance, time	hr
EB*	specific energy, FF battery	(W hr/kg)
f	fraction	---
g	gravity constant	9.81 m/s <sup>2</sup>
h	height above MSL	m
I	current, electric	A
kV	brushless motor constant	RPM/V
L/D	Lift to Drag ratio	---
mA	milliamper	mA
mAh	milliamp-hours	mAh
m	mass	kg
P	power	W
RPM	Rotations Per Minute	rotations/min
r	radius	m
T	thrust	N
V	volts	V

<b>Symbol</b>	<b>Definition</b>	<b>Units</b>
v	velocity	m/s
W	weight	N
Greek Symbols		
$\alpha$	angle of attack	degrees
$\eta$	efficiency	---
$\rho$	density	kg/m <sup>3</sup>
Subscripts		
( ) <sub>∞</sub>	freestream	---
( ) <sub>c</sub>	constant	---
( ) <sub>cl</sub>	climb	---
( ) <sub>cr</sub>	cruise	---
( ) <sub>m</sub>	motor	---
( ) <sub>mc</sub>	microcomputer	---
( ) <sub>prop</sub>	FR propeller	---
( ) <sub>res</sub>	contingency reserve	---
( ) <sub>s</sub>	servo	---
( ) <sub>TO</sub>	takeoff	---
Acronyms		
AALN	Autonomous Aerial Logistics Network	---
ABS	Acrylonitrile-Butadiene Styrene	---
AGL	Above Ground Level	---
AR	Wing, Aspect Ratio	---
ARM	Advanced RISC Machine	---
AWG	diameter, wire, American Wire Gauge	---
BLDC	BrushLess DC	---
CAD	Computer Aided Design	---
CG	Center of Gravity	---
CP	Concept Phase	---
CPU	Central Processing Unit	---
DARPA	Defense Advanced Research Projects Agency	---
EM	ElectroMagnetic	---
ESC	Electronic Speed Control	---
FANDECT	Fixed-wing Aircraft Networked with Deployable Engines for Cargo Transport	---
FDM	Fused Deposition Modeling	---
FF	FANDECT-Fixed wing main system	---
FOSA	FR, total amperage Factor of Safety	---

<b>Symbol</b>	<b>Definition</b>	<b>Units</b>
FR	FANDECT-Rotary wing subsystem	---
GPIO	General Purpose Input/Output	---
GPS	Global Positioning System	---
HP03	Helios Prototype 03	---
IDE	Integrated Development Environment	---
IDLE	Integrated Development and Learning Environment	---
IFR	Instrument Flight Rules	---
ILS	Instrument Landing System	---
LEAPTech	Leading Edge Asynchronous Propeller Technology	---
LiPo	Lithium Polymer	---
LoRa	Long Range	---
LOS	Line Of Sight	---
LZ	Landing Zone	---
MSL	Mean Sea Level	---
MTOW	Maximum TakeOff Weight	---
NASA	National Aeronautics and Space Administration	---
NDB	Non-Directional Beacon	---
OGE	Out of Ground Effect	---
OS	Operating System	---
PDB	Power Distribution Board	---
PIXEL	Pi Improved Xwindows Environment Lightweight	---
PL	PayLoad	---
PLA	PolyLactic Acid	---
PP	Production Phase	---
PWM	Pulse Width Modulation	---
RISC	Reduced Instruction Set Computing	---
RP	Release Point	---
SEM	Scanning Electron Microscope	---
SoC	System On a Chip	---
SSH	Secure SHell	---
VFR	Visual Flight Rules	---
VHF	Very High Frequency	---
VOR	VHF Omni-directional Range	---
VTOL	Vertical TakeOff and Landing	---

## Table of Contents

<b>1. INTRODUCTION</b>	1
1.1 CONTEXT & BACKGROUND	1
1.1.1 Context	1
1.1.2 Background	1
1.1.2.1 Hybrid aircraft (VTOL)	1
1.1.2.2 Re-evaluating VTOL usage	1
1.2 PROBLEM DEFINITION & APPROACH	2
1.2.1 F-F Design	2
1.2.2 F-R Design	2
1.2.2.1 Dependent flight mode	2
1.2.2.2 Autonomous flight mode	2
1.2.3 Aircraft Subsystem Network	3
1.3 SOCIAL INTENT	3
1.3.1 Stage 1: Corridor Designation	3
1.3.2 Stage 2: Fleet Deployment	3
1.3.3 Stage 3: Autonomous Aerial Logistics Network	3
<b>2. RESEARCH &amp; PLANNING</b>	4
2.1 LITERATURE REVIEW	4
2.1.1 Comparative Study of Similar Aircraft	4
2.1.1.1 DARPA VTOL X-Plane	5
2.1.1.2 DARPA Tern	5
2.1.1.3 NASA X-57 Maxwell	6
2.1.1.4 Schleicher ASH 31	7
2.1.1.5 Consortium Eta	8
2.1.1.6 NASA HP03	9
2.1.1.7 Solar Impulse HB-SIA	10
2.1.2 FR Technical Research	11
2.1.3 Hazardous Material Research	12
2.2 PROJECT OBJECTIVE	13
2.3 METHODOLOGY	13
2.3.1 Mission Specification	13
2.3.1.1 Mission requirements	13
2.3.1.2 Mission profile	14
2.3.1.3 Market analysis	14
2.3.1.4 Technical analysis	14
2.3.1.5 Operational analysis	14
2.3.2 Production Phases	14
2.3.3 Concept Phases	15
2.3.3.1 FR progression	15
2.3.3.2 FANDECT progression	15

<b>3. FR SUBSYSTEM</b>	16
3.1 DESCRIPTION	16
3.2 MISSION REQUIREMENTS & CONFIGURATION	16
3.2.1 Mission Requirements	16
3.2.2 Configuration	16
3.3 DESIGN & FUNCTIONALITY	17
3.3.1 Components	17
3.3.1.1 Structure	17
3.3.1.2 Propeller	17
3.3.1.3 Power	17
3.3.1.4 Motor	18
3.3.1.5 Data & signals processing	19
3.3.1.6 Control flaps	20
3.3.1.7 Software	20
3.3.2 CG	20
3.3.3 Control	20
3.3.3.1 Vertical axis control	21
3.3.3.2 Vertical off axis control	21
3.3.4 Docking Guidance & Payload Drop Off	21
3.3.4.1 Stage 1: Beacon homing	21
3.3.4.2 Stage 2: Visual homing	21
3.3.4.3 Stage 3: EM docking	22
3.3.4.4 Post docking	22
3.3.4.5 Payload drop off	22
3.4 PRODUCTION	22
3.4.1 Computer Aided Design	22
3.4.2 Machine Code Generation	23
3.4.3 Material Properties	23
3.4.4 3D Printer	24
3.4.5 Post Printing Treatment	24
3.4.6 Assembly & Testing	25
<b>4. FF SYSTEM</b>	25
4.1 DESCRIPTION	25
4.2 MISSION REQUIREMENTS AND CONFIGURATION	25
4.2.1 Mission Requirements	25
4.2.2 Configuration	27
4.3 DESIGN	27
4.3.1 FR Properties	27
4.3.1.1 Mass	27
4.3.1.2 Rotor dimensions	27
4.3.1.3 Motor power	27

4.3.1.4 Thrust	27
4.3.2 Power	28
4.3.2.1 FF power	28
4.3.2.2 FR power	28
4.3.3 Weight Sizing	28
4.3.3.1 Battery weight	28
4.3.3.2 FR weight	29
4.3.3.3 Structural weight	29
4.3.4 Pmotor Distribution	30
4.3.5 Performance Constraints	30
4.3.6 Fuselage	30
4.3.7 Airfoil Analysis in Xfoil	30
4.3.7.1 Configuration	30
4.3.7.2 Xfoil analysis	31
4.3.8 Wing Analysis in AVL	34
4.3.8.1 Configuration	34
4.3.8.2 AVL analysis	35
4.3.9 Landing Gear Design and Weight & Balance Analysis	39
4.4 PRODUCTION	39
4.4.1 Material Properties	39
4.4.2 Wing Spar Analysis	39
<b>5. SOFTWARE</b>	40
5.1 DESCRIPTION	40
5.2 GENERAL OPERATION	40
5.2.1 Programming Software	40
5.2.2 Communication	40
5.3 MANUAL MODE	41
5.3.1 Controller	41
5.3.2 Pitch and Roll	41
5.3.3 Thrust and Yaw	42
5.3.4 Miscellaneous Controller Functions	42
5.4 AUTONOMOUS MODE	42
5.4.1 Visual Input	42
5.4.2 Standard Flight	43
5.4.3 Landing & Approach	43
<b>6. SYSTEM OPTIMIZATION</b>	43
6.1 DESCRIPTION	43
6.2 PROPULSION SYSTEM	43
6.2.1 Propeller	43
6.2.2 Motor	44

6.3 CONTROLLERS	44
6.3.1 ESC	44
6.3.2 Microcomputer	44
6.4 POWER	45
6.4.1 Power Distribution Board	45
6.4.2 Battery	45
6.4.2.1 Battery configuration #1	45
6.4.2.2 Battery configuration #2	46
6.5 COMMUNICATION	46
6.5.1 Short Range	46
6.5.2 Mid Range	46
6.5.3 Long Range	46
<b>7. ANALYSIS &amp; SUMMARY</b>	<b>47</b>
7.1 ANALYSIS	47
7.1.1 General Functionality	47
7.1.2 FR Auto Stabilization	47
7.1.3 User Command Input	47
7.1.4 Structural Design	47
7.1.5 Critical Damage Test	47
7.2 SUMMARY	48
7.3 FUTURE INTENT	48
<b>References</b>	<b>49</b>
<b>Appendix A - FR Rendering</b>	<b>52</b>
<b>Appendix B - FF Rendering</b>	<b>53</b>
<b>Appendix C - Calculating FANDECT Wing Geometry with MATLAB</b>	<b>55</b>
<b>Appendix D - FANDECT Wing Geometric Parameters for AVL</b>	<b>57</b>
<b>Appendix E - FR Script, Manual Mode</b>	<b>58</b>

# 1. INTRODUCTION

## 1.1 CONTEXT & BACKGROUND

### 1.1.1 Context

There exists an unmet demand for an aircraft that exhibits the range and endurance efficiency of a plane while operating with the vertical flexibility of a helicopter. Several companies have designed hybrid (VTOL) aircraft to meet such a demand. Although feasible, such hybrid aircraft currently lack the full potential of a fixed or rotary wing aircraft. Therefore, a hybrid may operate as both but with major performance degradation.<sup>1</sup> The FANDECT project redefines the method of conducting VTOL operations. This is done by designating specific aircraft subsystems to independently conduct certain mission tasks.

Although VTOL aircraft are engaged in a variety of operations, the FANDECT will be designed to perform light delivery tasks. The FANDECT will deliver a small payload (5-20 lb) within a 50 nmi radius. The FANDECT itself is a fixed wing aircraft and it will not be capable of landing at the delivery address. Therefore, the FANDECT will deploy one of several small electric motors that will deliver the payload vertically. The FANDECT will enter a traffic pattern above the delivery address and await the return of the engine to the assigned wing pylon.

### 1.1.2 Background

Since WWII, the US has expanded military doctrine to include the rapid deployment of forces by flexible aerial assets (i.e. helicopters). Helicopters provide the military with precision and flexibility in the placement of forces across the field of operation. Still, helicopters have a smaller operational range, are far less fuel efficient, and much slower than fixed wing aircraft. For these reasons, operations could only be conducted within range of an airbase or forward operating base. This made deep strikes (more common with fixed wing aircraft delivering munitions) less practical for the deployment and retrieval of military operators.

#### 1.1.2.1 Hybrid aircraft (VTOL)

The military attempted to overcome the shortcomings of helicopters by purchasing the VTOL V-22 Osprey in 2012.<sup>1</sup> Although still operational, the massive weight and rotor size of the V-22 prevent it from operating in confined and poorly supported areas. The surface area of the main wing also generates drag at a hover since the two main rotors are directing thrust downwards and directly against it.

VTOL technology is currently expanding in the civilian market. Aside from light quadcopter hobbyists, VTOL design has been pursued by the parcel delivery industry. Amazon is currently creating a drone delivery service called Amazon Prime Air. The service is projected to deliver packages to customers in 30 minutes or less. The aircraft is an autonomous VTOL electric drone guided by GPS and is capable of carrying a payload of up to 5 lbs.<sup>2</sup> Still, the design fails to develop an aircraft that has the energy efficient range associated with a fixed wing aircraft. This is sacrificed for the vertical landing feature.

#### 1.1.2.2 Re-evaluating VTOL usage

While companies are vying for a segment of the \$5.5 billion VTOL market (projected for 2020),<sup>3</sup> a different approach can be taken to meet the same operational requirement. Rather than sending an entire aircraft to deliver a payload, a subsystem can be sent to deliver the payload. The multi component system is referred to as the FANDECT.

In general, multi-engine aircraft require the greatest amount of engine power during takeoffs and landings. At cruise flight, the engines are not operating near maximum power. Therefore, it is possible for the aircraft to fly with less than 100% engines operational. The FANDECT takes advantage of cruise flight by deploying one of the engines (electric motors) as a payload delivery system. After delivery, the system returns to the aircraft prior to returning to an airfield for landing and where greater engine power is needed once more.

As seen in Figure 1.1 below, the FANDECT departs from an airfield. An RP is established as a fixed distance from the delivery location. Once the FANDECT reaches the RP, the rotary subsystem (F-R) detaches from the fixed wing (F-F). The F-F establishes a traffic pattern above the delivery location while the F-R descends, delivers the payload, and returns to the F-F. Once the F-F and F-R are reconnected, the FANDECT may continue to the next location or return to the airfield. This results in each leg of the flight using only the equipment that is optimal for that segment.

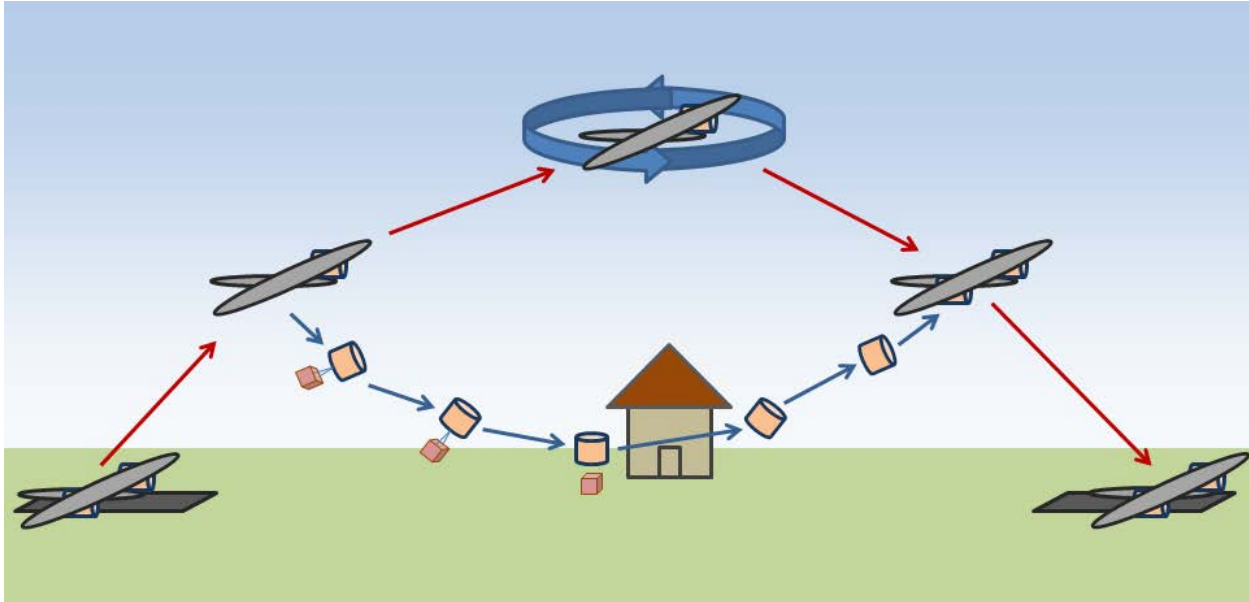


Figure 1.1 - Mission profile sketch of the FANDECT.

## 1.2 PROBLEM DEFINITION & APPROACH

The greatest problem with designing the FANDECT rests in designing multiple systems that interact with one another while maintaining subsystem autonomy. The FANDECT consists of one fixed wing main system (F-F) and four rotary wing subsystems (F-R). Each subsystem requires controls, processing, and power independency in order to transport a 3 kg payload.

### 1.2.1 F-F Design

The F-F design requires a configuration optimized for high endurance and low speed at low altitude.

The F-F wing design is visually similar to the NASA LEAPTech design. The LEAPTech is a NASA X-Project aircraft designed with multiple motors and small propellers positioned along the leading edge of a wing to improve aircraft performance while minimizing aircraft noise.<sup>4</sup> The F-F will initially be designed with a high aspect, cantilevered, dihedral, high wing to provide optimal endurance and ground clearance for F-Rs. Five pylons are located on each wing to mount the F-R subsystems that provide electric motor thrust.

If time permits, a second design iteration will include solar panel wings that will increase operational time and greater charging capacities for the F-Rs.

### 1.2.2 F-R Design

An F-R subsystem will consist of two coaxial contra-rotating propellers individually linked to two electric motors. The propellers are ducted primarily for safety purposes when delivering payloads to customers. The ducting also provides a shell that acts as a structure for subcomponent rigging. Subcomponents include a battery that provides power during autonomous flight mode, two ESC units, one microcomputer, one wifi adapter, landing struts, servos, control surfaces, and one power distribution board.

Each F-R will be capable of operating in two flight modes. The control surfaces and center of gravity must be calculated to provide optimal flight stability in both flight modes.

#### 1.2.2.1 Dependent flight mode

In the dependent mode, each F-R is mechanically attached to a pylon located on the F-F wing. Air intake is horizontal through the ducting. Power is drawn from the F-F battery bank and F-F processor instructions override F-R processor instructions.

#### 1.2.2.2 Autonomous flight mode

In the autonomous mode, the F-R decouples from the pylon and flies in a vertical profile due to center of gravity placement. Air intake is nearly vertical through the ducting. Power is drawn from the F-R battery. F-R processor instructions take precedence over F-F processor instructions. Variable RPM with the contra-rotating system provides

yaw control. Flat control surfaces positioned vertically and between the landing struts provide pitch and roll control. Each control surface is re-positioned with a servo that receives input from the F-R processing unit.

Careful consideration will be provided to the flight mechanics associated with the F-R and flight controls relationship. The F-R must be responsive to control input while avoiding erratic or over control that may result in the aircraft rolling over and losing its balance. This is a greater concern during moments of deployment and retrieval where F-R movement must be smooth and precise.

### 1.2.3 Aircraft Subsystem Network

Once the F-F and F-R are designed, the transition moments must be tested to determine the most ideal process. Since the FANDECT is flying low to the ground, changes in altitude most not occur. This is a problem when adding or removing engines to the aircraft that affect thrust and center of gravity. During these moments of transition, changes must be made to individual engine RPM to balance out thrust distribution. These calculated changes in RPM must then be scripted and loaded into the code that governs aircraft actions.

From a mechanical standpoint, the transition must also occur smoothly. The deployment and retrieval of F-R units by the F-F pylons are similar to landing a small aircraft on another aircraft in flight. During deployment, a mechanism is required to detach the F-R and allow the F-R to naturally rotate from the horizontal to vertical position due to its center of gravity. Precision sensors are required for positioning during retrieval. When in close proximity, a latch or magnetic type of mechanism is required to attach the F-R to the pylon. During both processes, sensors are required to also prevent unplanned collision between the F-R and F-F.

The F-R and F-F relay position and mission updates through wireless channels. An ideal communication medium must be chosen that minimizes data loss. Contingency plans must also be built into the programming of the subsystems in case communication is lost, sensors fail, or GPS fails.

## 1.3 SOCIAL INTENT

The FANDECT project emphasizes aircraft design and mechanical feasibility. But a functional aircraft design allows for the pursuit of a much larger ambition: improved transportation and city development.

Local transportation has always been gridlocked into a two dimensional field on the surface of the Earth. Although aircraft experience the luxury of travel through a three dimensional medium, such travel is restricted to routes connecting airports. Therefore, the use of air assets for local transportation remains rare. While cities continue to grow in density and traffic conditions worsen, the vast area above ground remains heavily unutilized. The FANDECT may offer a way to curb traffic and improve city growth through the implementation of three stages.

### 1.3.1 Stage 1: Corridor Designation

Currently, scores of airways cross the skies over the US in multiple directions. Known as victor airways, they are air corridors that were designated by the FAA and meant for pilot navigation under IFR operations. These corridors generally exist from 1,200 ft to 18,000 ft AGL.<sup>5</sup>

By using a concept similar to victor corridors, a new set of commercial air corridors may be defined over urban and suburban areas at approximately 500 ft to 1,000 ft AGL. These corridors will connect major logistic hubs to populated areas. With use of the FANDECT, packages may be air delivered from warehouses to customers regardless of landing area suitability.

### 1.3.2 Stage 2: Fleet Deployment

Once corridors and logistic points have been established, a fleet of FANDECTs may patrol designated routes at a flight spacing of several minutes. When an F-R deploys, it delivers the payload and then flies in the direction of the next F-F system enroute on the corridor. Once linked, the F-R recharges from the F-F battery bank. As the F-F nears a logistic point, the F-R deploys, lands at the logistic point, attaches a new payload, wirelessly updates the payload destination data, and waits to fly to the next F-F bound for the route designated for the package. It is comparable to installing a conveyor belt in the sky to deliver goods.

### 1.3.3 Stage 3: Autonomous Aerial Logistics Network

FANDECTs use designated air corridors to deconflict with local air traffic and minimize liability associated with autonomous aircraft flying outside of designated areas (uncontrolled and frequented by private and commercial aircraft). The autonomy of the system allows the fleet to operate day and night. Human operations are limited to ground control stations that monitor the entire system from one location. Such a network can deliver common goods within minutes to hours from the time of order placement.

The AALN also alleviates local ground traffic associated with common item purchases. When categorizing ground traffic, it may be categorized as either business, leisure, or goods procurement. The AALN stacks goods procurement traffic vertically.

Through implementation of the AALN, a 3D local transportation web is created and the added degree of movement results in pollution reduction, decrease in traffic, and improved city development.

## 2. RESEARCH & PLANNING

### 2.1 LITERATURE REVIEW

#### 2.1.1 Comparative Study of Similar Aircraft

The FANDECT is comprised of multiple electric motors attached to a high endurance fixed wing. Since the aircraft consists of two unique flight systems (rotary and fixed wing), VTOL and high endurance aircraft have served to develop initial design parameters. Both systems are not widely popular and some information is not available to the public. Several of the aircraft have also been designed by agencies with classified material. Therefore, it is difficult to gain specific data. But the data available will prove to be beneficial to the project.

Table 2.1 lists several aircraft that share those common features. The aircraft fall under three areas of interest. Category I involves aircraft with design and control features that are beneficial for the FR subsystem (small drone control and ducted fans).

Category II involves aircraft with a high number of small rotor electric engines that still maintain a high endurance profile. This data will be beneficial with designing the engine and pylon placement on the FF.

Category III involves high aspect ratio and endurance aircraft. This will dictate the aerodynamic design of the FF. Most of the third category aircraft have solar power charging capabilities. This is a secondary interest that can be implemented into the FANDECT if time permits.

Table 2.1 - Similar Aircraft

Manufacturer	Aircraft	Defining Feature	Quantifiable Data
DARPA Aurora Flight Sciences	VTOL X-Plane <sup>7</sup>	Single engine Multi fan ducts VTOL	Turboshaft: 3 MW Fan ducts: 24 L/D: 10 Cruise: 300-400 kt PL fraction: 0.40
DARPA Northrop Grumman	Tern <sup>8</sup>	Medium AR VTOL Contra-rotating	Motors: 2
NASA	X-57 Maxwell <sup>9</sup>	High AR Multi motor	AR: b = 31 ft Motors: 18 (13 kW)
Schleicher	ASH 31 <sup>10</sup>	High AR Solar power	AR: 33.5 L/D: 56 Wing loading: 53 kg/m <sup>2</sup> Empty mass: 425 kg MTOW: 630 kg Power: 1 Rotary engine (42 kW) 4 small solar panels
Consortium	Eta <sup>13</sup>	High AR	AR: 51.33 L/D: 70 Wing loading: 44.8 kg/m <sup>2</sup> Empty mass: 710 kg MTOW: 850 kg Power: 1 Piston engine (47 kW)
NASA AeroVironment	HP03 Helios Prototype <sup>14</sup>	High AR Multi motor Solar power	AR = 30.9 Motors: 10 (2 hp) Power: 18.5 kW

Manufacturer	Aircraft	Defining Feature	Quantifiable Data
		Endurance	Hours: 24
Solar Impulse	HB-SIA <sup>16</sup>	High AR Multi motor Solar power Endurance	AR = 19.7 Motors: 4 (10 hp) Power: 6 kW Hours: 36

Note: hp specification is per motor.

#### 2.1.1.1 DARPA VTOL X-Plane

The DARPA VTOL X-Plane (Figure 2.1) is a Category I aircraft and it is the only multi engine VTOL aircraft included in the study. It will serve as a benchmark for common vertical takeoff designs with multiple engines attached to a high AR wing.

The aircraft is designed with a unique multi ducted fan configuration that is powered by a single turboshaft engine. The ducted fans minimize wingtip vortices while providing a nominal vectored thrust capability. Although capable of taking off vertically, the result is an L/D ratio of 10. When compared to high endurance aircraft, the L/D ratio is nearly six times smaller. Still, the aircraft has a payload fraction of 40% on takeoff and can possibly achieve 300-400 kts. In comparison to the FANDECT, the ducted fan design and thrust vectoring provide a basis for FR construction. The PL fraction also shows the possibility of ducted fan systems transporting loads comparable to their own weight.<sup>2</sup>



Figure 2.1 - DARPA X-Plane artist rendering.<sup>6</sup>

Although not officially stated in any reports, several features of the DARPA X-Plane can be identified through published illustrations (see Figure 2.1). The fuselage is designed with a rectangular cross section that varies in height from the front to aft section.

The wing is a high mounted configuration designed with a constant chord length along the span of the ducted fans. The wings are mounted to a rotating device hidden within the fuselage that pivots the wing and ducted fans vertically for takeoff. The wing tips are crowned with winglets that exhibit a dihedral angle of approximately 40 degrees. The canard also has winglets that exhibit an anhedral angle of approximately 10 degrees. The canard to wing ducted fan ratio is 1:3. The fan ducts are designed with a square cross section. Elevators are attached to each exhaust to provide vector thrusting. The effectiveness of vector thrusting with the X-Plane configuration is unknown.<sup>7</sup>

#### 2.1.1.2 DARPA Tern

The DARPA Tern (Figure 2.2) is a Category I aircraft and it is the smallest aircraft on the list. Interest in the aircraft rests in the contra rotating system that traverses the aircraft horizontally in cruise flight as well as vertically

for takeoff and landing. There is also an interest in aircraft control with the contra rotating system and 6 control surfaces. Data collected on these areas will assist in the design of the FR system.

The aircraft primarily consists of a medium wingspan and contra rotating rotor system attached to the nose. Landing gear is located on each wing and vertical stabilizer. The landing gear does not retract but appears to lock in at a specific angle during flight. A hardpoint is located on each of the two wings between the landing gear and wing tip. The wing acts as a blended body with the propulsion system attached to the very horizontal and vertical center of it. The wing geometry appears to be a blend between trapezoidal along the trailing edge and swept along the leading edge. The wing tip to root taper ratio is approximately 0.2.<sup>8</sup>



Figure 2.2 - DARPA Tern artist rendering.<sup>8</sup>

Control surfaces are located on each wing and vertical stabilizer. There are a total of six control surfaces. A vertical stabilizer is attached to the top and bottom of the aft section. A rudder is located on each vertical stabilizer to provide yaw control.<sup>8</sup>

Two control surfaces are allocated per wing. Although the configuration looks similar to an aileron and flap configuration, the aircraft lands vertically and more than likely flares the contra rotating system like a helicopter instead of using flaps. Therefore, the control surfaces are more likely ailerons paired with elevators to provide pitch and roll control. If one of the control surfaces actually are flaps (instead of ailerons) that slow down the aircraft on approach, then roll control may be possible through asymmetric RPM of the contra rotating system. The asymmetric RPM may provide a difference in torque that will result in aircraft roll in the direction opposite of the high RPM engine. Or if the rotor blades have variable pitch, then the aircraft will roll in the direction opposite of the increased pitch rotor system.

Percentage difference in rotor RPM or pitch versus roll rate is a major area of interest for the FR design. The transition from a rotary to fixed wing flight profile is similar to the flight dynamics of the FR. Both of these factors make the Tern an attractive aircraft to study in preparation for FANDECT design.

### 2.1.1.3 NASA X-57 Maxwell

Of all the aircraft studied so far, the NASA X-57 Maxwell (Figure 2.3) matches the proposed FANDECT concept by far. It is the only Category II aircraft in this study. The aircraft has a high aspect ratio, electric motors that cover nearly the entire leading edge of the wing, short high lift blades with long chord lengths, and projected high endurance. While the DARPA Tern serves as a similar design concept for the FR, the Maxwell serves as a similar design concept for the FF.

The X-57 is a concept aircraft currently under development at the NASA Armstrong Flight Research Center. The aircraft is using a new propulsion configuration known as LEAPTech. The research team claims that power distributed across fourteen motors generates twice as much lift at low speed. Twelve motors placed across the leading edge

primarily assist with takeoffs and landings. A larger motor is located on each wing tip to assist with cruise flight. This is currently being verified by comparing CFD results versus an actual test of the configuration.



Figure 2.3 - NASA X-57 Maxwell artist rendering.<sup>9</sup>

The energy drain is also expected to be far more effective than general aviation engines. For example, the proposed aircraft that is expected to be built in 2019 will be outfitted with a 500 KW power system that is capable of ferrying nine passengers. As pointed out by NASA, that is equivalent to only 700 hp. This results in a propulsion system that is nearly five times as powerful as conventional engines.<sup>9</sup>

Unfortunately, the tests are still the CFD and ground phase and are yet to be verified in flight and OGE. Eventually, the LEAPTech wing will be attached to a Tecnam P2006T for flight test purposes.<sup>9</sup>

Along with the benefits of improved power and fuel usage, the small multi engine configuration is also expected to be quieter and provide a smoother ride.<sup>9</sup> Reduced noise pollution is ideal for the FANDECT since it is expected to operate at low altitudes over suburban areas. A smoother ride may reduce long term maintenance due to wear and tear associated with aircraft vibrations.

As seen in Figure 2.3, the X-57 wing has a nearly negligible wing tip to root taper ratio. The slight trapezoidal wing is mounted in a high wing configuration.<sup>9</sup> Electric motors mounted on the wing tips prevent winglets from being installed and strong vortices might be generated from the outer placed motors.

Although the propellers are nearly located at the leading edge, the motor is housed in a pylon underslung on the wing. If effectively redesigned, this could also serve as storage for small payloads.

#### 2.1.1.4 Schleicher ASH 31

The remaining studies are Category III aircraft (high aspect ratio and endurance). High endurance for the FF system is vital since the FANDECT takes advantage of transporting rotary wing components long distances at an effective fuel consumption rate. This results in a lighter battery load and faster transport of the payload.

The Schleicher ASH 31 (Figure 2.4) is a one seater glider aircraft that was designed by a small family operated business in Germany. It is powered with a single 42 kW rotary engine. It does not have any other functional characteristics but its sleek design makes it more aerodynamic than general aircraft. It has a lift to drag ratio of 56

which is nearly 6 times greater than the Cessna 172 (a common general aviation aircraft) which peaks at 10.9 around 90 mph in standard cruise flight.<sup>10 11</sup>



Figure 2.4 - Schleicher ASH 31 photo.<sup>10</sup>

Each wing consists of two components that can be unassembled for ground transport. The wing configuration is trapezoidal with a high taper effect from wing root to tip. The 90 degree dihedral wingtips minimize any traces of wing tip drag generated from the high aspect ratio wing. The wing is mounted in a high wing configuration perhaps to prevent wing damage on landing since ground clearance with the fuselage is nearly 1 foot. Due to the thin chord length, the ailerons extend along nearly one third the length of each wing to provide enough surface area to be effective in controlling the aircraft.<sup>10</sup>

A blowhole boundary layer system is built into the flaps and ailerons. The designer of the ASH 31 incorporates an airfoil that has a max thickness located further back than traditional airfoils. This results in laminar flow experienced across a longer section of the wing and less friction experienced from separation bubbles or turbulence. But this also results in a rapid narrowing of the airfoil towards the trailing edge. As a result, the flow separates and creates a high drag bubble. To overcome this, blowholes are built in the section slightly prior to boundary layer separation.<sup>7</sup> With the ASH 31, the boundary layer is tripped at approximately 95% of chord length from the leading edge.<sup>10</sup>

The blowing of air redirected from another section of the aircraft forces the air to transition into a turbulent boundary layer. Although turbulence still generates drag friction, the drag is much lower than that experienced by a separation bubble. Along with blowholes, the manufacturer also uses zig-zag and dimple tape.<sup>12</sup>

As seen in Figure 2.4, the fuselage mimics a teardrop-like shape. The canopy and solar panels located aft of the wing are streamlined into the design with minimal protrusion. The empennage consists of a single rudder located on a tall vertical stabilizer. The horizontal stabilizer is mounted in a high tail configuration.<sup>5</sup> Although this may result in a deep stall with general aviation aircraft climbing at an angle high enough to disturb the flow over the horizontal stabilizer, the ASH 31 glider should not experience steep angles of attack in flight that will trigger such a stall.

The landing gear consists of two retractable wheels positioned in tandem. The wheels are positioned slightly aft of the pilot and below the empennage. The forward wheel is placed near the pilot but well ahead of the aircraft center of gravity. This minimizes the possibility of scraping the nose during takeoffs.<sup>10</sup>

#### 2.1.1.5 Consortium Eta

Similar to the ASH 31, the Consortium Eta (Figure 2.5) is also a glider manufactured in Germany. The Eta is a two seater aircraft with a significant lift to drag ratio. The aspect ratio is nearly 1.5 times greater than the ASH 31.

This is perhaps the main contributing factor that results in an L/D ratio of 70. Greater than the ASH 31 L/D ratio of 56, the Eta has the greatest L/D ratio among the aircraft studied in this list by far.<sup>13</sup>

The aircraft is powered with a Sola 2625-02 twin cylinder inline two stroke piston engine that delivers 47 kW. Due to the longer wingspan and surface area, the Eta experiences a smaller maximum wing loading ( $44.8 \text{ kg/m}^2$ ) when compared to the ASH 31 ( $53 \text{ kg/m}^2$ ).<sup>10 13</sup>



Figure 2.5 - Consortium Eta photo.<sup>13</sup>

The Eta has an empty weight of 710 kg and a gross weight of 850 kg. This results in a maximum load of 140 kg (which includes the crew of two). Although the aircraft generates more lift, overall it is heavier and transports a smaller load than the AH 31 (205 kg).<sup>10 13</sup>

#### 2.1.1.6 NASA HP03

The NASA HP03 (in conjunction with AeroVironment) (Figure 2.6) was designed to be an uninhabited high altitude aircraft that would fly non-stop. Such a mission profile is required to conduct certain Earth and atmospheric scientific research. Ideally, NASA would like to fly the aircraft nonstop for up to six months while carrying a payload of 200 lb.<sup>14</sup> Such payload capacity and endurance characteristics make the HP03 an ideal candidate for the long term goals of the FANDECT project (long term flight, delivering multiple light payloads).

Unlike most of the other aircraft in the study, the HP03 lacks an empennage. It was designed as an all wing aircraft with minimal extrusions. The wingspan is incredibly long (247 ft) and surpasses most aircraft operating in the United States. The wing maintains a constant thickness and chord length along the entire length.<sup>9</sup>

The aircraft is constructed with a combination of carbon fiber, graphite, epoxy, Kevlar, styrofoam, and a plastic skin. The main wing spar is a tubelike structure composed of carbon fiber and reinforced with Nomex and Kevlar. Styrofoam lined with plastic film shapes the leading edge of the wing.<sup>14</sup>

The HP03 is propelled by 14 BLDC motors that are rated at 1.5 kW each. Fitted with advanced composite propellers that are 79 inches in diameter, the aircraft is capable of achieving high levels of efficiency at high altitudes. With such a propulsion configuration, the HP03 travels at a cruise speed of 19-27 mph. Takeoff and landing speeds are comparable to that of a bicycle.<sup>9</sup>



Figure 2.6 - NASA HP03.<sup>14</sup>

Aircraft control is achieved through two methods. 72 trailing edge mounted elevators provide pitch control. Asymmetric power loading of the motors provide yaw control.<sup>14</sup>

Aside from the extremely high endurance and lack of fuselage, the HP03 differs from most of the other aircraft studied by being outfitted with over 62,000 solar cells. Lithium batteries are stowed in the four underslung pylons (which also house the landing gear). Although lithium batteries are currently used, the HP03 requires batteries with a higher energy density storage capacity to achieve all night flight. The Helios Team has proposed a proton-exchange membrane fuel cell. The technology involves combining oxygen and hydrogen gas to produce heat and water as byproducts. This technology should provide the HP03 will full day and night capability. The greatest impediments to implementing the fuel cell are designing the equipment for flight purposes and being light enough to be more effective than lithium batteries.<sup>14</sup>

Since the HB03 operates in military restricted airspace, the aircraft has been outfitted with a flight termination system. This consists of a parachute that deploys on command and a homing beacon to track aircraft location. In the event of loss of communication or control, the onboard computer executes the flight termination system to isolate the downed aircraft to the local area.<sup>14</sup>

The team has been experimenting with controlling pitch through differential thrust. If achieved, the 72 elevators located along the trailing edge, servo motors, and associated electrical wiring may be removed (25-30 lb weight loss). In flight, the HP03 wing is shaped like a shallow crescent with the wing tips higher than the center of the aircraft. Therefore, increasing the RPM of the motors near the wingtips resulted in the aircraft pitching downwards. Increasing the RPM of the motors near the center of the aircraft resulted in the aircraft pitching upwards. Although proven in flight, the Helios team will decide whether the pitch is effective enough to warrant the removal of the elevators.<sup>14</sup>

#### 2.1.1.7 Solar Impulse HB-SIA

The Solar Impulse HB-SIA (Figure 2.7) is a world record setting solar powered aircraft. It was the first solar powered aircraft to fly across the United States.<sup>10</sup> It also gained the popular title of first round the world solar flight aircraft in 2015-2016. The aircraft required a high endurance, low power configuration to accomplish the feat. Therefore, it has the wingspan of a Boeing 747, weighs 1.5 tons, and has as much power as a motorcycle. The company claims that the Solar Impulse is the largest aircraft ever built with such low weight.<sup>16</sup> The unique configuration

emphasizes endurance flight and can be used to develop a high endurance logistics aircraft that rarely has the need to land. Therefore, the aircraft may fly dedicated logistics routes with minimal interference.



Figure 2.7 - Solar Impulse HB-SIA.<sup>15</sup>

The aircraft is powered with four brushless electric motors each generating 17.4 hp. The motors are underslung on the wing. Each motor is attached to a reduction gear to limit rotational speed to 525 rev/min for a 2 bladed, 4 m diameter.<sup>16</sup>

The upper body of the aircraft is lined with 17,248 solar cells that collect 340 kWh per day. Each solar cell is 135 microns thick and line the skin of the top of the wings, fuselage, and horizontal stabilizer. To prepare for night flight, excess solar power is stored in lithium polymer batteries. The batteries have an energy storage density of 260 Wh/kg. Each battery is insulated with high density foam and stored in the engine nacelles. The storage bays are controlled by systems that regulate charging thresholds and temperature. Altogether, the batteries weigh 633 kg (25% of total aircraft mass).<sup>16</sup>

Airspeeds are low when compared to other aircraft but reasonable when compared to ground transport. At sea level, the aircraft may fly from 20-49 kts. At maximum operational altitude (9,000 m), the aircraft may fly from 31.5-77 kts.<sup>16</sup>

The aircraft has a unique mission profile. During the day time, the aircraft climbs to 9,000 m to maximize solar absorption, minimize cloud interference, and take advantage of the readily available light from the Sun. At dusk, the aircraft begins a gliding (power off) descent which lasts for four hours. For this duration, the aircraft draws nearly no energy. At the end of the four hours, the motors are re-engaged and power consumption resumes. The aircraft flies at 1,500 m where air density is higher and more lift can be effectively generated.<sup>16</sup>

### 2.1.2 FR Technical Research

FR technical research consists of scaling drone technology into an independent system that may act as both a drone and a fixed wing propulsion system. Drone technology is readily accessible through hobby sites catering to remote controlled aircraft. Although there is a wide range of specifications and quality, parts selection is generally narrowed down according to the operational intent of the drone. A basic drone consists of a frame, rotor system, battery, power distributor, remote control, and flight controller.

A frame is required to mount the hardware and provide rotor blade separation. The FR will utilize a cylindrical skin that provides fan ducting, propeller protection, and component mounting.<sup>17</sup>

One motor, propeller, and ESC set is required for however many rotor systems are desired. The initial FR design concept will require two motors, two propellers, and two ESCs. The ESC provides the user with motor control as well as stepping down the voltage from the battery rating. The propeller translates the mechanical input from the motor to thrust that propels the drone.

The motor converts electrical input to mechanical output through a high speed rotating shaft. RC motors are rated by kV. kV is the rpm/voltage rating of a motor.<sup>13</sup> For example, a kV rating of 2,000 states that the motor will experience 2,000 rpm when 1 V is applied. RC Aircraft and racing drones use a high kV rating for better maneuverability. But the high kV rating results in a higher power draw. The amount of power required to rotate a propeller at high rpm will increase and drain the battery at a much faster rate.<sup>17</sup>

A battery provides the electricity necessary to power the rotor systems, receiver, and miscellaneous components onboard. Perhaps the most common type of energy storage associated with small scale drones is the LiPo battery. Lithium polymer has a higher energy density than traditional batteries and it is also capable of a high discharge rate. The high discharge rate is necessary for circumstances that require a high energy input (i.e. highly maneuverable drones).

A power distributor reroutes power from the battery to the multiple drone components.<sup>17</sup> A basic power distributor may be used for initial drone setup. The battery and each ESC are attached to the power distributor. The receiver draws power from the ESC input.

A remote control is used when the FR is undergoing flight testing. The remote control provides the operator with a flexible platform to send immediate tasks to the FR. A receiver is installed on the FR when a remote control is being used. The receiver is linked through signal wire to the ESCs and control surfaces on the FR.

Control surfaces will require servos to move. Plastic micro servos may serve for initial prototype designs. Larger servos with metal gears may be required for drones operating at higher speeds (i.e. 30 kts).

Under normal operation (outside of flight testing), a microcomputer may be installed on the FR to act as a flight controller. A Raspberry Pi Zero W is a 1x3 in microcomputer shaped like a thin card. It has a built in wireless capability and may draw power from the power distributor. The GPIOs may be connected to the ESCs and servos linked to the control surfaces. Through low voltage triggers, the user may control FR functions via the Raspberry Pi Zero W. Since the Zero W has wireless capability, the user may SSH into the computer and wirelessly take full control of the system over a local network. At this point, the user may directly relay orders to the FR or load a Python script for the FR to follow.

### 2.1.3 Hazardous Material Research

Aside from experiencing direct contact with the rotating propellers, the LiPo battery is the most hazardous project component. Understanding basic lithium battery technology provides the insight necessary to make safety conscious decisions with handling such material.

Lithium battery technology consists of negative (anode) and positive (cathode) electrode materials, a microporous separator, and an electrolyte.<sup>19</sup>

The anode is generally made of graphite in powder form combined with binder material. The cathode is generally made of an oxide such as lithium cobalt dioxide.

A microporous separator is an extremely thin film (10-40 $\mu$ m thick) comprised of polyethylene, polypropylene, or a combination of both. The film exists to separate the cathode and anode while acting as a porous wall to allow only Li<sup>+</sup> ions to travel during charge or discharge. The film softens at increased temperatures. This property acts as a safety feature in the event that a particle penetrates the film and contact between the cathode and anode is imminent. Due to the temperature increase, film locally softens and melts to close the torn film.<sup>19</sup>

The electrolyte consumes the area between the cathode and anode. Common electrolytes are ethylene carbonate and diethyl carbonate saturated with Li<sup>+</sup>. The temperature that the battery will operate at generally dictates the type of electrolyte used. Contact between the electrolyte and any trace amounts of lithiated carbon is thermodynamically unstable under standard voltage use at and room temperature. High temperatures further accelerate reaction between the electrolyte and lithiated carbon. The reaction results in a gaseous discharge that is flammable. Therefore, lithium batteries should be stored and operated in areas under 60°C. If the lithium cell experiences higher temperatures (75°C), the cell will undergo self heating. This effect will be further catalyzed under the adiabatic conditions of a well insulated cell. According to United Nations testing, the battery will undergo thermal runaway within 2 days if maintained under such conditions.<sup>19</sup>

Thermal runaway involves the rapid self heating that a cell undergoes from the exothermic reaction triggered by the oxidizer of the positive electrode and the reducer of the negative electrode. The reaction rapidly releases the stored

battery energy. This creates a dangerous situation since flammable and combustible material exist in LiPo batteries.<sup>19</sup> As a precaution, LiPo batteries should be isolated when stored and preferably have shielding when installed in a device. For example, the ESC may generate a high level of heat when operating a motor. Storing a LiPo battery in contact with an ESC in an unventilated compartment may result in the battery failing and combusting.

During battery usage, lithium ions depart the anode and are intercalated into the cathode material. During battery charging, lithium ions depart the cathode and are intercalated into the anode. The process of intercalation involves storing the ion into one of many voids in a crystallographic structure. This prevents the generation of lithium metal from Li<sup>+</sup> in storage. Since lithium is stored as an ion, metal fire suppression techniques are not effective with lithium battery fires.<sup>19</sup>

One battery cell consists of stacking alternating electrode layers along a strip that may be rolled into a cylindrical configuration (common AA lithium battery configuration). Batteries common with drone usage are enclosed in foil pouches that are heat sealed.<sup>19</sup>

LiPo batteries should not be over discharged or overcharged. Over-discharging a LiPo battery results in cell thermal runaway which leads to cell failure. Overcharging LiPo batteries results in rapid exothermic degradation of the electrodes.<sup>19</sup>

Caution must be used to enter the correct parameters into a lithium battery recharging station to prevent overcharging. Caution must also be used to prevent over discharging during battery operation. The battery rating must meet or exceed the demand of the load that it is powering. A low voltage alarm should also be installed on each LiPo battery to notify the user that the battery should be removed and recharged.

## 2.2 PROJECT OBJECTIVE

The FANDECT is a proof of concept project that may be expanded in the future to develop systems for commercial and industrial use. The initial design and minimum configuration of the FANDECT consists of four rotary systems attached to a small wing with an estimated 10 ft wingspan.

The project will primarily study the relation between fully independent networked flight systems with actions dictated by the most effective flight profile and mission demands. Operating an electric motor as both a component of fixed wing thrust and as a VTOL delivery system will be a large focus of the study. A study will also be conducted to determine the amount of control authority generated by the use of variable RPM on a multi-motor fixed wing aircraft. Lastly, the project will be reviewed from an economic standpoint. Using the Bay Area in California as a possible area of operation, the feasibility (technical and economical) of implementing a FANDECT small package delivery system will be determined.

The FANDECT will undergo a basic flight and functionality test. The aircraft will conduct one standard traffic pattern. The FANDECT will conduct a standard fixed wing departure from a local runway. In the first one-third of downwind, one FR will detach and land at the midpoint of downwind (pre-defined by a GPS point). Upon landing, the FR will disconnect from its payload. The FANDECT will continue the traffic pattern with three intact FRs and it will perform a low approach with no ground contact. The FANDECT will continue around the traffic pattern. As the FANDECT turns onto downwind, the FR will depart and attempt to re-attach in the final one-third of downwind. The FANDECT will conduct an approach to the runway to a full stop and the flight test will be concluded.

## 2.3 METHODOLOGY

### 2.3.1 Mission Specification

Prior to beginning the design and production of the FANDECT, the mission should be specified. Mission specification involves requirements and a profile. The mission requirements will both dictate the design parameters and optimize them for the most effective configuration. The mission profile will dictate how the aircraft is expected to carry out proposed tasks.

The design process will continue to be molded by market, technical, and operational analyses of the FANDECT operation.

#### 2.3.1.1 Mission requirements

Initial mission requirements have been designed for the first generation FANDECT that will undergo a flight test.. As stated in the same section, an emphasis is placed on flight dynamics between the multiple subsystems. Once the flight test is passed, mission requirements may be increased for larger scale operation. Initial mission requirements are listed in Table 2.2.

Table 2.2 - Mission Requirements for Initial Design

<b>Payload capacity</b>	12 kg*
<b>Crew members</b>	None
<b>Endurance</b>	1 hr
<b>Cruise Speed</b>	50 mph
<b>Cruise Altitude</b>	1,000 ft MSL

\*3 kg payload per FR

2.3.1.2 Mission profile

The FANDECT mission profile consists of a deploy and retrieve operation. One FR detaches during flight to deliver a payload. The FR will rendezvous with the FANDECT after payload delivery and return to the designated pylon (fig. 1.1).

2.3.1.3 Market analysis

A market analysis will review possible business ventures for the FANDECT along with the lucrative aspect of such market segments. The market for small package mail delivery will primarily be reviewed. Major competitors such as Amazon.com will also be reviewed along with the pros and cons of their projected air delivery programs.

2.3.1.4 Technical analysis

The technical feasibility of deploying a FANDECT operation will identify what is necessary to begin operations. This includes a review of local infrastructure, legislation, and the logistics involved in delivering a package to a specific location for a customer.

For example, data has been gathered on local airports in the Bay Area of California. The FANDECT is expected to take off and land at a local airport. Therefore, the aircraft must be sized to operate within local airport restrictions. Local airport runway dimensions are listed in Table 2.3.

Table 2.3 - Local Airport Data

<b>Airport Location</b>	<b>Runway Width (ft)</b>	<b>Runway Length (ft)</b>
Oakland <sup>21</sup>	100	5676
Palo Alto <sup>22</sup>	70	2443
San Carlos <sup>23</sup>	75	2600
San Francisco <sup>24</sup>	200	7650
San Jose <sup>25</sup>	150	11000

2.3.1.5 Operational analysis

Lastly, an economic analysis will be conducted to determine the feasibility of designing, building, and deploying a FANDECT operation capable of servicing the Bay Area in California.

2.3.2 Production Phases

Due to the complexity of the subsystems interacting with one another, FANDECT production will be divided into multiple production phases (PP). Each phase will consist of individual subcomponent design, construction, testing, and refinement. Once subcomponents undergo at least one iteration, they will be combined to begin the next production phase. The production phases are as follows:

- PP1: FR
- Design
- Construction
- Flight Test
- Parameters Refinement

- PP2: FF

Design  
Construction  
Parameters refinement

PP3: FR+FF  
Design  
Flight Test

PP4: Networking  
Deployment Mechanism  
Retrieval Mechanism  
Flight Test

PP5: Payload  
Rigging  
Detachment

### 2.3.3 Concept Phases

The FANDECT project is scaled to improve operational effectiveness over several concept phases (CP). The concept phases are divided between subcomponent FR and FANDECT progression.

#### 2.3.3.1 FR progression

CP-R1: FR I  
Demonstrates full operation/control independency  
No detaching capability

CP-R2: FR II  
Detaching/reattaching capability

CP-R3: FR III  
FRs are networked with one another  
4 FRs deploy to deliver (separate times)

CP-R4: FR IV  
FR deploys to retrieve new payload

#### 2.3.3.2 FANDECT progression

CP-F1: FANDECT I  
Short FF wingspan  
4x FR I (2 per wing)  
Endurance: 1 hr

CP-F2: FANDECT IIA  
FF pylons modified for detachment operations  
FR II upgrade

CP-F3: FANDECT IIB  
FR III upgrade

CP-F4: FANDECT IIC  
FF pylons modified for inflight payload retrieval  
FR IV upgrade

CP-F5: FANDECT III  
Medium FF wingspan  
10x FR IV (5 per wing)

Endurance: 5 hr

CP-F6: FANDECT IV

Long FF wingspan

20x FR IV (10 per wing)

Endurance: 7 hr

CP-F7: FANDECT V

Solar panels integrated with high AR wings

Inflight FR recharging

Endurance: sunrise - sunset

CP-F8: FANDECT VI

Improve power usage and storage

Endurance: land only for maintenance

### 3. FR SUBSYSTEM

#### 3.1 DESCRIPTION

FANDECT thrust and payload delivery are controlled by multiple FR subsystems. The following sections describe the design, construction, and testing of the first and second generation FR subsystems: the FR I and FR II. The FR I will demonstrate full operation and control independency in a VTOL flight profile. The FR II will demonstrate the capability of detaching from the FANDECT pylon and entering a VTOL flight profile. The FR II will also demonstrate autonomous guided flight towards the FANDECT pylon, re-attach, and continue flight in a fixed wing profile.

#### 3.2 MISSION REQUIREMENTS & CONFIGURATION

Traditionally, aircraft design begins with defining mission requirements and capabilities. That process is followed by numerous calculations that govern the weight, geometry, and performance of the desired aircraft.<sup>26</sup> With the FANDECT, the FF design is governed by the physical and performance characteristics of the FR subsystem. The FR subsystem design is primarily governed by the weight and size of the payload to be delivered as well as operating in a VTOL capacity. Therefore, the FANDECT design process begins with the design and testing of the FR detailed in the following sections, continues with the design of the FF detailed in the next section, and is refined with the networked capabilities of the two systems.

##### 3.2.1 Mission Requirements

The FR is the component that provides the most unique capabilities to the FANDECT system. The FR must be capable of carrying a 3 kg payload that does not exceed 15 x 15 x 15 cm in volume. The payload mass and volume are dictated by small packages commonly purchased through online merchandise sites. Also, the FANDECT is being designed and constructed as a proof of concept. Therefore, the allowable payload is small and primarily serves as a physical component for the FANDECT to move from one location to another.

Being an uninhabited system, the FR requires a wireless data signal and onboard computer processing to communicate with the remaining FANDECT system.

The FR must be capable of accessing areas that lack the space for any sort of run on landings or takeoffs. The FR must also be capable of performing a controlled descent to such confined areas from 300 m MSL to 0 m MSL while hoisting a 3 kg payload.

The most unique mission requirement is that the FR must also operate as a fixed wing propulsion system when it is not detached and delivering packages. Therefore, the FR must be capable of operating in a horizontal configuration that can attach and detach to a wing. The FR control system must be capable of being overridden when attached to the fixed wing system but also activate an autonomous flight profile when detached from the wing.

##### 3.2.2 Configuration

Since the FR must be capable of accessing confined areas, a rotary wing configuration is most suitable. A traditional quadcopter configuration is avoided since four rotor discs placed side by side increases the landing area required and becomes cumbersome in a horizontal configuration when attached to a fixed wing. The thin profile makes it unstable when the direction of thrust is mounted directly into the oncoming freestream. The use of one rotor disc is also avoided since one motor will generate a counter torque on the FR structure.

Therefore, the FR is designed with a contra-rotating motor configuration. Two motors are mounted at the core of a cylindrical structure. The two motors rotate in opposite direction of one another but at the same rate of rotation to negate any counter torque felt by the structure. When ascending and descending, the thrust line for both motors are aligned along the same axis. This improves the stability and thrust delivered at the center of the FR and avoids any asymmetric torque applied on the structure at different points.

The contra-rotating rotor discs are horizontally blockaded by a cylindrical shell. The shell is not being implemented to design a ducted fan. Rather, the cylindrical shell serves as the monocoque structure of the aircraft. The power, CPU, and control systems are housed in the shell. The shell protects the components from any foreign debris (especially at higher flight speeds experienced in the fixed wing configuration). It also protects the electronics from shorting out under adverse weather conditions (i.e. rain and sprinklers). The shell also provides a third level of functionality. Since the FANDECT is ideally used to deliver small payloads to densely populated areas, it is necessary to protect any passersby on the ground from the fast rotating dual blade system. The shell protects individuals from being injured in the event of drone contact.

The FR does not have a built in payload bay. This minimizes the size, mass, and drag that would accompany a payload bay. Prior to the FANDECT taking off, the payload is stored in the FF pylon that the FR attaches to. The payload is also attached by cable to the aft section of the FR. Once the FR detaches from the pylon in-flight, the payload is released from the pylon and the attached cables allow it to be underslung in a hoist configuration. When the FR approaches the delivery zone, the cables detach from the payload. The FR is rigged once again after the FANDECT lands. Ideally, the FR would depart the FANDECT in the vicinity of a logistics facility and be rigged with another payload. That process would minimize the frequency of the FANDECT landing. This is the primary reason to develop the FF as a high endurance wing that requires minimal down time.

### 3.3 DESIGN & FUNCTIONALITY

The FR functions through compact hardware controlled by pre-programmed code. The hardware is similar to equipment commonly found in hobby enthusiast level quadcopters. The programming code is generated with Python 2 and executed on a Linux based microcomputer.

#### 3.3.1 Components

##### 3.3.1.1 Structure

The FR structure is a cylindrical monocoque shell constructed from 1.75 mm ABS filament extruded at 230°C and cooled at room temperature. In contrast to common quadcopter designs, the shell houses the equipment internally. The added protection from environmental conditions enhances the life cycle of the onboard electronics and also minimizes inflight outages due to contact with airborne debris or water.

The shell is directly connected to the motor support beams as well as the landing struts. Areas of contact between the shell, beams, and struts are cushioned with an elastic filament. The elastic material dampens the high frequency vibrations from the two contra rotating motors as well as the periodic shock from the landing struts.

The inner diameter of the shell is 258 mm. The diameter provides clearance for a 254 mm propeller diameter with 2 mm of clearance beyond the blade tip.

The shell is divided into an upper and lower section. The upper section houses the FR components and encircles the blade rotating area. The lower section is comprised of the landing struts, flaps, and housing for both the flaps and rods used to control the flaps.

Due to the contra-rotating configuration of the two electric motors, the height of the upper shell is limited to a minimum of 161 mm. The height of the lower shell (70 mm) is a function of the size of the flaps and height of the landing struts.

##### 3.3.1.2 Propeller

The propeller diameter is restricted to a diameter of approximately 254 mm (10 inches). An increase in propeller diameter results in an increase of the outer shell that houses the FR components. As a result, the larger shell will increase drag per FR unit attached to the FANDECT.

If the thrust generated by the FR subsystems cannot sustain flight when coupled with the FF system, then the number of FR units will be increased. Therefore, the number of FR units will be adjusted in lieu of increasing the diameter of the propeller.

The propeller airfoil type, blade number, and twist analysis will be reviewed in a later chapter.

##### 3.3.1.3 Power

Two LiPo batteries are connected to the power distribution board that powers the servos, computer, and motors.

Each LiPo battery has been rated with the specifications listed in Table 3.1.

Table 3.1 - LiPo battery specifications<sup>27</sup>

<b>Capacity</b>	2,200 mAh
<b>Cell count</b>	3S
<b>Cell voltage (nominal)</b>	3.7 V
<b>Battery voltage</b>	11.1 V
<b>Discharge rating (constant)</b>	25C
<b>Discharge rating (burst)</b>	35C
<b>Current (continuous)</b>	55 A
<b>Current (burst)</b>	77 A

The capacity measures the amount of power that the battery is capable of storing. In this case, constant usage of the battery at 2,200 mA (2.2 A) will discharge the battery in 1 hr.<sup>28</sup>

One LiPo cell is designed with a nominal voltage of 3.7 V. The maximum voltage that a LiPo battery may be charged to is 4.2 V. The minimum safe discharge voltage is 3.0 V. 3.7 V is the approximated average of the high and low voltage. The cells may be placed in series to deliver a greater voltage. In this case, the battery consists of 3 cells. The “S” designates that the cells are placed in series. A “P” rating indicates that the cells are placed in parallel.<sup>28</sup> The 3 cells deliver a rating of 11.1 V across the battery.

$$\begin{aligned}
 \text{Cell count} &= 3S \\
 \text{Cell voltage (nominal)} &= 3.7V \\
 \text{Voltage} &= \text{cell count} * \text{cell voltage} = 11.1 V \\
 \text{Voltage} &= 11.1 V
 \end{aligned} \tag{3.1}$$

When working with BLDC motors, the voltage rating influences the rotor RPM. BLDC motors have a kv rating which is the amount of RPM per volt applied. 11.1 V provides an RPM that is 11.1 multiplied by the kV rating of the motor.<sup>19</sup>

The discharge rating (constant) is used to calculate the maximum allowable discharge in amps at a constant rate without damaging the battery. When the discharge rate is multiplied with the capacity of the battery, the result is the maximum allowable continuous current. The “C” designation with the discharge rate indicates that it is not a stand-alone number and requires the capacity to calculate the allowable current.<sup>28</sup>

$$\begin{aligned}
 \text{Discharge rate (constant)} &= 25C \\
 I_{\text{continuous}} &= \text{discharge rate (constant)} * \text{capacity} \\
 I_{\text{continuous}} &= 55 A
 \end{aligned} \tag{3.2}$$

The discharge rating (burst) may be used in a form similar to the constant rating. The burst rating indicates the maximum allowable current for a 10 second period.<sup>20</sup> The rating may generally be used for quick accelerating flight profiles.

$$\begin{aligned}
 \text{Discharge rating (burst)} &= 35C \\
 I_{\text{burst}} &= \text{discharge rate (burst)} * \text{capacity} \\
 I_{\text{burst}} &= 77 A
 \end{aligned} \tag{3.3}$$

#### 3.3.1.4 Motor

BLDC motors provide optimal RPM and torque for small drones. The RPM is high and can generate thrust when necessary. The torque can sustain rotation at the given RPM with common blade designs for small drones. The FR was tested with motors ranging from 900 to 1500 kV.

$$\begin{aligned}
 \text{RPM} &= \text{kv rating} * \text{voltage rating} \\
 \text{RPM}_{900 \text{ kV}} &= (900 \text{ kV}) (11.1 \text{ V}) = 9,990 \text{ RPM} \\
 \text{RPM}_{1500 \text{ kV}} &= (1,500 \text{ kV}) (11.1 \text{ V}) = 16,650 \text{ RPM}
 \end{aligned} \tag{3.4}$$

A high RPM motor is ideal for maneuverability and rapid response to control input but it lacks torque. A low RPM motor may not provide a drone with high maneuverability but it exhibits higher torque. For a transport drone, higher torque is desired since the RPM can be maintained at a consistent rate under heavy loads or moments of flight profile transition (i.e. detaching from the FF pylon). Also, rapid maneuvering is not a primary requirement for FANDECT payload transport.

### 3.3.1.5 Data & signals processing

FR control is governed by a microcomputer located onboard the FR that processes three sets of data signals. The microcomputer provides motor speed and flap control with PWM data that maneuvers the FR to the desired location and perform the assigned task. The visual data provides the microcomputer with visual cues during landing and docking guidance.

The Raspberry Pi Zero W is the governing microcomputer of the FR. The Zero W is a Raspberry Pi Foundation product that was released in February 2017 with the listed specifications in Table 3.2. It is light in mass, compact, uses low power, and has GPIO pins that are suitable for receiving external data signals. Each GPIO pin is capable of generating a 3.3V signal.<sup>28</sup>

Table 3.2 - Raspberry Pi Zero W Specifications<sup>29</sup>

<b>CPU</b>	1 GHz
<b>Memory</b>	512 MB RAM
<b>Hard Disk Drive</b>	8 GB micro SD card
<b>Power</b>	Micro USB
<b>Wireless Connectivity</b>	802.11 b/g/n wireless LAN Bluetooth 4.1/Bluetooth Low Energy (BLE)
<b>Ports</b>	1x Mini HDMI 2x Micro USB
<b>GPIO</b>	40 pin
<b>Dimensions (LxWxH)</b>	65 x 30 x 6 mm

PWM is a method that transfers digital data in a way that mimics analog data. The Raspberry Pi GPIO pins may activate an electronic device by turning it on (3.3V) or turning it off (0V). The digital signal may also be sent as a square wave by rapidly sending an on/off signal. Doing so allows the GPIO pin to send a signal that mimics a voltage greater than 0V but less than 3.3V. The rate at which this occurs is a function of frequency and duty cycle assigned by the user programming the code. The inverse of the given frequency determines the period of one on/off cycle. The duty cycle determines the percentage of the on/off cycle where the signal will remain on.<sup>30</sup> Table 3.3 illustrates several examples of the duty cycle effect on the voltage being applied across one period.

Table 3.3 - Duty cycle effect on voltage over time

<b>Duty Cycle [%]</b>	<b>One Period</b>	
0	0V	
50	3.3V	0V
75	3.3V	0V
100	3.3V	

The speed of each of the two motors is governed by an ESC. The ESC draws current from the power distribution board and receives data from the microcomputer via PWM. The data received consists of a frequency and duty cycle. The ESC translates the two parameters into a voltage pulse that is delivered across the motor. A specific frequency and duty cycle is related to a specific motor RPM.

The movement of each of the four flaps is governed by a 180° micro servo. As with the ESC, the servo also

operates via PWM. The servo receives a frequency and duty cycle. A specific frequency and duty cycle is related to a specific angular location on the servo. Therefore, one end of the range of values results in the servo aligning at 0°. The other end of the range results in the servo aligning at 180°. A value from the mid range results in the servo aligning at 90°.

The PixyCam delivers visual information of high contrast colors in the form of a 320x200 matrix.<sup>31</sup> See Section 3.3.4.2, Stage 2 for an explanation of the data usage.

#### 3.3.1.6 Control Flaps

The FR control system consists of data output by the onboard processor, four micro servos, and four control flaps. The microcomputer delivers a signal to the servo that dictates which angle the servo will reposition to.

The servo is mechanically linked to a control flap located inside and aft of the FR subsystem. A small displacement of the servo will result in a small displacement of the flap outwards to obstruct a segment of the flow departing the contra-rotating propellers.

#### 3.3.1.7 Software

The Zero W microcomputer runs the Raspbian Jessie with PIXEL OS. The OS runs on a Debian based operating system that functions as a Unix OS. Debian is based on the Linux kernel and it features one of the largest online repositories for software packages. This improves the compatibility of the OS by providing free software that is readily available to download.<sup>32</sup> Without such a directory, it would be left to the user to develop such software or find a way to port it from another OS.

Raspbian Jessie tailors the Debian OS to the low performance Raspberry Pi CPU and electronics infrastructure. The Raspberry Pi is developed with ARM processors. Such chips are common in compact devices such as smartphones and tablets. ARM chips provide devices with small and inexpensive processing power that consumes low power and emits low heat. The tradeoff is that ARM chips are designed with fewer transistors when compared to x86 processors common with computers currently on the market.<sup>33</sup>

PIXEL provides the Raspbian Jessie OS with a clean and modern desktop environment. The desktop improves accessibility to software applications as well as easing user navigation between programs.<sup>34</sup>

The script generated for the FANDECT system was developed in a Python 2 format. The motors and servos are controlled through either pre-programmed Python script when in autonomous mode or through user inputs that are refined by the Python script in manual mode. The user input is refined to deliver smooth control behavior to the subsystems of the FANDECT.<sup>35</sup>

### 3.3.2 CG

The axisymmetric design of the FR is beneficial in adjusting the CG. As a component that is cylindrically shaped with the thrust line collocated with the axis of symmetry (central axis of the shell), the CG is located on the axis. The structural components are symmetrical in mass. Paired components are anchored in the shell 180° across from one another to provide a counterbalance. The heaviest components housed within the shell are the two LiPo batteries (173 g each). Therefore, the LiPo batteries serve as adjustable ballasts that may be adjusted to balance the CG if it is located off axis from the thrust line.

The vertical location of the CG exists near the height of the bottom motor. The upper shell section contains more mass than the lower section.

It is advantageous to have the CG located lower than the average vertical location of the two motors that are generating thrust. When the FR detaches from the FF to deliver a payload, the orientation of the FR transitions from horizontal to vertical. The aft located CG results in the aft section of the FR pivoting 90° downwards and the thrust being redirected from forward to upward. The FR then conducts a power on gliding approach to the delivery site in order to save battery power during the maximum gross weight leg of the FR mission profile.

### 3.3.3 Control

FR control operates differently when the largest velocity component exists along the vertical axis (up or down) versus any horizontal axis.

As stated in the motor section, the contra-rotating motors maintain constant RPM in opposite directions of rotation to prevent the FR structure from experiencing adverse yaw due to a counter torque. The onboard IMU (inertial measurement unit) relays the angular velocity along the vertical axis to the processing unit every ten microseconds. The processor outputs a yaw command in the opposing direction to zeroize the angular velocity. Once the aircraft achieves a negligible yaw rate that is defined within a tolerable range, the ratio of voltage delivered across the upper motor versus the lower motor is recorded and used to derive a constant. The constant serves as a multiplier against the

rpm of the stronger motor. When the user requests a change in thrust, the stronger motor will be multiplied with the constant in order to mitigate adverse yaw as a result of imbalanced motors.

The intentional relaying of different speed signals to the ESCs will also result in asymmetric motor RPM. The minor difference in RPM will translate the counter torque to the structure of the FR and generate a yaw about the vertical axis in the direction of the user's command. When the processing unit identifies a signal being transmitted on the user input yaw channel, the user request will temporarily override the zeroizing of the angular velocity along the vertical axis.

The four FR flaps are mounted aft of the CG and center of lift. When deployed into the high velocity stream departing the propellers, the flap creates a pitching moment by increasing form drag on one side of the FR. The flap may be deployed and contracted rapidly at a large angle to generate a quick pitch or roll correction. It may also be deployed at a small angle and maintain position to achieve a newly desired flight profile.

### 3.3.3.1 Vertical axis control

The FR abides by vertical axis control parameters generally during approach and takeoff from a delivery zone. As previously noted, this occurs when thrust is more parallel to the vertical axis than the horizontal axis. Visually, the FR is postured in an upward position. Table 3.4 identifies the primary systems that govern each mode of control.

Table 3.4 - Vertical axis control systems

<b>Pitch</b>	Forward & aft flap deployment
<b>Roll</b>	Left & right flap deployment
<b>Yaw</b>	Asymmetric RPM of contra-rotating motors

### 3.3.3.2 Vertical off axis control

The FR abides by vertical off axis control parameters generally after the rotation following detachment and during approach to the FF pylon. This occurs when thrust is more parallel to a horizontal axis than the vertical axis. Visually, the FR is postured in a sideways position. In the off axis profile, roll and yaw control is switched from the on axis profile (see Table 3.5).

Table 3.5 - Vertical off axis control systems

<b>Pitch</b>	Forward & aft flap deployment
<b>Roll</b>	Asymmetric RPM of contra-rotating motors
<b>Yaw</b>	Left & right flap deployment

## 3.3.4 Docking Guidance & Payload Drop Off

The most critical moment of FANDECT operation involves the docking procedure of the FR when it returns to the FF. Due to the criticality, the procedure consists of a three stage docking procedure.

### 3.3.4.1 Stage 1: Beacon homing

The docking procedure is initiated with beacon homing when the FR is at a distance greater than 6 m from the FF. The beacon signal emitted from the fuselage of the FF allows the FR to crudely home towards it. The technology is similar to aircraft navigating off of an NDB. While unable to track towards the signal like a VOR, the NDB still allows the pilot to travel in the relative direction of the signal.

Distance determination greater than 6 m may be approximated with GPS location of the FF and FR.

### 3.3.4.2 Stage 2: Visual homing

Once the FR is within 6 m of the FF, visual homing overrides beacon homing. A color sensing camera is located onboard the FR. PixyCam is a kickstarter project that uses a micro-USB connection to relay color information detected by an onboard camera with a resolution of 320x200 pixels.<sup>31</sup>

Using the PixyCam software, the user gives the device a specific color to identify. The camera records color data according to a 320x200 (x,y) coordinate matrix that mirrors the pixel resolution of the camera. If the user designated color is identified in the pixel, the area becomes highlighted.<sup>31</sup>

If a large amount of similar pixels are located next to one another, then the area is grouped into a rectangular shape. The size of the shape is output to the computer terminal in the form of the left and rightmost x locations along

with the down and up most y locations of the rectangle. Therefore, FR controls may be manipulated to center a color on the camera (pixel location 160x100). This will result in the FR homing to the color panel so long as the PixyCam verifies that the panel is increasing in size.

The user may define a second color to track at the same time. When two large areas of nearby colors are defined by the user, the PixyCam may also relay rotational information according to the orientation of one color to another. As a side note, the PixyCam can be programmed to track up to eight unique color signatures.<sup>31</sup>

This process has been implemented with the Stage 2 FF docking procedure by coloring high contrast panels on the underside of the FF wing and adjacent to each pylon. With the pylon between two different colored panels, the FR will home towards the two colors while maintaining zero degrees in rotation (aligned longitudinally with the FF).

Distance determination less than 6 m may be calculated by comparing the size of the high contrast panels located on the FF measured by the PixyCam. During the construction phase, the size of the panels registered by the PixyCam at 6 m is recorded. When the panel size is detected by the PixyCam during the docking process, the distance is assumed to be 6 m. The change in size can be continuously compared to the benchmarked size at 6 m to determine distance. The increase in size translates to approaching the pylon while the decrease in size translates to departing the pylon.

#### 3.3.4.3 Stage 3: EM docking

EM docking occurs rapidly and when the FR is within 8 cm of the FF pylon. Along one side of the FR exists an electromagnet strip. An electromagnet with an opposite charge is located along the length of the bottom of the pylon.

Once the FR is visually guided within proximity of the FF pylon and distance is verified by the PixyCam, current temporarily activates the electromagnets long enough for the FR to contact the FF pylon.

Distance determination is necessary to verify that the FR has docked with the FF pylon. A docking switch protruding from the bottom of the FF will be pushed once the FR is docked. This will relay the message that the FR is now docked with the FF pylon at a distance of 0 cm.

#### 3.3.4.4 Post docking

Once the docking switch relays a signal, a front and aft mechanical link deploy from the pylon and hook into two slits on the FR. The forward dual link engages the FR with one cable delivering FF power and second cable delivering FF signal data. Once the links have engaged the FR, the electromagnets are discharged. The FR recharges the LiPo battery with the FF battery bank. The FR microcomputer processes signals delivered by the FF. The FR controls are returned to the default (minimum drag) position. The FR operates at an RPM level that mirrors the other three FRs docked with the FF.

#### 3.3.4.5 Payload drop off

The second most critical moment of FANDECT operations involves guiding the FR to the delivery zone and dropping off the payload. For first generation FANDECT delivery, the delivery zone will be marked with a high contrast panel.

The onboard PixyCam used in docking procedure Stage 2 is mounted on a 90 degree servo housed within the shell of the FR. When the FR is descending towards the delivery zone, the servo pivots the pixycam 90 degrees until it is facing downwards (towards the ground). While the FR is guided to the delivery location by a pre-established GPS location, the PixyCam will override guidance control once the color signature is registered. Therefore, the PixyCam will overcome the lack of accuracy provided by civilian GPS. The FR will hover within inches of the intended delivery zone and deactivate the cable hooks, thus, delivering the payload. The FR engages the three stage guidance procedure to return to the FF.

### 3.4 PRODUCTION

The FR subsystem is a design that is uncommon with drones. Many of the subcomponents were designed with geometry that cannot be purchased at local stores. Therefore, the FR was made with the use of additive manufacturing. 3D printing the FR components removed the manufacturing limitations generally placed on constructing a system with locally purchased parts.

Production of the FR involves six steps. These steps govern the 3D parametric design, machine code generation, material selection, parts production, post treatment, and assembly.

#### 3.4.1 Computer Aided Design

The FR was designed as a CAD assembly consisting of numerous parts that are individually 3D printed. Autodesk Inventor 2017 (Student Version) was used to CAD every FANDECT component.

As a first generation design, the FR was partitioned into multiple subsections for several reasons. Being a

prototype aircraft, the FR will more than likely experience multiple initial failures and crashes. If the FR sustains damage, only the damaged subsections require replacement with new 3D printed components. This saves on the amount of filament used to 3D print as well as the downtime experienced during the 3D printing process.

For example, the outer shell consists of eight subsections, each requiring five hours to 3D print. If the shell was printed as one solid component, it could very well take more than 24 hours to 3D print.

#### 3.4.2 Machine Code Generation

Once the FR parts are designed in a CAD program, the file is saved as a stereolithography file (.stl). The stl file translates the parametrized part into an outer shell that depicts it as one solid component. 3D printing preprocessing software is used to prepare the stl file for production. Simplify3D was used to prepare the stl file exported from Autodesk Inventor.

Simplify3D imports the part in stl format into a computer generated depiction of the 3D printer being used. The part is turned around and aligned on the printer bed in the position most suitable for the part geometry.

Speed, temperature, resolution, and infill parameters may be adjusted according to the type of geometry being printed. Due to the presence of many curved aerodynamic surfaces, printing speeds were reduced by 50-60% to prevent any misalignment along the curves. Extruding filament at higher speeds along a curve generally results in delamination between the layers. This occurs due to the lack of time given for the freshly applied layer to melt with the previously printed layer.

The temperature of the printing head (extruder) and printer bed are adjusted according to the material being used. Material type and temperature are further reviewed in the 3D Printing section.

For the FR, most components were printed with a resolution of 0.2 mm height per layer. Although the 3D printer being used may print at a height of 0.1 mm (double the resolution), this nearly doubles the printing time. The Post Printing Treatment section describes how the parts are smoothly refined without requiring a high resolution and time consuming print.

The infill parameter governs the internal density of the object. While the shell of the part is printed at 100% density, the internal structure may consist of a honeycomb-like structure. Low density structure both reduces the amount of filament used as well as the weight of the structure. Therefore, structures that do not require the toughness of a completely solid infill may be printed with a lighter internal structure. From an aerodynamic perspective, the weight reduction results in a lighter aircraft. A lighter aircraft requires less engine power to propel it (or maintain the same engines and experience a greater allowable thrust envelope). FR components used a 20% infill. Due to the thin profile of most of the geometry, the components are still tough enough to maintain original form without any bending noticeable to the human eye.

Once the parameters have been entered, the program generates a machine code for the printing process. The code consists of support geometry, printing axis movement speeds, filament extrusion, and (x,y,z) coordinates for the printing head to follow.

Support material is printed in areas where an overhang may exist on the component. For example, printing a hole in a vertical sheet will require the printer to begin printing over no support at the upper half of the hole. Support material may be added as a pillar that begins at the bottom of the circle so that it may serve as support at the top of the circle. It is generally offset by a few millimeters so that it may be easily broken away in the post printing treatment of the part. Support material is generated according to a software algorithm and user input parameters. For the FR, any geometry that results in a layer overhang exceeding 45° will require support.

The coordinates are generated by using software algorithms that define the most optimal path for the printing head to travel along that will generate the imported part layer by layer. Once the part geometry is converted to machine code, the file is uploaded to a microSD card and transported to the 3D printer.

#### 3.4.3 Material Properties

Deciding the type of material to build a part with requires a background in how 3D printers work as well as an analysis of common materials used.

3D printers vary in a wide range of capabilities and cost. The 3D printer used for the FANDECT project uses FDM. This involves feeding plastic in the form of a thin filament through a heated extruder head that melts the plastic as it is printed onto a bed. The extruder moves along the x, y, and z axis while applying the filament in a small cylindrical form.

Two common filaments used with FDM are PLA and ABS. Both materials have a list of benefits and drawbacks. PLA is a biodegradable plastic created with sugar cane and cornstarch, making it more environmentally friendly. It does not require venting during the printing process since it does not release toxic fumes. PLA does not actively react with acetone (a process common with smoothing the rough outer surface of a printed part). PLA is printed at

approximately 210°C. The printer bed does not need to be heated for PLA to adhere to it. PLA is more suitable for individuals new to 3D printing. It is more forgiving of less than optimal printing conditions and it is less sensitive to environmental temperature changes.<sup>36</sup>

ABS is an oil based plastic that is less environmentally friendly than PLA. When melted during the 3D printing process, ABS releases toxic fumes that are known to be carcinogenic. When printing with ABS, the area must be vented and uninhabited. ABS is printed at 230°C. The printer bed is heated to 85°C in order to allow ABS to adhere to it. ABS is more suitable for advanced 3D printer users. It requires a 3D printer with a well calibrated and leveled printer bed, a temperature controlled printing bay, venting, and constant monitoring. ABS is prone to delaminate and warp due if a constant temperature is not maintained. The high sensitivity to environmental temperature makes ABS difficult to print with.<sup>36</sup>

The material properties of PLA and ABS differ by a considerable amount. PLA strength exceeds ABS. It is sturdier and less prone to bending under stress. Rather, the part will shatter instead of bend.<sup>37</sup> As a result, ABS toughness exceeds PLA. When undergoing a stress test, a part printed in ABS will begin to bend whereas the same part printed in PLA will break or shatter. Despite the greater difficulty in printing, ABS is preferred over PLA for most engineering applications.<sup>36</sup>

#### 3.4.4 3D Printer

The 3D printer used for the FANDECT project is the MakerGear M2. The M2 is an FDM printer upgraded with a dual extruder head capable of printing a part with two different materials. The extruder takes in 1.75 mm filament and extrudes at a 0.4 mm diameter. The M2 is capable of printing a volume of 200 x 250 x 200 mm.<sup>38</sup> The volume is nearly four times greater than entry 3D printers. Therefore, the FR does not have to be spliced to an unreasonably small size in the CAD process so that it can fit in the printing bay. When smaller parts are used, the structure becomes less stable and heavier since more hardware is required to attach the parts.

The M2 has an open bay which is problematic for ABS printing. The M2 is shielded with a 2x2x2 foot acrylic cube. The acrylic paneling retains the heat emitted from the extruder and printing bed and provides a consistent ambient temperature to surround the part during the printing process. The ABS parts have less delamination, warpage, and better geometric tolerance as a result.

#### 3.4.5 Post Printing Treatment

Once the ABS part has been printed, it is allowed to cool so that it may be separated from the printing bed. Carefully, the support material is removed with tweezers, pliers, and a razor blade. This generally results in a rough and scratched area. The overall part will also have a rough texture due to the layering process involved with the printing.

Since the FANDECT project involves the optimization of rotary and fixed wing systems, minimizing drag is necessary in every aspect possible. The rough 3D printing finish contributes to a high skin friction drag if left unattended. Therefore, printed parts undergo two steps to minimize skin friction.

All finished parts undergo a sanding process with fine grain sandpaper. The layers are sanded to minimize the half cylindrical tube-like surface. The parts undergo a final sanding step in the direction of expected freestream flow to minimize any burrs or bumps that may promote separation of laminar flow.

Although sanding may remove most of the rough protrusions visible to the human eye, an acetone wash reacts at the microscopic level to generate a smooth finish and refined look. ABS is soluble with acetone. In fact, an ABS part submerged in acetone will begin to exhibit a melting appearance within several minutes. Brushing a part with acetone results in a melting of the outer layers. In this form, the part may be brushed to a smooth finish with the 3D printing edges becoming nearly non-existent.

The acetone wash also relieves another issue with 3D printing ABS parts. Since ABS is sensitive to temperature changes during the printing process, internal stress is generated once the part finally cools.<sup>14</sup> A bending stress is highly visible with curved parts. If a part cracks along the length of the applied layers, the part has an affinity to return to a straight profile. A curved ABS component experiences compression on the convex face and tension on the concave face with the neutral axis located internally. Acetone washing the part eases the greatest tension and compression stresses that are located on the surfaces. The acetone dissolves the ABS plastic enough to reshape in the current position.

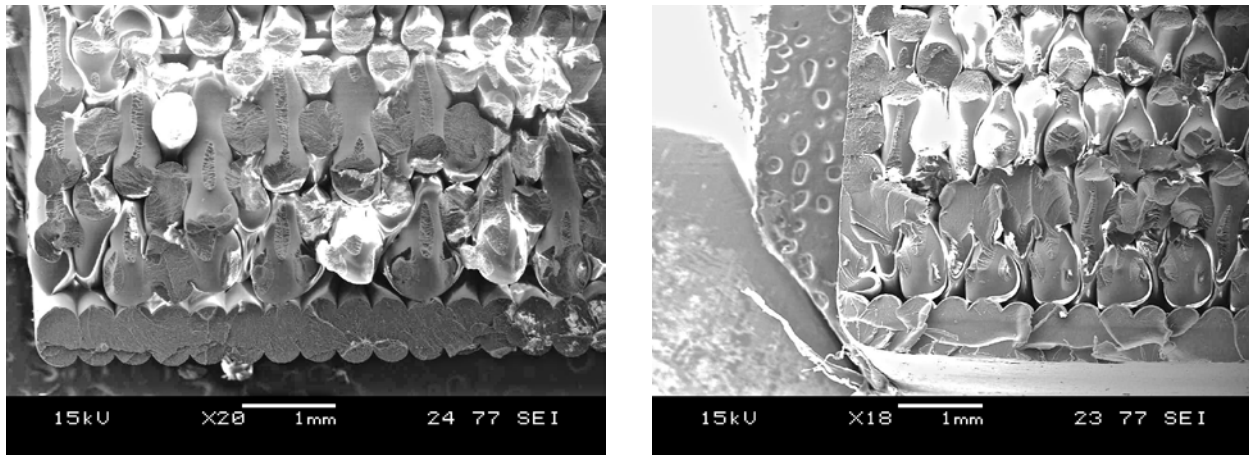


Figure 3.6 - SEM imaging: comparison of 3D printed ABS parts, standard (left) and acetone washed (right).<sup>39</sup>

As seen in the SEM images of a dog bone toy (Fig. 3.6), the standard 3D printed part maintains a rigid shape along the surface. The acetone washed part experiences more tensile strain but less tensile stress due to the melting and reshaping of the layers.<sup>39</sup>

Acetone washed components are allowed 3 hours to dry in a well ventilated area prior to assembly.

#### 3.4.6 Assembly & Testing

Treated parts are assembled with stainless steel hex bolts and screws. Dimensions that lack enough tolerance to connect with one another are sanded and acetone washed once more. Updated dimensions are entered into the CAD file to improve the next printed part.

Due to manufacturing tolerances, the two motors will not be manufactured to generate the exact RPM. The propellers will also exhibit varying mass and one set may generate more lift than another. These two differences will result in a counter-torque felt by the FR structure since one rotor system will be more effective than the other at the same given speed parameter. To overcome this, the FR undergoes a weight and balance after assembly. With two given sets of motors and propellers, the FR will be brought to a 6 inch hover while anchored by wire to four static ground ports.

A corrective factor will be determined from multiple hover tests to determine how much more effective one rotor is versus the other. The corrective factor will be multiplied with the output speed data of the more effective motor. The speed factor is not applied to the less effective motor because this will cause the motor to operate at a speed greater than the more effective motor. This may result in an over torque of the motor at high RPM.

## 4. FF SYSTEM

### 4.1 DESCRIPTION

FANDECT lift and primary systems housing are governed by the FF system. As stated in the FR design section, FF design is governed by FR parameters. FR thrust and payload capabilities are the primary properties that cross over to the FF design process. Combined, the two systems create a fully operational FANDECT. The following sections will cover the design, construction, and testing of the first two generations of the FANDECT: the FANDECT I & FANDECT IIA-C.

### 4.2 MISSION REQUIREMENTS AND CONFIGURATION

While the FR provides the FANDECT with a set of unique capabilities, the FF serves to improve the FR capabilities and nothing more. Alone, the FR subsystem is a VTOL drone with a high energy consumption rate that lacks the operational range of a fixed wing drone. Therefore, the FF serves to improve the operational range of the FR while decreasing the energy consumption rate.

#### 4.2.1 Mission Requirements

Constricted by the thrust and mass of four wing mounted FR subsystems, the FF must provide an aerodynamic platform that the FR can attach to. The platform must be able to expand the FR operational range by generating more lift, less drag, and consuming less energy in the process. Unlike the FR, the FF is designed to land like a traditional fixed wing aircraft. Therefore, the FF must have traditional landing gear capable of enduring standard aircraft landings

to a paved runway.

The FF must be capable of housing the primary battery system that powers the FR subsystems. The same electrical grid must also recharge the FRs upon reattachment after payload delivery.

The FF must house long range communication equipment for the FANDECT. Since the FR receives instructions from the FF, the FR is not required to house long range communications equipment. The FR may also operate in confined areas near the ground. The FF is pictured in the sky above and serves as an excellent relay of information from the user to the FR.

The pylons must be designed with a profile that exhibits minimal drag. Since the FANDECT I does not exhibit FR launching capabilities, the aerodynamic design is the sole requirement for the pylons.

But the most technical component of the FF system is introduced with the FANDECT II series and the improved pylon design. The FANDECT IIA introduces FR launching capabilities. Each pylon must house the mechanical links and EM strips that detach and retrieve the FR. The pylon must also be capable of storing a payload that is loaded prior to FANDECT takeoff. Prior to FR detachment, the pylon must be capable of freely releasing the payload. The FR Mission Requirements section dictates the maximum payload dimensions (15 x 15 x 15 cm). The pylon must be capable of completely housing the payload volume.

The FANDECT IIB introduces FR retrieval capabilities. Fitting with the guidance procedures of the FR, the FF must have high contrast color rectangular panels located on the belly of the wing. Panels must be located on both the left and right of each pylon.

Finally, the FANDECT IIIC introduces the concept of retrieving a payload in mid-flight. In other words, the FR may be launched to retrieve a payload from a logistics facility and return to the FF where the payload is loaded into the aerodynamic pylon. This reduces the form drag that may be generated by an externally mounted payload while enroute to a delivery location.

The speed of the FANDECT should be only fast enough to avoid stall during basic maneuvers. Preferably, a low speed is desirable so that the FR will not require a high max velocity to rendezvous with the FF. Approximately 5 m/s of overlap should exist between the maximum FR velocity and the minimum FF velocity. For example, if the FR is designed with a maximum velocity of 22 m/s, then the FF should be capable of achieving a minimum velocity of 22 m/s without stalling. Figure 4.1 illustrates the moment of re-attachment in the FANDECT mission profile.

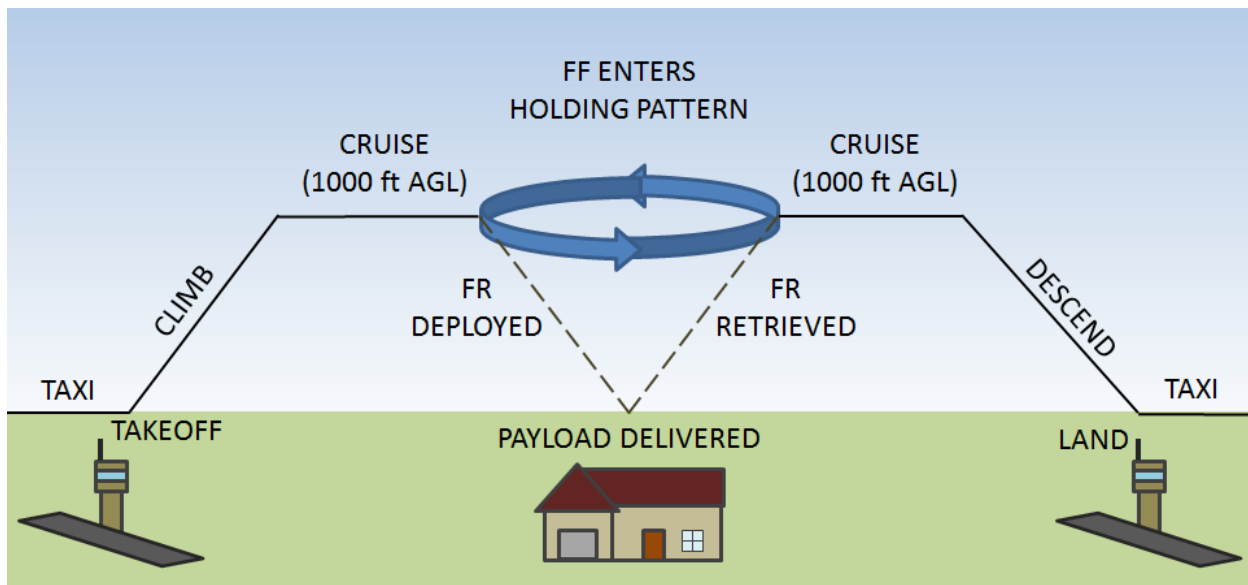


Figure 4.1 - FANDECT mission profile.

FANDECT landing requirements are constricted to local Bay Area airports since the aircraft is designed to operate in the local area. The five local airports involved in the analysis include those located in Oakland, Palo Alto, San Carlos, San Francisco, and San Jose. Palo Alto Airport has the shortest runway (744 m) as well as the smallest runway width (21 m). FANDECT geometry and takeoff parameters will operate safely within these restrictions.

To operate effectively, the FANDECT should be able to achieve a horizontal velocity of 22 m/s at 304 m MSL with a 2.54 m/s climb rate at 90% of maximum power. A horizontal velocity of 22 m/s is slow enough for an FR unit to reattach yet fast enough for the FF to generate enough lift to maintain flight with a reasonably sized wing. A climb

rate of 2.54 m/s allows the FANDECT to traverse 1,000 ft in two minutes. The remaining 10% of maximum power shall be maintained as a contingency buffer. These conditions shall be met with only three of four FR subsystems present. This condition defines the moment of greatest power demand on the FANDECT.

The FANDECT should be outfitted with enough battery capacity to fulfill the stated requirements for one hour.

#### 4.2.2 Configuration

Since the FR utilizes the FF as a type of long distance aerial conveyor belt, the cruise flight profile is optimized for endurance. The FF incorporates high endurance aircraft characteristics to reduce energy consumption during the cruise segment of flight.

The wing is designed with a high endurance airfoil. See the following section for airfoil comparison and analysis.

Major design influences rest with the wing design, fuselage size, and pylon geometry. The wing provides the aerodynamic benefit that the FR subsystems cannot experience alone. The fuselage maintains a sleek profile that minimizes drag while being large enough to house battery and communication equipment. The pylons are also designed to minimize drag while small enough to house the FR payload and detach/reattach equipment.

### 4.3 DESIGN

Similar to the FR, the FF functions through hardware controlled by pre-programmed code. The hardware is similar to equipment commonly found in small scale fixed wing drones. The programming code is generated with Python 2 and executed with a microcomputer operating a Linux based OS.

#### 4.3.1 FR Properties

The FF is designed according to the FR characteristics derived from the FR design section.

##### 4.3.1.1 Mass

$$m_{OE,FR} = 2 \text{ kg (measured)}$$

$$m_{PL} = 3 \text{ kg (mission requirement)}$$

$$m_{TO,FR} = m_{FR,OE} + m_{PL} = 5 \text{ kg} \tag{4.1}$$

$$\text{payload fraction} = \frac{m_{PL}}{m_{TO,FR}} = 0.6 \tag{4.2}$$

##### 4.3.1.2 Rotor dimensions

$$d_{prop} = 0.254 \text{ m}$$

$$r_{prop} = 0.127 \text{ m}$$

$$\eta_{prop} = 0.8$$

##### 4.3.1.3 Motor power

$$V_{battery} = 11.1 \text{ V}$$

$$I_{ESC} = 55 \text{ A}$$

$$\eta_{motor} = 0.8$$

$$P_{motor} = V_{battery} I_{ESC} \eta_{motor} = 488 \text{ W} \tag{4.3}$$

##### 4.3.1.4 Thrust

$$n_{motor} = 2$$

$$T_{FR} = n_{motor} [2\pi r_{prop}^2 \rho_{air} (\eta_{prop} P_{motor})^2]^{1/3} \tag{4.4}$$

At 0 m MSL:

$$\rho_{air,0m \text{ MSL}} = 1.225 \text{ kg/m}^3$$

$$T_{0m,FR} = 53.32 \text{ N}$$

At 304 m MSL:

$$\rho_{air,305m \text{ MSL}} = 1.190 \text{ kg/m}^3$$

$$T_{304m,FR} = 52.82 \text{ N}$$

#### 4.3.2 Power

##### 4.3.2.1 FF power

FF power is dictated by the equipment necessary to maintain the FANDECT at cruise flight for 1 hour with power provided by three FR subsystems under the following cruise conditions.

$$\begin{aligned}v_{CR,FF} &= 22 \text{ m/s} \\E &= 1 \text{ hr} \\h &= 305 \text{ m MSL} \\ \rho_{air,305m \text{ MSL}} &= 1.190 \text{ kg/m}^3\end{aligned}$$

To achieve the required climb rate, the horizontal velocity component (cruise) must maintain 22 m/s while the vertical velocity component (climb) achieves 1 m/s. The total velocity is derived by combining the horizontal and vertical velocity components.

$$\begin{aligned}v_{FF,CL} &= 2.53 \text{ m/s} \\v_{\infty} &= \sqrt{v_{CR,FF}^2 + v_{CL,FF}^2} = 22.15 \text{ m/s}\end{aligned}\tag{4.5}$$

Maximum power available is calculated as a function of the newly determined velocity and thrust per FR unit at 305 m MSL.

$$\begin{aligned}n_{max,FR} &= 4 \\P_{max,FF} &= n_{max,FR} T_{304m,FR} v_{\infty} = 4,680 \text{ W}\end{aligned}\tag{4.6}$$

A 10% contingency power reserve is deducted from the maximum power available.

$$\begin{aligned}\eta_{res,FF} &= 0.9 \\P_{a,FF} &= \eta_{res,FF} P_{max,FF} = 4,212 \text{ W}\end{aligned}\tag{4.7}$$

##### 4.3.2.2 FR power

The maximum power required at the most demanding moment of cruise flight is distributed across the minimum number of FR subsystems that may be present.

$$\begin{aligned}\eta_{min,FR} &= 3 \\P_{a,FR \text{ min}} &= P_{a,FF} / \eta_{min,FR} = 1,404 \text{ W}\end{aligned}\tag{4.8}$$

#### 4.3.3 Weight Sizing

The FF structure is designed to be lightweight and withstand stress endured at the location of the pylons due to detachment and reattachment of the FRs.

FANDECT weight varies according to the number of FR subsystems and payload attached to the pylons. Therefore, maximum weight is experienced with all four FRs attached with maximum payload weight attached to each. But lift is calculated for a FANDECT configuration of three FRs instead of four. In this configuration, only 75% of total power is available. The loss of 25% power is greater than the negligible decrease in weight of one FR. FANDECT weight is defined by the following equation.

FANDECT weight consists of several fixed and adjustable weight components.

$$W_{TO,FANDECT} = W_{TO,FF} + W_{TO,FR} n_{min,FR}\tag{4.9}$$

$$W_{TO,FF} = W_{E,FF} + W_{B,FF}\tag{4.10}$$

##### 4.3.3.1 Battery weight

Although  $P_{A,FF}$  is the power available to the FANDECT, the  $P_{motor}$  rating is used to calculate energy consumption. The power draw is translated to battery weight with the use of a specific energy constant. The specific energy used in the following calculations applies to lithium polymer. The following is also calculated for a FANDECT operating with all available motors at 100% for 1 hr.

$$P_{motor} n_{max,FR} n_{motor} = 2,930 W \quad (4.11)$$

$$E_{FANDECT} = 1 \text{ hr} + 20 \text{ min VFR reserve} = 80 \text{ min} \quad (4.12)$$

$$E_B^* = \text{specific energy} = 200 W \cdot \text{hr}/\text{kg}$$

$$\eta_B = \text{current draw rate efficiency} = 0.9$$

$$W_{B,FF} = \frac{P_{motor} n_{max,FR} n_{motor} E_{FANDECT}}{\eta_B E_B^*} g = 284 N \quad (4.13)$$

To achieve a better approximation of battery weight, the mission profile has been divided into segments according to varying motor power demand. A power % of 100% indicates that the motors are operating at 100% capacity. The battery weight indicates the amount in Newtons that is required to provide the power draw for the given time segment with a LiPo battery.

Table 4.1 identifies the segments in chronological order from taxi to shut down. A 20 minute VFR reserve has been added to the FANDECT endurance rating of 60 min for a total of 80 min. The 20 minute reserve is calculated with 4 operational FRs operating at cruise conditions.

Table 4.1 - Energy weight per flight profile segment

Action	Time (min)	Power %	# FR	W <sub>B</sub> (N)
Taxi	5	30	4	5.3
Take off	1	90	4	3.2
Climb	2	90	4	6.4
Cruise	17	67.5	4	40.7
Loiter	10	90	3	23.9
Cruise	17	67.5	4	40.7
Descend	2	30	4	2.1
Land	1	90	4	3.2
Taxi	5	30	4	5.3
Reserve	20	67.5	4	47.9
Total	80	N/A	N/A	179

$$W_{B,FF} = 179 N$$

#### 4.3.3.2 FR Weight

FR takeoff weight consists of 4 FR subsystems with a 3 kg payload attached to each FR.

$$W_{TO,FR} = m_{TO,FR} g = 49 N \quad (4.14)$$

$$W_{TO,FR \times 4} = W_{TO,FR} n_{max,FR} = 196 N \quad (4.15)$$

#### 4.3.3.3 Structural weight

For design purposes, FANDECT weight was estimated with the FR subsystems accounting for 30% of total weight. A 0.3 propulsion weight fraction of total weight has been used for a lightweight electric powered drone. A lower estimation is used for an electrical system. Although battery weight may be substantial, the FF battery weight was not added to the FR propulsion weight estimate. The lower propulsion fraction allows for greater battery weight to be added to the FF system.

$$f_{W,P} = 0.3$$

$$W_{TO,FR} n_{max,FR} = f_{W,P} W_{TO,FANDECT} \quad (4.16)$$

$$W_{TO,FANDECT} = 653 N$$

The structural weight of the FF is estimated by deducting subcomponent weight from the takeoff weight of the

FANDECT.

$$\begin{aligned} W_{E,FF} &= W_{TO,FANDECT} - W_{TO,FR \times 4} - W_{B,FF} \\ W_{E,FF} &= 173 \text{ N} \end{aligned} \quad (4.17)$$

$W_{E,FF}$  consists of the following components:

- Fuselage: 3 landing gear, frame
- Electronics: computer, long/short range communication
- Power: PDB, battery banks, inflight recharge points
- Wing: spar, ribs, stringers, skin, flaperon
- Empennage: hor. stab., elevator, ver. stab., rudder
- Wiring: power (16 AWG), signal (20 AWG)

#### 4.3.4 $P_{motor}$ Distribution

Since the FANDECT is capable of detaching one FR for payload delivery, the aircraft must be able to maintain level flight with three FRs. The loss of one FR requires the remaining three FRs to share the lost output of that unit. If the minimum number of FRs operate at 90% motor power to maintain steady flight, then the motor power percentage at cruise flight with four FRs may be calculated. Note that the 90% motor power is a result of the 10% contingency power reserve deduction.

$$\begin{aligned} f_{P,FR \min} &= 0.9 \\ P_{motor,FR \min} &= P_{motor} f_{P,FR \min} = 439 \text{ W} \end{aligned} \quad (4.18)$$

$$f_{P,FR \max} = f_{P,FR \min} (n_{min,FR}/n_{max,FR}) = 0.675 \quad (4.19)$$

$$P_{motor,FR \max} = P_{motor,FR \min} f_{p,FR \max} = 329 \text{ W} \quad (4.20)$$

Ideally, the FANDECT should be able to maintain level flight with all four FRs operating at 67.5% of maximum output. This percentage may be used to calculate power draw during standard cruise flight. These parameters are also used to send signals to the ESC for motor control. For example, if 100% of motors are attached, then the motors will operate at 67.5% to maintain steady flight. If 75% of motors are attached, then the motors will operate at 90% to maintain steady flight.

#### 4.3.5 Performance Constraints

The FANDECT operates locally and takes off from the same location that it lands at. Therefore, the operational range is calculated as the distance traversed in the first leg of cruise flight. Referring to the mission profile breakdown in Table 4.1, the first cruise leg lasts for 17 minutes. The operational range of the aircraft is calculated with the following equation.

$$\begin{aligned} E_{cr} &= 17 \text{ min} \\ v_{cr} &= 22 \text{ m/s} \\ R_{op} &= E_{cr} v_{cr} = 22.4 \text{ km} \end{aligned} \quad (4.21)$$

#### 4.3.6 Fuselage

Due to the uninhabited and autonomous control system of the FANDECT, the fuselage does not require life support equipment for crew members. The fuselage is designed to be large enough to house the battery bank, computer, and serve as a centralized location for processing and re-routing of power and signal wires.

The fuselage is designed as a slender, cylindrical, monocoque body. The wing is mounted towards the forward and top section of the fuselage.

#### 4.3.7 Airfoil Analysis in Xfoil

##### 4.3.7.1 Configuration

The FANDECT main wing is designed with an airfoil that prioritizes lift generation at cruise flight. Less important is lift generation at high angles of attack and aerobatic-like maneuverability. A high camber may improve the lift coefficient at cruise flight. A high L/D ratio is also necessary to minimize the amount of drag generated that the electric motors must overcome.

The mission profile of the FANDECT is repetitive and pre-determined. Functioning across a wide range of angles

of attack is not necessary. Therefore, a small leading edge radius may be used to decrease drag at the expense of operating within a narrow range of angles of attack.

Signal and power lines run the length of the FANDECT wing. Ideally, a thick wing would improve the structural strength and provide the space necessary to store electronics, navigating equipment, and wiring. It also provides the operator with space to access and repair the equipment when necessary. But an optimal L/D ratio takes precedence over this condition.

Through the information obtained with the literature review, the NACA 4412 is a common airfoil used with high endurance aircraft and it is fitting with the desired geometry for the FANDECT.

#### 4.3.7.2 Xfoil analysis

The NACA 4412 airfoil was analyzed with the use of Xfoil software.<sup>41</sup> The NACA 4412 airfoil was selected due to high L/D ratios that result in less battery drain due to drag.

The NACA 4412 was modeled with 250 panels exhibiting a cosine distribution (Fig. 4.2). To determine the effect of airfoil thickness, the NACA 4415 was also analyzed alongside the NACA 4412. The increased thickness of the NACA 4415 is beneficial for structural integrity but it may result in boundary layer complications. The thickness may lead to boundary layer detachment at higher angles of attack. Therefore, the NACA 4412 was analyzed side by side to determine how beneficial the thicker airfoil may be.

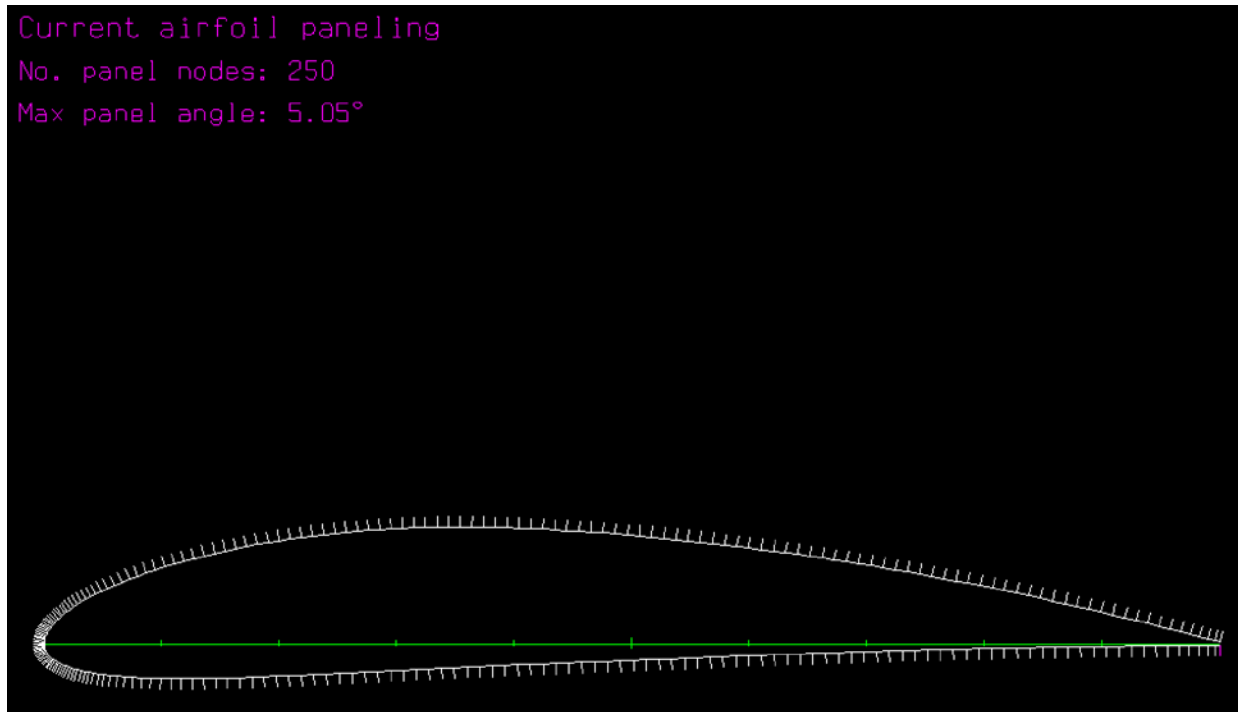


Figure 4.2 - Airfoil geometry and panel distribution for the NACA 4412.

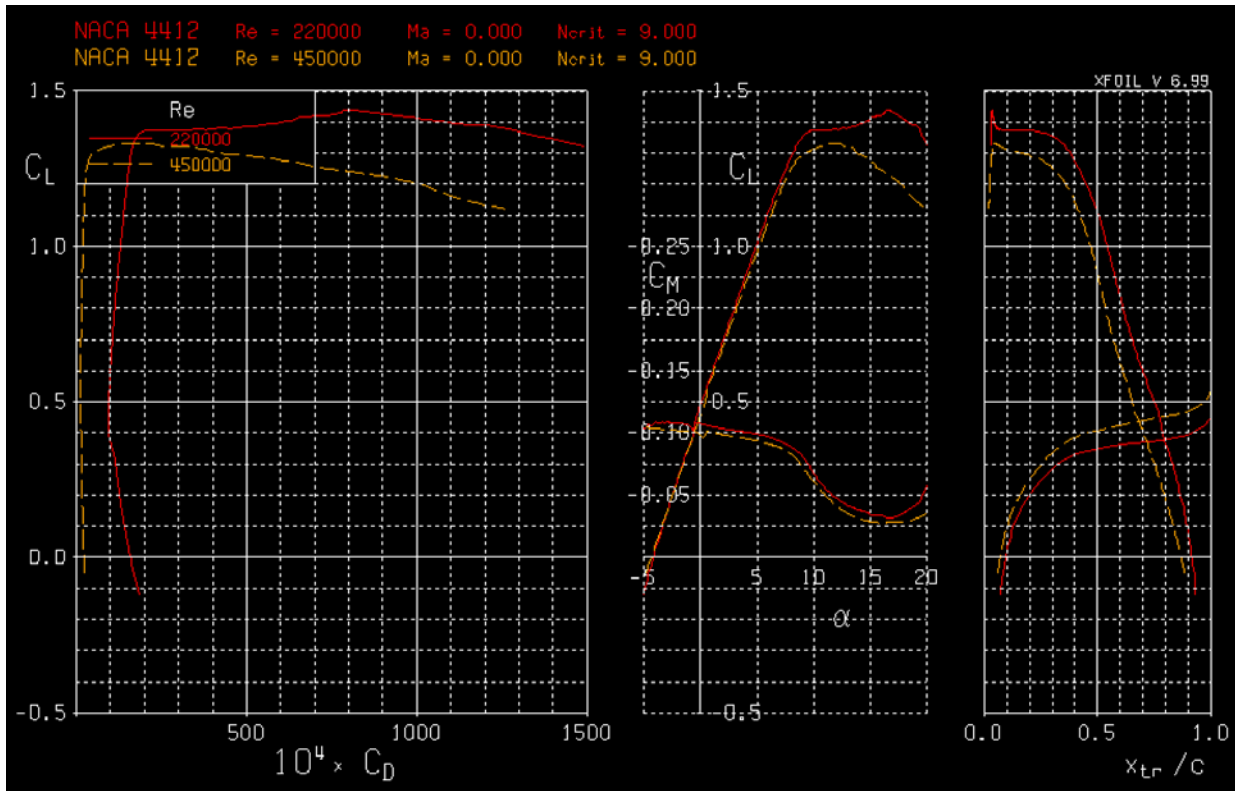


Figure 4.3 - Drag polar for the NACA 4412.

The drag polar analysis (Fig. 4.3) was conducted at a velocity of 22 m/s, 304 m MSL, and for two Reynolds numbers. The two Reynolds numbers differed according to the chord length at the wing root and tip. Angles of attack ranging from  $-5^\circ$  to  $+20^\circ$  in  $0.1^\circ$  increments served as the range for the drag polar analysis.

$$\begin{aligned}
 c_r &= 0.3 \\
 c_t &= 0.15 \\
 \rho_{304m\ MSL} &= 1.19\ \text{kg/m}^3 \\
 v &= 22\ \text{m/s} \\
 \mu &= 1.81\text{E-}5 \\
 Re_r &= 4.5\text{E}+5 \\
 Re_t &= 2.2\text{E}+5
 \end{aligned}$$

The angle of incidence between an aircraft wing and the freestream is approximately  $6^\circ$  for general aviation aircraft. According to the  $C_L$  v.  $\alpha$  graph in Fig. 4.3,  $C_L=1.2$  at  $\alpha=7.17^\circ$ . This allows for a maximum  $C_L$  of approximately 1.35 at  $\alpha=11^\circ$  for climbing and maneuvering purposes. Therefore, the desired  $\alpha_{\text{incidence}}$  is  $7.17^\circ$ .

Pressure distribution (Fig. 4.4) and skin friction (Fig. 4.5) were calculated at an angle of attack of  $7.17^\circ$ . At this angle of attack, there is a noticeable deviation in the pressure gradient along the upper length of the NACA 4415. The NACA 4412 exhibits a similar pattern but to a lesser extent.

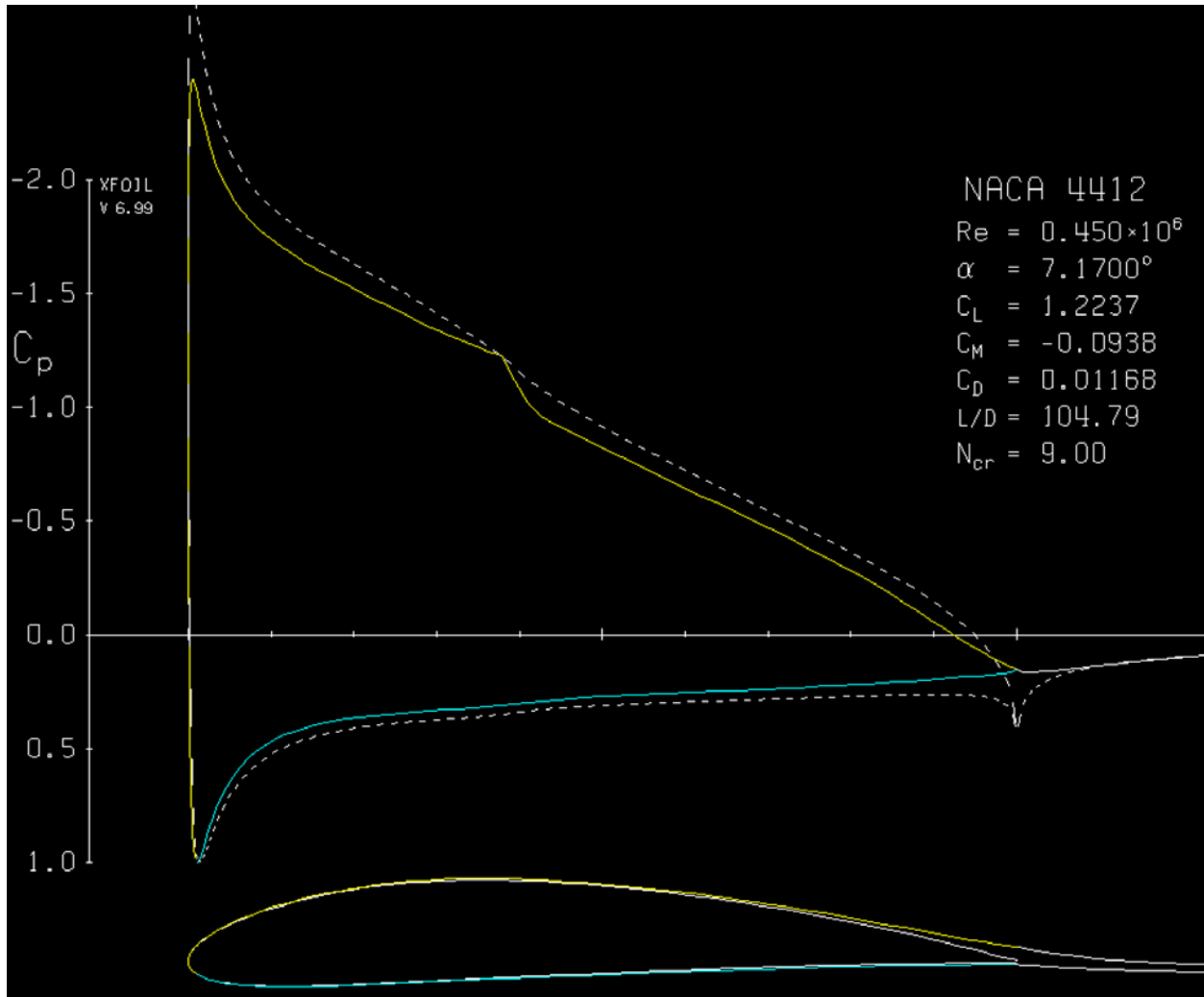


Figure 4.4 - Pressure distribution at  $\alpha=7.17^\circ$  for the NACA 4412.

Figure 4-4 identifies the point of transition at 0.4084c from the LE for the NACA 4415. This is due to a boundary layer that has previously been separated and has reattached as turbulent flow. Looking ahead of the transition point, the separation point can be identified in Fig. 4.4 where  $C_f=0$ . This occurs at approximately 0.33c.

Figure 4.4 also identifies a transition point for the NACA 4412 as 0.3787c. By assessing the skin friction coefficient in relation to chord length, skin friction appears to near a value of 0 at approximately 0.36. But the laminar flow transitions to turbulent without any separation. This is highlighted by the lift and drag numbers associated with the 4415 and 4412. The 4412 has 0.008 more  $C_l$  and 0.00063 less  $C_d$ . Although it may not seem like much, the results could be amplified at higher angles of attack.

The NACA 4412 was favored over the NACA 4415 since the thinner profile exhibited less drag and generated more lift while avoiding the creation of a separation bubble at cruise flight conditions.

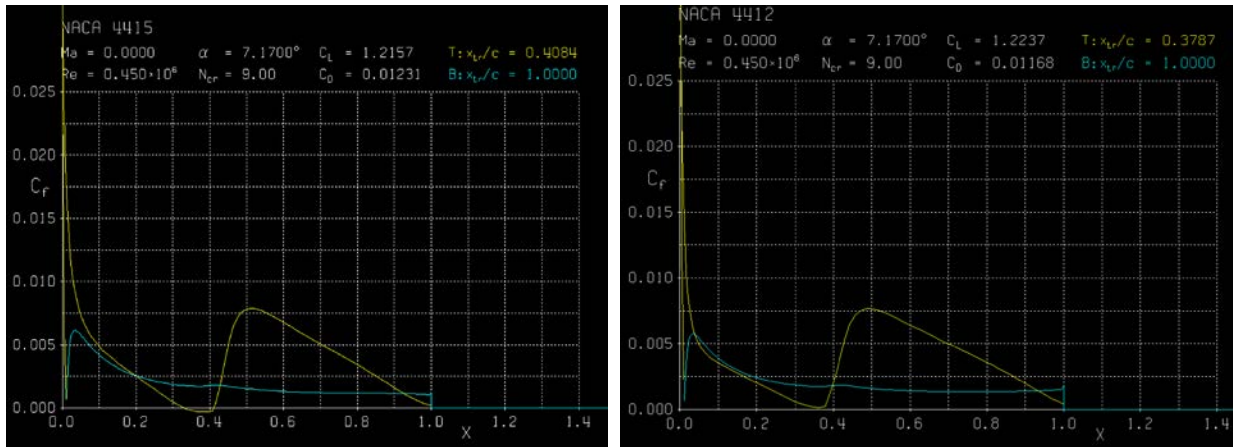


Figure 4.5 - Skin friction v. chord length at  $\alpha=7.17^\circ$  for the NACA 4415 (left) and NACA 4412 (right).

The area between possibly separated flow and reattaching as a turbulent boundary layer is also noticeable in the small bump along the pressure coefficient curve of the upper airfoil edge in Fig. 4.5. This is an area of importance for high endurance aircraft design when it comes to drag reduction. This area of detached flow contributes a considerable amount of drag that reduces the performance of the wing.

Having identified the location of the “separation bubble”, the aircraft designer may install a bump strip or blower along the wingspan and slightly ahead of this chord length. This results in the flow prematurely transitioning to turbulence prior to reaching the separation point. Although the turbulent layer increases drag over a laminar layer, the turbulence reduces the tendency of the boundary layer to separate due to the high energy present in the flow. Therefore, the boundary layer remains attached as turbulent flow and generates less drag. According to the Xfoil analysis at the given angle of attack at cruise, the bump strip should be placed at approximately  $0.3c$  from the leading edge for the NACA 4412.

Although separation does not appear to actually occur, the skin friction chart shows that it is on the verge of occurring. As a result, a minor change in flight conditions may catalyze the generation of a separation bubble. Therefore, it is advised to place a bump strip at  $0.3c$  along the length of the wing.

#### 4.3.8 Wing Analysis in AVL

##### 4.3.8.1 Configuration

The FANDECT is designed with a high mounted, trapezoidal, dihedral wing that exhibits hard stall tendencies at the wing root. The dihedral angle also promotes lateral stability since the light aircraft is highly susceptible to wind gusts.

A rough design estimation of the Reynolds number at the wing root (largest chord) and tip (smallest chord) generates the following:

$$\begin{aligned}
 Re &= \frac{\rho v c}{\mu} \\
 \rho_{0\text{MSL}} &= 1.225 \text{ kg/m}^3 \\
 v &= 20 \text{ m/s} \\
 c_{\text{root}} &= 0.300 \text{ m} \\
 c_{\text{tip}} &= 0.225 \text{ m} \\
 \lambda &= c_{\text{tip}}/c_{\text{root}} = 0.75 \\
 \mu &= 1.81e^{-5} \frac{\text{kg}}{\text{m} \cdot \text{s}} \\
 Re_{\text{root}} &= 0.41e^6 \\
 Re_{\text{tip}} &= 0.30e^6
 \end{aligned} \tag{4.22}$$

After reviewing similar aircraft in the literature review, an aspect ratio of 17 should provide a low enough drag profile for a high endurance aircraft while avoiding an extremely large wingspan.

#### 4.3.8.2 AVL analysis

The wing geometry was calculated with MATLAB.<sup>42</sup> The script identified (x,y,z) coordinates to be loaded into an .avl file. When loaded into AVL, the file depicted the wing geometry so that an aerodynamic analysis may be conducted.<sup>43</sup>

See Appendix B for the wing geometry parameters generated by MATLAB. See Appendix C for the wing geometry data imported into AVL.

General aviation commonly uses rectangular, trapezoidal, and elliptical wing planform designs. The rectangular design is by far the simplest and cheapest to manufacture. But the lack of a taper effect results in lift generation at the wingtips developing strong wing tip vortices that contribute to drag. As a result, the L/D ratio is penalized.

The lift distribution of a standard rectangular wing planform is depicted by the Trefftz plot in Fig. 4.6. Localized lift strongly correlates with the lift distribution across the wingspan. Lift is evenly distributed along approximately 70% of the center of the wing. The remaining 30% of the wing tapers off at the wing tips.

The wing tip vortices may be reduced by adding a taper effect along the wingspan. The reduction of surface area at the wingtips results in less lift generation and less vortex generation. This configuration, a trapezoidal planform, is a cheap and simple improvement to the rectangular planform. The elliptical planform further improves the L/D ratio by implementing a non-linear taper effect along the wingspan. Although aerodynamically more attractive, this method is the most costly and complex of the three mentioned. Therefore, the trapezoidal planform has been selected for the wing analysis.

As seen in Fig. 4.6, the trapezoidal planform increases the Oswald efficiency factor from 0.8944 (rectangular planform) to 0.9756. Even with less surface area (due to the introduction of a taper effect), the  $C_l$  increases by 0.0397 and  $C_d$  decreases by 0.0022.

But the localized lift coefficient deviates from the lift distribution curve at the wingtips. As a result, the wing is prone to experience a soft stall at the wingtips rather than a hard stall at the wing root.

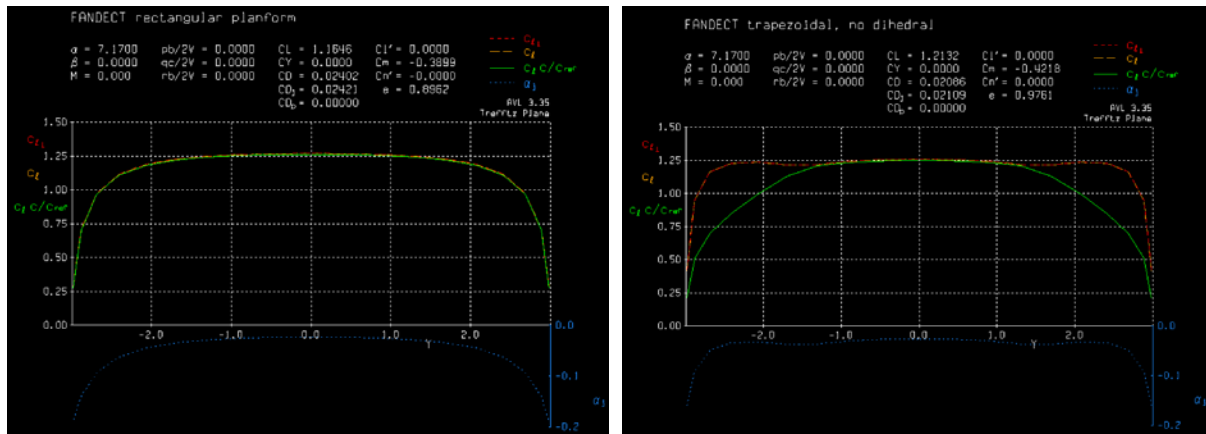


Figure 4.6 - Trefftz plot for a rectangular (left) and trapezoidal (right) wing planform.

Although ideal for lateral stability, a dihedral angle did little to improve the lift and drag characteristics of the trapezoidal planform. The Oswald efficiency number increased by 0.01 while lift and drag coefficient changes were nearly negligible. Figure 4.7 shows the Trefftz plot for the wing with a dihedral angle of 5° and 10°. While the 5° angle marginally increases the lift coefficient, the 10° angle shows a slight decrease over the 5° model. Still, the 10° dihedral angle provides an optimal Oswald efficiency number over both the 5° and 0° design.

Due to the optimal Oswald efficiency number and benefits of lateral stability in flight, the 10° dihedral angle was chosen as the desired parameter.

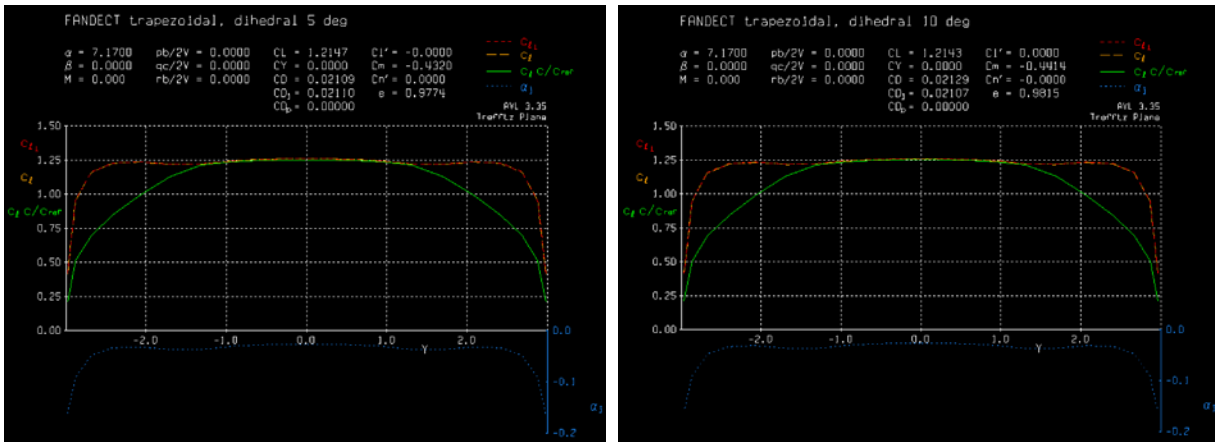


Figure 4.7 - Trefftz plot for a trapezoidal wing planform with a 5° (left) and 10° (right) dihedral angle.

Adding a taper effect between the root and wing tip chord results in an increase in the lift coefficient and oswald efficiency number at the expense of increasing the local lift coefficient near the wingtips. As seen in Fig. 4.8, increasing the taper effect to 0.25 results in the local lift coefficient of the wingtips exceeding that of the wing root.

If the wing begins to stall, the wingtips will experience a gradual stall creep first. Also, the wing is more prone to stall along the wingtips as it accelerates through a turn or maneuver since the wingtip is traveling faster than the rest of the wing. Therefore, a hard stall is preferred at the wing root which is more associated with a lack of taper effect. Unfortunately, the lift coefficient and oswald efficiency factor is deducted with this type of taper.

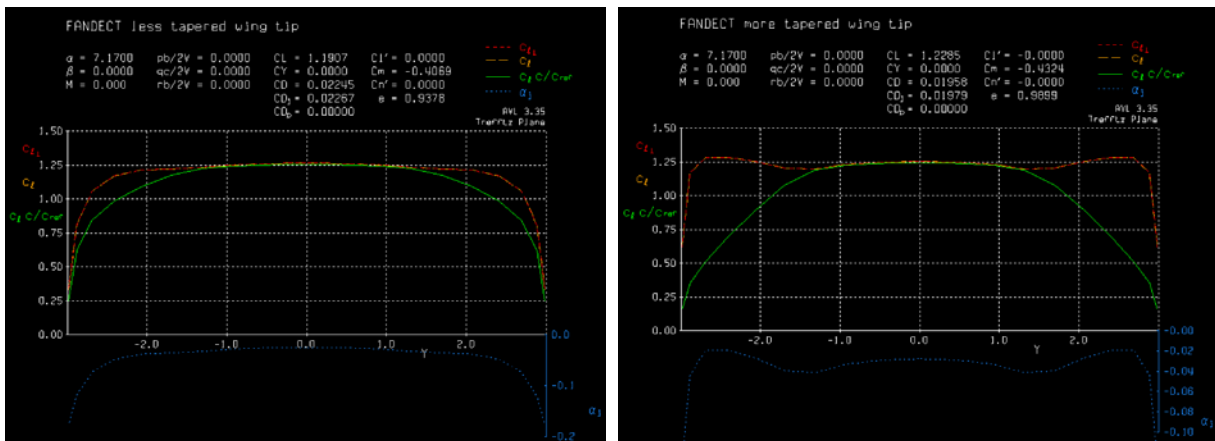


Figure 4.8 - Trefftz plot for a trapezoidal wing planform with less (left) and more (right) taper effect.

The span at which the trapezoidal planform extends across the wing also has an effect on the aerodynamic properties. The Trefftz plot in Fig. 4.9 consists of a trapezoidal planform that runs across 50% of the wingspan. The Trefftz plots in Fig. 4.9 exhibit a trapezoidal planform along 25% and 75% of the wingspan.

Noticeably, the lift coefficient and oswald efficiency number increase at the expense of the local lift coefficient creeping larger near the wingtips. Although undesirable, the amount of local lift coefficient increase is not as extreme as with an increase in taper effect. Therefore, an increase in trapezoidal area is somewhat more preferable than an increase in taper effect. Still, the increase in lift coefficient and oswald efficiency number is not as beneficial as that of a wing with an increased taper.

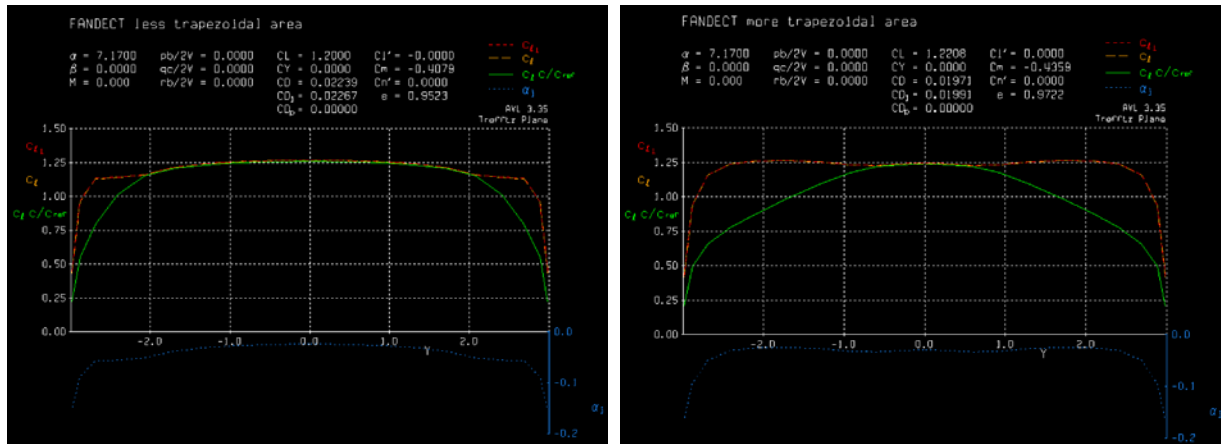


Figure 4.9 - Trefftz plot for a trapezoidal wing planform with less (left) and more (right) trapezoidal area.

While considering the benefits and drawbacks of changing the trapezoidal area and taper effect, a combination of the two parameters provide a synergistic effect. Increasing the trapezoidal planform area and dihedral angle while slightly decreasing the taper effect results in a local lift coefficient that remains highest near the center of the wing and decreases towards the wingtips. The Trefftz plot in Fig. 4.10 illustrates this effect with a wing that exhibits 65% trapezoidal planform along the wingspan, 0.45 taper, and a  $10^\circ$  dihedral angle.

The lift coefficient and oswald efficiency number are not as high as the most optimal individual cases but they are noticeably different from the standard trapezoidal planform in Fig. 4.6. The local lift coefficient is also distributed in a way that favors wing root stall over wingtip stall. Hence, the aerodynamic properties and lateral stability are improved while maintaining favorable stall conditions.

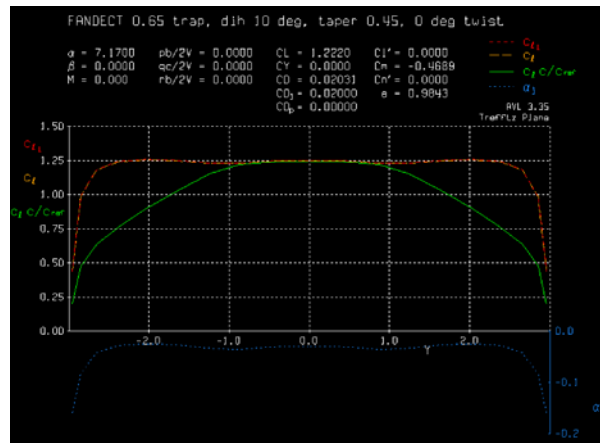


Figure 4.10 - Trefftz plot for a trapezoidal wing planform with 0.45 taper,  $10^\circ$  dihedral, and a larger trapezoidal area.

For the span of the rectangular planform section, the geometric twist shall be  $-0.5^\circ$ . For the span of the trapezoidal planform section, the geometric twist shall be  $-2^\circ$ . This promotes a higher angle of attack along the wing section adjacent to the root and a lower angle of attack towards the wingtips. A second study was conducted without any twist along the rectangular planform section but it resulted in a lower L/D ratio than the proposed twist of  $-0.5^\circ$ .

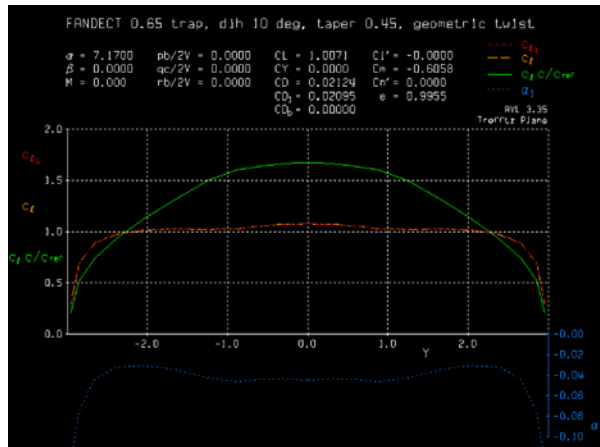


Figure 4.11 - Trefftz plot for a trapezoidal wing planform with 0.45 taper, 10° dihedral, a larger trapezoidal area, and a geometric twist of +2° along the span of varying chord length.

Although the lift coefficient decreases, this method increases the L/D ratio to 47.4 and increases the local lift coefficient at the wing root, thus promoting root stall over tip stall. The root chord was increased from 0.3 m to 0.468 m. This resulted in a change of AR from 22 to 15.4. Although this decreased the L/D ratio, the amount of lift generated increased without requiring a wingspan beyond 6 m. The final Trefftz plot (Fig. 4.11) shows the effects of geometric twist on lift distribution.

With the reasons stated above, the final geometric composition of the wing is illustrated in Fig. 4.12. The wing has been modeled with 65% of the length comprising a trapezoidal planform, 0.45 taper, 10° dihedral, a -0.5° geometric twist from the wing root to the trapezoidal area, and -2.0° geometric twist along the trapezoidal area.

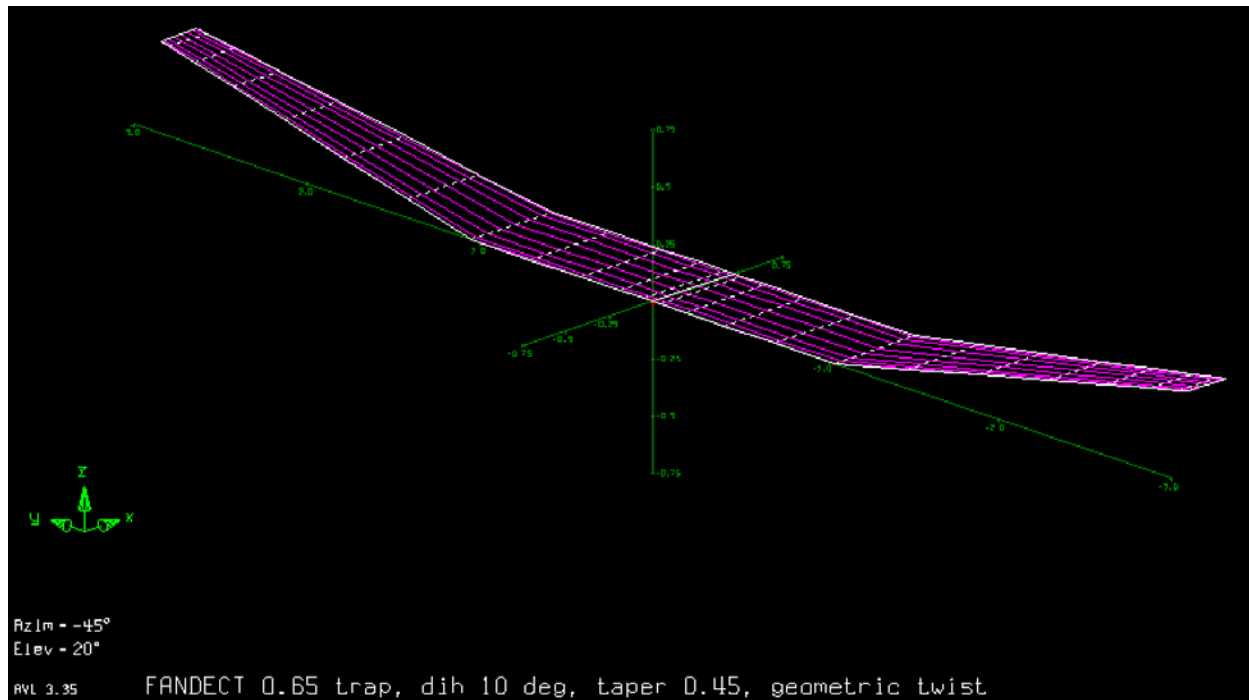


Figure 4.12 - Final wing geometry rendered in AVL. Note: the geometric twist does not appear in the AVL rendering.

Since the chord length at the root was changed, the Re increased to approximately 0.7E6. The NACA 4412 was re-analyzed with Xfoil at this Re and the skin friction coefficient still does not show the presence of a separation bubble. In fact, the transition from laminar to turbulence occurs at a higher skin friction coefficient, allowing for a safer buffer zone against reaching a value of 0 and generating a separation bubble.

The higher  $Re$  resulted in an increase in inertial forces as well as a more energized freestream. Although slightly, the flow is less likely to detach at cruise conditions. Still, a bump strip is recommended at  $0.3c$  from the leading edge to minimize separation conditions at higher angles of attack experienced in climbing and maneuvering.

#### 4.3.9 Landing Gear Design and Weight & Balance Analysis

Three landing gears are attached to the underbelly of the fuselage. One landing gear is located underneath the nose of the fuselage. Two landing gear are located slightly aft of the wing location and underneath the fuselage. The first generation of the FANDECT has fixed landing gear since the aircraft does not fly at high speeds. But future designs will incorporate retractable landing gear to minimize drag and improve endurance.

Contributing nearly 18% of total aircraft weight, the location of the battery bank heavily influences aircraft CG. The battery bank is positioned slightly forward of the rear landing gear but aft of the aerodynamic center. This minimizes the chance of the CG being located aft of the landing gear which could result in unwanted rotation during takeoff. Placing the battery bank aft of the aerodynamic center promotes a natural positive angle of attack in flight.

### 4.4 PRODUCTION

The FF production process is similar to the FR process. The greatest difference involves the material used for construction. The majority of the FR was constructed with 3D printed ABS. This is not the case with the FF since it is much larger in scale and experiences greater forces than the FR (lift, battery bank weight, landing shock).

#### 4.4.1 Material Properties

The FF is comprised of both isotropic and anisotropic material. Anisotropic material dominates the FF structure and critical mounting components. Isotropic components are primarily used for the linking mechanisms that mount the FR to the FF.

Electronics and small components are housed in the FF structure and held in place by 3D printed brackets. The brackets are small and individually designed according to the item being supported.

3D printed ABS is generated in an additive manufacturing process that results in a layered configuration. Due to the printing process, the object exhibits anisotropic properties. The layers are dictated by the user when the object is oriented in pre printing software. This results in a greater tensile strength parallel to the layer axis and a weak tensile strength normal to the layer axis. For example, longer items should be printed with layers oriented with the longest length. If not, the part tends to snap between layers when stress is experienced. Although not the most ideal, additive manufacturing has propelled rapid prototyping. Thus allowing engineers to test concepts on a small makeshift level prior to developing a more refined product.<sup>45</sup>

The FF structure is designed with composite material similar to that of the wing spar (see next section). Minimizing the weight of the FF structure results in the motors requiring less power to maintain level flight. Less of a power drain results in smaller battery banks and an increase in aircraft endurance. Since the FANDECT takes advantage of endurance to boost rotary wing operations, the improved endurance is an attractive parameter to boost.

#### 4.4.2 Wing Spar Analysis

The wing spar is expected to be constructed with aluminum. But if the aircraft requires a minor weight reduction, then the wing spar will be constructed with carbon fiber (std. grade).

The wing spar is comprised of an I cross section and spans the length of the wing. The isotropic version is designed with Al 2024-T351. See Table 4.2 for the isotropic properties.

Table 4.2 - Isotropic properties<sup>46,47</sup>

<b>Material properties</b>	Al 2024-T351
<b>Modulus of Elasticity</b>	73.1 GPa
<b>Shear Modulus</b>	28 GPa
<b>Ultimate Tensile Strength</b>	469 MPa
<b>Yield Strength</b>	345 MPa
<b>Fracture Toughness</b>	32 MPa-m <sup>1/2</sup>

The anisotropic version is designed with standard carbon fiber material in a  $[90^\circ 0^\circ]$  laminate configuration. See Table 4.3 for the anisotropic properties. The configuration provides strong tensile strength along the length of the

wingspan while minimizing bending effects due to lift generation and the weight of the FR subsystems and fuselage.

Table 4.3 - Anisotropic properties<sup>48</sup>

Material properties	Carbon fiber (std. grade)
Density	1.6 g/cm <sup>3</sup>
E <sub>1</sub>	175 GPa
E <sub>2</sub>	8 GPa
G <sub>12</sub>	5 GPa
v <sub>12</sub>	0.30
s <sub>1</sub>	1000 MPa
s <sub>2</sub>	40 MPa
s <sub>12</sub>	60 MPa
α <sub>1</sub>	-0.3
α <sub>2</sub>	25

## 5. SOFTWARE

### 5.1 DESCRIPTION

The FANDECT exists as a multitude of subsystems comprised of one FF and multiple FRs. What makes the FANDECT unique is the FR capability to act an independent system when disengaged from the FF. To achieve such independency, each subsystem has a dedicated microcomputer. The microcomputer is outfitted with WiFi and bluetooth which allows the subsystems to create a communications network within the FANDECT.

To achieve this operational network, each microcomputer has communications and component control software installed. The bulk of the software is comprised of the operating system and standard operating functions. The remaining software consists of scripts programmed for manual and autonomous flight mode operation.

### 5.2 GENERAL OPERATION

The FR operates on a Debian based OS, Raspbian Stretch with PIXEL, optimized for Raspberry Pi 3 operation.<sup>49</sup> The operating system is Unix-like since it shares many graphical similarities and functions with the Unix OS.

#### 5.2.1 Programming Software

Several programs were scripted to aid in FR operation. All general, manual, and autonomous scripts have been written in Python. Being a general purpose programming language, Python provides a simple and clean platform to generate script for basic operations. In comparison to C++ or Java, Python is capable of expressing commands in fewer lines with a minimalist syntax.<sup>50</sup> Python has also been a popular programming language for the Raspberry Pi community. Therefore, many open source libraries already exist to support hobbyists.

Currently, Python can be written in either 2.0 or 3.0. Released in 2000, Python 2.0 was a major upgrade to the original Python released in 1991 by Guido van Rossum. Python 3.0 was released in 2008 and is easier to grasp for users new to Python.<sup>51</sup> Still, the library support for 3.0 is not as strong as the support for 2.0. Due to the numerous libraries already written in Python 2.0, the FANDECT scripts have also been written in 2.0.

The software was developed in the IDE known as IDLE.<sup>52</sup> IDLE is a development environment that is generally bundled with Raspberry Pi software. The environment is color coded which allows for ease with navigating script. The software also provides the programmer with tool tips, autocompletion options, and a debugger.

#### 5.2.2 Communication

The FR operates without the need for any external physical connections due to the use of onboard batteries for power and the WiFi/bluetooth capabilities of the microcomputer for communication. Upon startup, the FR logs in to a pre-designated local network. The user identifies the FR by the local IP address.

With the known local IP address, the user may access the FR from their personal laptop wirelessly through an SSH client. The SSH client PuTTY is open source software that is readily available and compatible with the Windows OS that is installed on the user laptop.<sup>53</sup>

Once the user accesses the FR via SSH, a username and password are required to access the terminal prompt. At the terminal prompt, the user may access either the manual or autonomous python script to begin FR operation.

### 5.3 MANUAL MODE

Manual mode is generally used to conduct flight tests and systems checks and is therefore the secondary mode for FR operation. In manual mode, user transmits control signals via Wifi to the microcomputer. The microcomputer processes the requests and sends corresponding digital signals to the FR subsystems via hard wired GPIO pins. By operating a wireless handheld controller, the user may control the flaps, motors, and cam onboard the FR.

The FR manual mode script is located in Appendix B.

#### 5.3.1 Controller

The Microsoft Xbox 360 wireless controller is used for FR operation in manual mode. In comparison to other controllers, the 360 controller has more open source software support for the Raspberry Pi community. The controller also has numerous buttons and joysticks that can control the multiple features of the FR.

The driver named “xboxdrv” served as an open source Python library capable of receiving controller input and outputting a numerical response.<sup>54</sup> The numerical response is translated by the microcomputer into an action that physically manipulates the FR subsystems. In Table 5.1, each controller feature is listed with the numerical range and subsystem that it manipulates.

Table 5.1 - Controller Input/Output

Controller Feature	Controller Range	FR Feature	FR Component
Button: Xbox	0/1	Turn on Controller	N/A
Button: Select	0/1	Stop Program	All
Button: Start	0/1	Comm Check/Start	N/A
Joystick L-X	-1.0 - +1.0	Yaw	Motor
Joystick L-Y	0.0 - +1.0	Thrust	Motor
Joystick R-X	-1.0 - +1.0	Roll	Servo
Joystick R-Y	-1.0 - +1.0	Pitch	Servo
Gamepad: Up	0/1	Cargo Handling	Servo
Gamepad: Dn	0/1	Cargo Handling	Servo
Gamepad: L	0/1	Cargo Handling	Servo
Gamepad: R	0/1	Cargo Handling	Servo
Button: A	0/1	Trim On/Off	Motor/Servo
Button: B	0/1	Camera: Tilt Down/Stow	Servo
Button: X	0/1	Position Lights	LED
Button: Y	0/1	Anti-Collision Lights	LED
Button: L	0/1	Cargo Release	Servo
Button: R	0/1	Audio	Speaker
Trigger: L	0.0 - +1.0	Undefined	N/A
Trigger: R	0.0 - +1.0	Undefined	N/A

Although the y axis of the left joystick is capable of outputting a range from -1.0 to +1.0, only 0.0 to +1.0 is used for throttle control. The joystick naturally sits at 0.0. Therefore, that is the designated location for setting thrust at 0%.

#### 5.3.2 Pitch and Roll

Pitch is controlled with the right joystick y axis. Roll is controlled with the right joystick x axis. When the microcomputer receives a numerical input from the right joystick, the number is translated to a PWM signal. If the joystick is not moving, a numerical input of 0 translates to a PWM signal of 0 (off). If the joystick is moved to the maximum position, a numerical input of +1.0 translates to the largest PWM signal. At a maximum value, the servo rotates to the maximum clockwise position. As a result, the flap is deployed 60 degrees from the stowed position. This places the flap into the freestream behind the motors, creating a pitching moment generated from the

form drag.

The translation from controller signal to PWM signal is conducted as a linear relation. Therefore, the same amount of controller input from 0 to 0.1 will result in the same amount of flap deflection experienced from 0.9 to 1.0. Eventually, an exponential relation will be desired with an input near 0 resulting in a small flap response and an input near 1.0 resulting in a greater flap response. This provides the user with a less sensitive control input when no move is desired. When the user inputs a demand for greater control movement, the response will be much greater.

### 5.3.3 Thrust and Yaw

The motors are controlled in the same manner as the servos. The motors are controlled with the left joystick +y axis. The left joystick +y axis position is sent as a number to the Raspberry Pi. The script translates the number into a PWM parameter and sends the value to the two ESCs. The ESCs translate the parameter to a motor rotational value of 0 to 100%.

Yaw is controlled with the left joystick x axis. If a yaw signal is entered with the left joystick x axis, then it is translated in the same way and delivered to the ESCs. But the signal to one ESC is decreased by 5% in relation to the signal sent to the other ESC. This results in asymmetric RPM. Without an even torque generated by both motors, the excess torque of one motor will translate to the FR structure in the form of rotation.

The top motor rotates counter-clockwise and the FR structure responds by rotating clockwise. The bottom motor rotates clockwise with an FR response in the counterclockwise direction. When both motors are generating an equal amount of torque to counter one another, the FR structure remains static.

If the RPM of the bottom motor is reduced, the excess torque generated by the top motor will translate to the FR structure. Therefore, decreasing the RPM of the bottom motor results in a right yaw of the FR. Vice versa, decreasing the RPM of the top motor results in a left yaw of the FR. RPM is decreased instead of increased to avoid over torquing the motors at the maximum power setting.

### 5.3.4 Miscellaneous Controller Functions

The Xbox button turns on the controller.

The select button halts the program, returns the flaps to the retracted position, and stops the motors.

When the manual mode program is initiated, the start button must be pressed to unlock access to the controls. This also serves as a communication check between the FR and the Xbox controller.

The 4 arrow gamepad will be used for cargo handling. It has not yet been implemented.

The A button records the last set of control parameters and enters an infinite loop while maintaining the parameters. The loop is broken by pressing the A button again. This functions similar to an aircraft trim system when the pilot requires the controls to maintain the position they were last trimmed at.

The B button tilts the PixyCam out and downwards to look past the aft section of the FR. Pressing the B button again stows the PixyCam in the original position flush with the outer shell of the FR.

The X button turns the position lights on and off. Green and red position lights are used to provide the user with FR alignment.

The Y button turns the anti-collision lights on and off. The anti-collision lights provide the user and others in the area with an awareness of the FR location.

The Left button initiates the cargo release procedure.

Holding down the right button will turn on a high pitch speaker. The loud audio beep assists the user in looking for the FR in flight or while searching after a crash.

Left/right triggers are undefined.

## 5.4 AUTONOMOUS MODE

Autonomous mode is the primary mode for FR operation. Autonomous control requires that the FANDECT conduct mission requests by processing visual data and independently calculating all necessary movements. With respect to safety, autonomous mode may be overridden by pressing the designated override button on the handheld controller. At this point, autonomous mode ends and the user takes full control in manual mode.

### 5.4.1 Visual Input

Currently, the FR follows a pre-scripted flight route that provides guidance to and from the FF. Obstacle avoidance and GPS tracking will be implemented for actual operation. This report focuses on developing the technology associated with accurate package delivery and FR retrieval. The PixyCam is involved in both procedures by providing real time visual data.

The PixyCam is located on the aft side of the FR. At a hover, the camera is pointing at the horizon. As the FR

tilts in flight, the camera is positioned upwards. When the FR is conducting an approach to the FF for docking, the camera will be naturally facing the underside of the FF.

During cargo delivery, the FR is aligned in an upwards position. The camera may be tilted out and downwards by 90 degrees so that the ground is in view. By using the same color tracking methods involved in FR docking operations, the FR can identify and begin an approach towards a marked LZ. The LZ is expected to be marked by a 2x2 m bright orange square. The square will be similar in material and brightness to the VS17 panel used in the military for marking equipment and signaling to search and rescue crews.

#### 5.4.2 Standard Flight

While the FR is flying to and from the FF and LZ, the flaps and motors respond in a manner similar to what is detailed in manual mode. For the first generation of the FR, the maneuvering is pre scripted and executed according to a list detailing system activation, degree of activation, and time of action. For example, slightly rolling to the right will involve activating the right side servo, applying a PWM signal that involves a 20 degree deployment of the right flap, wait 0.5 sec, then retract the flap.

#### 5.4.3 Landing & Approach

While prescribed movement may be suitable for straight and level flight across open space, it is not used for landings and FF approaches. The visual data streamed by the PixyCam and hardwired directly to the onboard microcomputer provides the FR with high integrity and real time data.

The objective of landings and approaches are to close in on high contrasting square objects. The matrix of data sent by the PixyCam identifies where the color is located on the screen with respect to pixels. When a square color is identified, the center of the square can be calculated by using the maximum and minimum values located across the x and y axis. The x,y cartesian coordinate of the center of the square becomes the vital data necessary to translate into subsystem instructions.

The FR autonomous mode script for retrieving the color block data is located in Appendix C.

Tables 5.2 shows the difference in control movement between landing and FF approach. Adjusting the controls in an attempt to align the coordinates on the center of the screen is similar to an ILS approach that pilots conduct during instrument flight.

Note that the PixyCam is located on the aft section of the FR. When the PixyCam is deployed during landing, the bottom of the screen is near the FR body and the top of the screen is away from the FR.

Table 5.2 - Center Coordinate Translation

Square Location from Center Screen	Adjustment for Landings	Adjustment for FF Approaches
Up	Deploy Aft Flap	Increase Thrust
Down	Deploy Front Flap	Decrease Thrust
Left	Deploy Right Flap	Deploy Right Flap
Right	Deploy Left Flap	Deploy Left Flap

## 6. SYSTEM OPTIMIZATION

### 6.1 DESCRIPTION

After completing a preliminary design for the FR and FF systems, performance criteria was matched with mission requirements. The FR lacked the thrust required to achieve hover, processing power to refine and execute user commands, and an effective communication system beyond short range LOS.

### 6.2 PROPULSION SYSTEM

#### 6.2.1 Propeller

The original 3 blade propeller lacked the characteristics necessary to generate enough lift for flight. The rotor disk is confined to a diameter of 225 mm. With the inability to extend rotor blade length to generate more lift, the blade chord and pitch were increased. The number of blades were also increased from 3 to 5 and finally to 8.

As a result, each blade generated more lift but also more drag. The original BLDC motors lacked the torque

necessary to maintain the 5 blade propeller rotating at 100% power.

Structurally, the base of the propeller was undersized and rotational tests resulted in the 5 blade configuration fracturing at the root of each blade. The taper effect at the root of each blade also contributed to cracks developing along that section with each use. The buildup of cracks resulted in a failure after approximately 12 test cycles. One test cycle involved accelerating the motor to 100%, maintaining rotation for 5 seconds, and then decelerating the motor to 0%.

The new 8 blade configuration is not designed with a taper effect primarily to improve the structural integrity at the blade roots. The base diameter has been increased from 30 cm to 50 cm to provide a sturdier platform to attach the blades. The larger cross section does little to increase form drag in forward flight since the size matches the cross section of the new and larger motors.

### 6.2.2 Motor

The original BLDC motors lacked the torque necessary to rotate the new 5 blade configuration at maximum power. The original motors were incapable of maintaining 100% power without overheating and smoking. Therefore, new motors were installed that generated more torque.

The new BLDC motor is the T-Motor U7 420kv. Although heavier than the ST3007 1100kv, it is far more capable at maintaining an RPM setting under higher drag conditions.<sup>55</sup> It is for this reason that this motor type is generally installed on heavier drones (approx. 20 kg).

## 6.3 CONTROLLERS

### 6.3.1 ESC

To deliver the amperage necessary for the two new BLDC motors, two new ESCs were required. The new ESC is the T-Motor 80A Flame.<sup>56</sup> The original ESC was rated at 20A.

Although the new motor requires a rating of 40A, the 80A Flame has received excellent consumer reviews. Also, an 80A rating allows the user to upgrade the FR with even higher torque motors in the future if necessary. The 80A flame is also excellent at dissipating heat generated from controlling the 420kv motors.

### 6.3.2 Microcomputer

Although compact, the Raspberry Pi Zero W lacked the processing power to manage numerous programs at a calculating speed optimal to process every user request. While running the manual mode script, approximately 70% of control requests were being processed due to the lag experienced by overloading the processor. The Zero W was upgraded to the Raspberry Pi 3 Model B (see Table 6.1 for comparison).<sup>57</sup> Running the same script, approximately 95% of control requests were being processed.

Table 6.1 - Raspberry Pi Zero W v. Model 3B<sup>58</sup>

Property	Zero W	3B
Price	USD\$10	USD\$35
SOC	Broadcom BCM2835	Broadcom BCM2837
# Cores	1	4
GPU	VideoCore IV	VideoCore IV 1080p@30
CPU Clock	1 GHz	1.2 GHz
RAM	512 MB	1 GB
Weight	9 g	45 g
Power	180 mA	1340 mA

The greater processing power of the 3B comes with a tradeoff in cost, weight, and power consumption. In comparison to the Zero W, the 3B is 3.5 times costlier, five times heavier, and consumes 7.4 times as much power. Still, the demand for more processing power outweighs these penalties. Processing power is directly related to aircraft control integrity which is necessary to conduct a successful flight.

## 6.4 POWER

### 6.4.1 Power Distribution Board

Due to the motor and ESC upgrades, a new power distribution board was required to handle the higher amperage level. The previous PDB was rated to handle 25A due to the wire gauge and terminal size.

The new PDB is the Lumenier 4Power Quick Swap. The PDB has solderless terminals that allow for quick swapping between ESCs and the design is capable of handling a far greater amperage rating.<sup>59</sup>

### 6.4.2 Battery

Battery configuration went through two iterations. The original batteries were individually capable of handling the original motor configuration. Two batteries were installed to balance the CG of the FR. When wired in parallel, the batteries doubled the flight time.

But the new motors are capable of generating greater torque at higher voltage. Wiring the batteries in series doubled the voltage from 11.1V to 22.2V but halved the flight time experienced in the parallel configuration. If the flight time is too short for future operations, larger batteries will be installed and wired in parallel to once again double the flight time.

Note that the flight time is not perfectly doubled since an addition of another battery increases total FR weight. As a result, the added weight requires the motors to work at a higher power rating and drain the batteries faster.

Still, this configuration did not deliver the level of amperage required at 100% motor operation. The max amp level required was compared with the max amp level provided with the current configuration.

Required Current for FR Operation:

$$\begin{aligned} I_m &= 40A \\ n_m &= 2 \\ I_s &= 0.21A \\ n_s &= 4 \\ I_{mc} &= 1A \\ FOS_A &= 1.15 \\ I_{FR} &= FOS_A (I_m n_m + I_s n_s + I_{mc}) \\ I_{FR} &= 95A \end{aligned} \tag{6.1}$$

#### 6.4.2.1 Battery configuration #1

$$\begin{aligned} n_B &= 2 \\ m_B &= 0.168kg \\ m_{B,total} &= 0.336kg \\ \text{Operational Range per Cell} &: 3.35 - 4.05V \\ \text{Operational Range (3 cells)} &: 10.05 - 12.15V \\ I &= Ah * C \\ 2.200Ah \\ 25C \\ I &= 55A \\ I - I_{FR} &= -40A \end{aligned} \tag{6.2}$$

Configuration 1 lacked the amperage rating required by 40A at 100% motor operation. Therefore, a new battery configuration was required that delivered at least 95A and met the motor criteria. At optimal operation, the motor requires 40A and 25V delivered by an 8S lipo battery.

Since the batteries are some of the heaviest components in the FR, two 4S batteries are connected in series to mimic the 8S configuration. When the 4S batteries are placed on opposite sides within the FR shell, the CG is more centered.

A longer operational time is also desirable so amp-hour ratings greater than the initial 2200mAh were reviewed. A 5000mAh battery provides longer operational time but the mass is close to 0.750kg. A 4000mAh battery is nearly twice as great as the initial configuration and has a mass of approximately 0.450kg (almost twice as light as the 5000mAh battery).

The Turnigy Nano-Tech 4000mAh 4S 25-50C lipo battery pack has an optimal amperage rating (100A), voltage rating (25V with two batteries in series), operational time (4000mAh), and mass (0.432kg).<sup>60</sup>

#### 6.4.2.2 Battery configuration #2

$$n_B = 2$$

$$m_B = 0.395kg$$

$$m_{B,total} = 0.790kg$$

*Operational Range (4 cells): 13.4 – 16.2V*

*4.0Ah*

*25C constant*

*50C burst*

$$I_C = 100A$$

$$I_B = 200A$$

$$I_C - I_{FR} = 5A$$

A surplus amperage rating of 5A at 100% motor operation exists with the second configuration. But the mass of the new battery configuration is increased by 135%. Although the battery mass increases, the motors are now capable of operating at 100%. Since the first configuration lacked the additional 40A necessary to run the FR at maximum operation, an assumption can be made that each of the two motors lacked 20A. Since each motor requires 40A for maximum operation, 20A would provide the system with 50% motor operation. The new configuration nearly doubles motor performance. Thus, the greater torque and rotational velocity generate more thrust which compensates for the increase in mass.

As the battery drain rate changes with the new configuration, the propeller design will be revisited. While maintaining the diameter restriction, the pitch, twist, and # of blades will be increased. Although each one of these parameters will increase drag, an optimal balance will be achieved that does not degrade the battery drain rate beyond a nominal amount (10% decrease in operational time). An increase in thrust results in greater maneuverability and an increase in maximum velocity.

Since the FR is designed to deliver a package and immediately return to the FF, maneuverability is favored over flight time. Maneuverability allows the FR to respond immediately to corrective control variables during descent and especially during retrieval.

During FR retrieval, the FR and FF match velocities. A higher FR maximum velocity results in the FF maintaining a higher cruise velocity. This prevents the FF from decelerating and nearing stall conditions due to a high angle of attack to generate the lift necessary at a low velocity. With the FF cruising at a higher velocity, more lift is generated which can translate to either a larger battery bank or a smaller wing planform if aircraft size is an issue.

### 6.5 COMMUNICATION

A lack of a mid to long range communication system prevents the FANDECT from conducting live testing beyond hover demonstrations. Mid to long range coverage is vital to test the FANDECT in a traffic pattern where FR deployment can be demonstrated while under the control of a user with a strong communication signal. The FANDECT project will undergo 3 stages of communication development. The levels progress communication range from short range (5 m) to mid range (30 km) and finally long range (any area with a data signal).

#### 6.5.1 Short Range

In the first stage, the microcomputer is accessed via Wi-Fi which is limited to a range of 32 m. The controller is connected through bluetooth which is limited to 100 m. Therefore, the Wi-Fi limits FANDECT operation to 32 m. Although unnecessary for autonomous operation, the controller should always be available during the development stages. The user might have to take over FANDECT control in the event of a hardware failure or an undiscovered bug in the software.

#### 6.5.2 Mid Range

The mid range stage implements the LoRa module as the primary mode of communication. The LoRa module provides a component with long range data transmission. It is capable of transmitting across 22 km with LOS and 2 km in an urban environment. It is compatible with the Raspberry Pi, lightweight, and compact enough to fit in the FR subsystem.<sup>61</sup>

#### 6.5.3 Long Range

The long range stage involves connecting the FANDECT to a cellular signal. The FR communicates with the FF via LoRa transmission. The FANDECT delivers and receives updates through use of the local cellular coverage. Therefore, the FANDECT is capable of operating in areas with cellular coverage. This can be further improved with

the use of satellite communication equipment installed in the FF. Areas of minimal to no cellular coverage may result in dropped connections. Satellite communication improves connection integrity and provides the user with constant updates and control.

## **7. ANALYSIS & SUMMARY**

### **7.1 ANALYSIS**

Serving as the critical feature of the FANDECT, the FR underwent a flight test to assess general functionality, stability, and structural design. The flight test was performed in manual mode with the use of auto stabilization and user command input.

#### **7.1.1 General Functionality**

A ground run was conducted on the FR prior to the flight test. The power distribution system, processor, control surfaces, and motors all indicated responsiveness to the application of battery power. LOS short range communication was optimal and response times of the control surfaces and motors were instantaneous. A full controls sweep was conducted and the control surfaces deployed to a maximum 90 degree angle from the surface of the shell for maximum drag. The control surfaces and propellers cleared the FR structure and rotated without interference. From startup to shutdown, the basic control of the FR was as expected.

#### **7.1.2 FR Auto Stabilization**

Auto stabilization provides the FR with the ability to maintain position with zero angular velocity in all axes and zero drift at a level of thrust selected by the user. The FR auto stabilization test involved manually increasing motor RPM until the FR generated enough thrust to achieve a 1 ft hover. No other controls were manipulated by the user. The FR was able to achieve a 1 ft hover for an average of 5 seconds.

Several factors prevented the FR from maintaining a hover beyond 5 seconds. The mass distribution resulted in a semi balanced system. The left and right sections were balanced but had more mass than the front and back sections. When the aircraft experienced a drift to the left or right, the control surfaces would extend further and for a longer time to correct the drift.

Control surfaces reacted instantaneously when applying corrective actions to maintain position and minimize angular velocity. If a drift or tilt correction was necessary, the control surfaces immediately began to increment towards full deployment until the FR returned to a stable profile. As described in the next section, an issue was identified with the lack of control surface effectiveness due to sizing.

Yaw control was the most effective feature of the auto stabilization. The FR received the angular velocity data associated with yaw from the IMU and adjusted the RPM of the stronger motor to zeroize any uncommanded yaw rate. Upon achieving a hover, the FR held heading without delay.

#### **7.1.3 User Command Input**

User command input was tested by manipulating the thrust and control surfaces of the FR remotely. When a command is sent to adjust the control surfaces, the FR auto stabilization is overridden and the user assumes full control authority. Full authority stops when the FR no longer receives a signal for the control surface. At that moment, the auto stabilization mode immediately takes over.

During this test, another issue was identified with the control surfaces deploying to counteract a roll to the left or right. The surface area of the control surface was not large enough to provide effective control during all maneuvers. When the FR was rolled to the left or right at a high angular velocity, full deployment of a control surface would not be sufficient to roll the FR back in the opposite direction.

#### **7.1.4 Structural Design**

The shell that housed the components proved to be a stable structure that did not experience fatigue under hovering conditions and landing. The shell could be made thinner to decrease overall FR mass.

The weak point of the structure resided where the four motor support beams attached to the shell. These four sections bear the weight of the structure pulling downwards and the thrust generated by the motors pulling upwards. During hard landings, the four sections also experienced a sharp shearing motion due to the centralized heavy motors exerting a force downwards at the moment of landing. The shearing across the circular cross section of the support beams is what resulted in the FR experiencing critical damage and no longer being operational.

#### **7.1.5 Critical Damage Test**

During a hover test, the FR was experiencing an outward spiral motion. The user attempted to override the auto

stabilization mode and directly command the control surfaces. The outward spiral could not be suppressed and the user executed a rapid descent. Upon contact with the ground, the four struts sheared at the points of contact with the shell. Loose from the main structure, the motors made contact with the ground and the propellers shattered upon contact with the inner shell. The propellers rotating at a high RPM resulted in the destruction of several of the inner shell panels.

Due to the chain reaction of events that followed the shearing of the support beams, greater consideration must be given to design of the support beams. This involves increasing the material cross section at the point of contact with the shell as a means to sustain harder landings. Ideally, a vertical shock absorption system should be placed at each support beam. This will absorb the downward force of the landing instead of translating it directly to the shell. Although designed to support and safeguard the FR components, the shell was not designed to withstand rapid moments of shock. The installation of a shock absorption system could be a more suitable alternative to increasing the width of structural components to make them more shock resistant. An increase in structural thickness could increase the weight drastically and serve to exacerbate the force experienced during a hard landing.

Another solution would be to reconsider how the part was printed. The 3D printed ABS support beam can bend and withstand low levels of shock. But due to how the part was printed, the layers ran parallel to the cross section of the beam. Therefore, the layers were oriented to receive the maximum shear force at the weakest point of the support beam. With the shear force acting directly between the layers, a crack could have developed between the layers where the least amount of bonding occurred during 3D printing. Printing the support beam so that the layers are printed across the long axis could significantly increase the resistance to a downward shear force.

## 7.2 SUMMARY

The FANDECT delivery system is a concept that competes with the maneuverability of a helicopter. Rotary wing aircraft operate in a rugged profile where hard landings are likely and control in confined areas is necessary to avoid a blade strike. In order to be a feasible alternative, the FR must have a sturdy structure capable of executing the user's intent with a slim error margin. This translates to the FR conducting maneuvers within a tolerance of 1 cm if the unit plans to deploy and return to the fixed wing pylon without damaging any subcomponents.

The FR requires a redesign of critical structural components such as the support beams. When assessing the stress in the support beams, the factor of safety should be increased to compensate for harder landings. Since the FR has nearly negligible gliding capability, any sort of precautionary landing could result in a hard landing.

The FR also requires a redesign of the control surfaces to make pitch and roll more commands more responsive. The subsystem could be more responsive if the control surface size is increased. The increase in drag will amplify the pitching moment and result in an FR that is more reactive to pitch and roll changes.

The FR also requires an improved auto stabilization system to minimize the outward spiral. If the control surfaces are larger and the mass distribution is more evenly distributed about the center, then the FR could experience a stable vertical descent that is 100% controlled by the auto stabilization system. Ideally, the FR approach from the FANDECT pylon to the ground would be under full autonomous control in order to react to minor disturbances (i.e. gusts) far more rapidly effectively than a human could. Minor automated control surface and motor adjustments result in a faster round trip while draining less battery power.

## 7.3 FUTURE INTENT

The FANDECT is held back due to the instability of the FR subsystem. Without a stable FR, the FANDECT will be unable to safely attach and detach the system in flight. Without the ability to attach to the lift generating surface of the FF, the FR loses the ability to travel long range in an energy saving profile. The FR would then be no more unique than a small commercial drone on the market. Therefore, the FR has two likely paths that can be taken to address the issue.

The auto stabilization script requires a finely tuned integral controller. The script currently lacks the ability to accurately keep track of distance displacement over time. When the FR experiences minor drifting, the movement goes unchecked since the acceleration is registered as residing within a tolerable level. Once the FR can monitor displacement accurately, then adjustments can be made during the approach to the FF pylon that will guide the FR to the electromagnetic mounting system. Without the integral controller, the FR will navigate solely on the positioning of color panels observed with the onboard Pixycam. Although the computer vision will bring the FR close to the FF, the inability to correct for unintended drift will make mounting the pylon a dangerous operation that could instead result in the FR making contact with the wing.

Redesign of the FR subsystem is another viable approach. The FR carries a lot of mass in the outer shell and that serves as the primary obstacle for stability. It also means the pitching moment becomes stronger to overcome due to the displacement of mass several centimeters away from the vertical axis. If the FR had the mass directly located along

the vertical axis, then the subsystem would be much more stable. It will have a tendency to return to a naturally stable state after experiencing a pitch or roll command. The mss would be underslung below the two contra-rotating motors and would be clear of the propellers. One problem stems from the loss of the outer shell that protects the propeller from making contact especially during an approach to the FF pylon. Ideally, an FR with an underslung subcomponent compartment would provide the stability necessary to deliver cargo to a pinpoint location on the ground and return to the fixed wing system in the air.

## References

### Introduction

1. Boeing, V-22 Osprey: Unlike any aircraft in the world, 2016, URL: <<http://www.boeing.com/defense/v-22-osprey/>>.
2. Amazon.com Inc, Amazon Prime Air, 2016, URL: <<https://www.amazon.com/Amazon-Prime-Air/b?ie=UTF8&node=8037720011>>.
3. MarketsandMarkets, VTOL UAV Market By Application, Type, Propulsion, Payloads, Geography - Global Forecast to 2020, URL: <<http://www.marketsandmarkets.com/PressReleases/vtol-uav.asp>>.
4. Connor, M., Piloted, Electric Propulsion-Powered Experimental Aircraft Underway, NASA Armstrong Flight Research Center, Edwards AFB, CA, 2016, URL: <<https://www.nasa.gov/centers/armstrong/features/sceptor.html>>.
5. Federal Aviation Administration, Instrument Procedures Handbook, US Department of Transportation, Oklahoma City, OK, 2015, URL: <[https://www.faa.gov/regulations\\_policies/handbooks\\_manuals/aviation/instrument\\_procedures\\_handbook/media/Chapter\\_2.pdf](https://www.faa.gov/regulations_policies/handbooks_manuals/aviation/instrument_procedures_handbook/media/Chapter_2.pdf)>.
6. Holden, J., Fast-Forwarding to a Future of On-Demand Urban Air Transportation, Uber Technologies Inc., Oct. 2016, URL: <<https://medium.com/@UberPubPolicy/fast-forwarding-to-a-future-of-on-demand-urban-air-transportation-f6ad36950ffa#.vblzo5i0n>>, retrieved Feb. 22, 2017.
7. DARPA Announces VTOL X-Plane Phase 2 Design, DARPA, Mar. 2016, URL: <<http://www.darpa.mil/news-events/2016-03-03>>, retrieved Feb. 22, 2017.
8. Tern Moves Closer to Full-Scale Demonstration of Unmanned VTOL Aircraft Designed for Small Ships, DARPA, Dec. 2015, URL: <<http://www.darpa.mil/news-events/2015-12-28>>, retrieved Feb. 22, 2017.
9. Connor, M., Piloted, Electric Propulsion-Powered Experimental Aircraft Underway, NASA Armstrong Flight Research Center, Edwards AFB, CA, 2016, URL: <<https://www.nasa.gov/centers/armstrong/features/sceptor.html>>, retrieved Jan. 22, 2017.
10. Alexander Schleicher GmbH & Co., Ash 31 Mi, Wasserkuppe, Germany, URL: <<http://www.alexander-schleicher.de/en/flugzeuge/ash-31-mi/>>, retrieved Jan. 23, 2017.
11. McIver, J. B., Cessna Skyhawk II/100 Performance Assessment, Temporal Images, Ormond, Victoria, Australia, 2003, URL: <<http://temporal.com.au/c172.pdf>>, retrieved Feb. 02, 2017.
12. Alexander Schleicher GmbH & Co., Boundary layer blowing, Wasserkuppe, Germany, URL: <<http://www.alexander-schleicher.de/en/service/technik/grenzschiichtausblasung/>>, retrieved Jan. 25, 2017.
13. Wikipedia, Eta (glider), URL: <[https://en.wikipedia.org/wiki/Eta\\_\(glider\)](https://en.wikipedia.org/wiki/Eta_(glider))>, retrieved Jan. 26, 2017.
14. NASA Armstrong Fact Sheet: Helios Prototype, NASA Armstrong Flight Research Center, Edwards AFB, CA, 2014, URL: <<https://www.nasa.gov/centers/armstrong/news/FactSheets/FS-068-DFRC.html>>.
15. Power Clouds Holdings Pte Ltd, Photovoltaics that make you fly: the Solar Impulse venture, Singapore, 2016, URL: <<http://www.powerclouds.com/index.php/photovoltaics-that-make-you-fly-the-solar-impulse-venture/>>, retrieved Feb. 05, 2017.
16. Solar Impulse, Our Adventure, Lausanne, Switzerland, 2016, URL: <<http://www.solarimpulse.com/adventure>>, retrieved Feb. 03, 2017.
17. What Parts do you Need to Build a Drone?, The Drone Info, 2015, URL: <<http://www.thedroneinfo.com/2015/06/06/what-parts-do-you-need-to-build-a-drone/>>.
18. Brushless motors - how they work and what the numbers mean, Drone Trest, 2014, URL: <<http://www.dronetrest.com/t/brushless-motors-how-they-work-and-what-the-numbers-mean/564>>.
19. Mikolajczak, C., Kahn, M., White, K., Long, R. T., "Lithium-ion Batteries Hazard and Use Assessment", Fire Protection Research Foundation, Quincy, MA, 2011, URL: <[http://www.prba.org/wp-content/uploads/Exponent\\_Report\\_for\\_NFPA\\_-\\_20111.pdf](http://www.prba.org/wp-content/uploads/Exponent_Report_for_NFPA_-_20111.pdf)>.
20. Wikipedia, Lithium Polymer Battery, URL: <[https://en.wikipedia.org/wiki/Lithium\\_polymer\\_battery](https://en.wikipedia.org/wiki/Lithium_polymer_battery)>.
21. Airport IQ 5010, Oakland County Intl Airport Master Record. GCR Incorporated, 2016, URL: <<http://www.gcr1.com/5010web/airport.cfm?Site=PTK&AptSecNum=3>>, retrieved Jan. 25, 2017.

22. Airport IQ 5010, Palo Alto Airport Master Record. GCR Incorporated, 2016, URL: <http://www.gcr1.com/5010web/airport.cfm?Site=PAO&AptSecNum=3>, retrieved Jan. 25, 2017.
23. Airport IQ 5010, San Carlos Airport Master Record. GCR Incorporated, 2016, URL: <http://www.gcr1.com/5010web/airport.cfm?Site=SQL&AptSecNum=3>, retrieved Jan. 25, 2017.
24. Airport IQ 5010, San Francisco Intl Airport Master Record. GCR Incorporated, 2016, URL: <http://www.gcr1.com/5010web/airport.cfm?Site=SFO&AptSecNum=3>, retrieved Jan. 25, 2017.
25. Airport IQ 5010, Norman Y Mineta San Jose Intl Airport Master Record. GCR Incorporated, 2016, URL: <http://www.gcr1.com/5010web/airport.cfm?Site=SJC&AptSecNum=3>, retrieved Jan. 25, 2017.
26. Roskam, J. (1985). *Airplane Design, Parts I-VIII*, Roskam Aviation and Engineering Corporation, Ottawa, KS, 1985.
27. “ZIPPY Flightmax 2200mAh 3S1P 25C”, Kwun Tong, Hong Kong, URL: [https://hobbyking.com/en\\_us/zippy-flightmax-2200mah-3s1p-25c.html](https://hobbyking.com/en_us/zippy-flightmax-2200mah-3s1p-25c.html), retrieved Jan. 13, 2017.
28. Schneider, B., “A Guide to Understanding LiPo Batteries”, Roger’s Hobby Center, Saginaw, MI, URL: <https://rogershobbycenter.com/lipoguide/>, retrieved Mar. 17, 2017.
29. “Raspberry Pi Zero W”, Raspberry Pi Foundation, Cambridge, UK, URL: <https://www.raspberrypi.org/products/pi-zero-w/>, retrieved Jan. 15 2017.
30. “PWM Tutorial”, Arduino LLC, Vancouver, Canada, URL: <https://www.arduino.cc/en/Tutorial/PWM>, retrieved Feb. 11, 2017.
31. “Pixy (CMUcam5)”, Charmed Labs, Austin, TX, 2017, URL: <http://charmedlabs.com/default/pixy-cmucam5/>, retrieved Mar. 16, 2017.
32. “About Debian”, www.debian.org, 2016, URL: <https://www.debian.org/intro/about>, retrieved Apr. 10, 2017.
33. “The complete suite of products from ARM”, ARM Holdings, Cambridge, UK, URL: <https://www.arm.com/products>, retrieved Apr. 10, 2017.
34. “Introducing PIXEL”, Raspberry Pi Foundation, Cambridge, UK, URL: <https://www.raspberrypi.org/blog/introducing-pixel/>, retrieved Apr. 10, 2017.
35. “Python 2.7.2 Release”, Python Software Foundation, Wilmore, DE, 2017, URL: <https://www.python.org/download/releases/2.7.2/>, retrieved Apr. 10, 2017.
36. Grieser, F., “PLA vs ABS: Filaments for 3D Printing Explained & Compared”, All About 3D Printing, 2016, URL: <https://all3dp.com/pla-abs-3d-printer-filaments-compared/>, retrieved Jan. 15, 2017.
37. “Strength - Toughness”, Department of Engineering, University of Cambridge, Cambridge, UK, 2002, URL: [http://www-materials.eng.cam.ac.uk/mpsite/interactive\\_charts/strength-toughness/basic.html](http://www-materials.eng.cam.ac.uk/mpsite/interactive_charts/strength-toughness/basic.html), retrieved Apr. 6, 2017.
38. “MakerGear M2 3D Printer Specs”, MakerGear, Beachwood, Ohio, URL: <https://www.makergear.com/products/m2>, retrieved Jan. 10, 2017.
39. Chapman, B. Shivan, D., Muraoka, M., and Vidolova, T., “Investigating Methods of Prototyping with ABS”, Olin College of Engineering, Needham, MA, 2014, URL: [https://benchapman4.files.wordpress.com/2014/05/teamabs\\_guidereport.pdf](https://benchapman4.files.wordpress.com/2014/05/teamabs_guidereport.pdf), retrieved May 6, 2017.
40. Roskam, J. *Airplane Design, Parts I-VIII*, Roskam Aviation and Engineering Corporation, Ottawa, KS, 1985.
41. XFOIL, Software Package, Ver. 6.99, Massachusetts Institute of Technology, Boston, MA, 2013.
42. MATLAB, Matrix Laboratory, Software Package, Ver. 9.2.0.538062 (R2017a), MathWorks, Natick, MA, 2017.
43. AVL, Athena Vortex Lattice, Software Package, Ver. 3.36, Massachusetts Institute of Technology, Boston, MA, 2017.
44. “NACA 44412 (naca4412-il)”, Airfoil Tools, URL: <http://airfoiltools.com/airfoil/details?airfoil=naca4412-il>.
45. Ziemian, C., Sharma, M., Ziemian, S., “Anisotropic Mechanical Properties of ABS Parts Fabricated by Fused Deposition Modelling”, Bucknell University, Lewisburg, PA, Duke University, Durham, NC, 2012, URL: <http://cdn.intechopen.com/pdfs/35261.pdf>.
46. Anon., “Matweb Material Property Data,” URL: [http://www.matweb.com/search/datasheet\\_print.aspx?matguid=67d8cd7c00a04ba29b618484f7ff7524](http://www.matweb.com/search/datasheet_print.aspx?matguid=67d8cd7c00a04ba29b618484f7ff7524).
47. Anon., “Alloy 2024 Sheet and Plate,” Alcoa Mill Products, URL: [https://www.arconic.com/mill\\_products/catalog/pdf/alloy2024techsheet.pdf](https://www.arconic.com/mill_products/catalog/pdf/alloy2024techsheet.pdf).
48. Mechanical Properties of Carbon Fibre Composite Materials, Fibre / Epoxy resin (120°C Cure), Performance Composites, Taunton, UK, URL: [http://www.performance-composites.com/carbonfibre/mechanicalproperties\\_2.asp](http://www.performance-composites.com/carbonfibre/mechanicalproperties_2.asp).
49. Raspbian, Software Package, Ver. 4.9, Cambridge, UK, 2017, URL: <https://www.raspberrypi.org/downloads/raspbian/>.
50. Python Software Foundation, “About Python”, Wilmington, DE, URL:

- <<https://www.python.org/about/gettingstarted/>>.
51. van Rossum, G., "A Brief Timeline of Python", , URL: <<http://python-history.blogspot.com/2009/01/brief-timeline-of-python.html>>.
  52. Python Software Foundation, "Integrated Development Environments", Wilmington, DE, URL: <<https://wiki.python.org/moin/IntegratedDevelopmentEnvironments>>.
  53. PuTTY, Software Package, Ver. 0.68, Cambridge, UK, URL: <<http://www.putty.org/>>.
  54. Userspace Xbox/Xbox360 Gamepad Driver for Linux, Ver. 0.8.8, Ruhnke, I., URL: <<https://pingus.seul.org/~grumbel/xboxdrv/>>.
  55. T-MOTOR, U7-V2.0 KV420, Jiangxi, China, 2017, URL: <<http://store-en.tmotor.com/goods.php?id=320>>.
  56. T-MOTOR, Flame 80A HV, Jiangxi, China, 2017, URL: <<http://store-en.tmotor.com/goods.php?id=372>>.
  57. Raspberry Pi Foundation, Raspberry Pi Model 3B, Cambridge, UK, 2017, URL: <<https://www.raspberrypi.org/products/raspberrypi-3-model-b/>>.
  58. Social Compare, RaspberryPI models comparison, 2017, URL: <<https://socialcompare.com/en/comparison/raspberrypi-models-comparison>>.
  59. GetFPV, Lumenier 4Power Quick Swap Power Distribution Board, Sarasota, FL, 2017, URL: <<https://www.getfpv.com/lumenier-4power-quick-swap.html>>.
  60. HobbyKing, Turnigy nano-tech 4000mah 4S 25~50C Lipo Pack w/XT-60, Kwun Tong, Hong Kong, 2017, URL: <[https://hobbyking.com/en\\_us/turnigy-battery-nano-tech-4000mah-4s-25-50c-lipo-pack-xt-60.html?\\_\\_store=en\\_us](https://hobbyking.com/en_us/turnigy-battery-nano-tech-4000mah-4s-25-50c-lipo-pack-xt-60.html?__store=en_us)>.
  61. Cooking Hacks, SX1272 LoRa Shield for Raspberry Pi-900/915 MHz, Zaragoza, Spain, 2015, URL: <<https://www.cooking-hacks.com/sx1272-lora-shield-for-raspberry-pi-900-mhz>>.

## Appendix A - FR Rendering

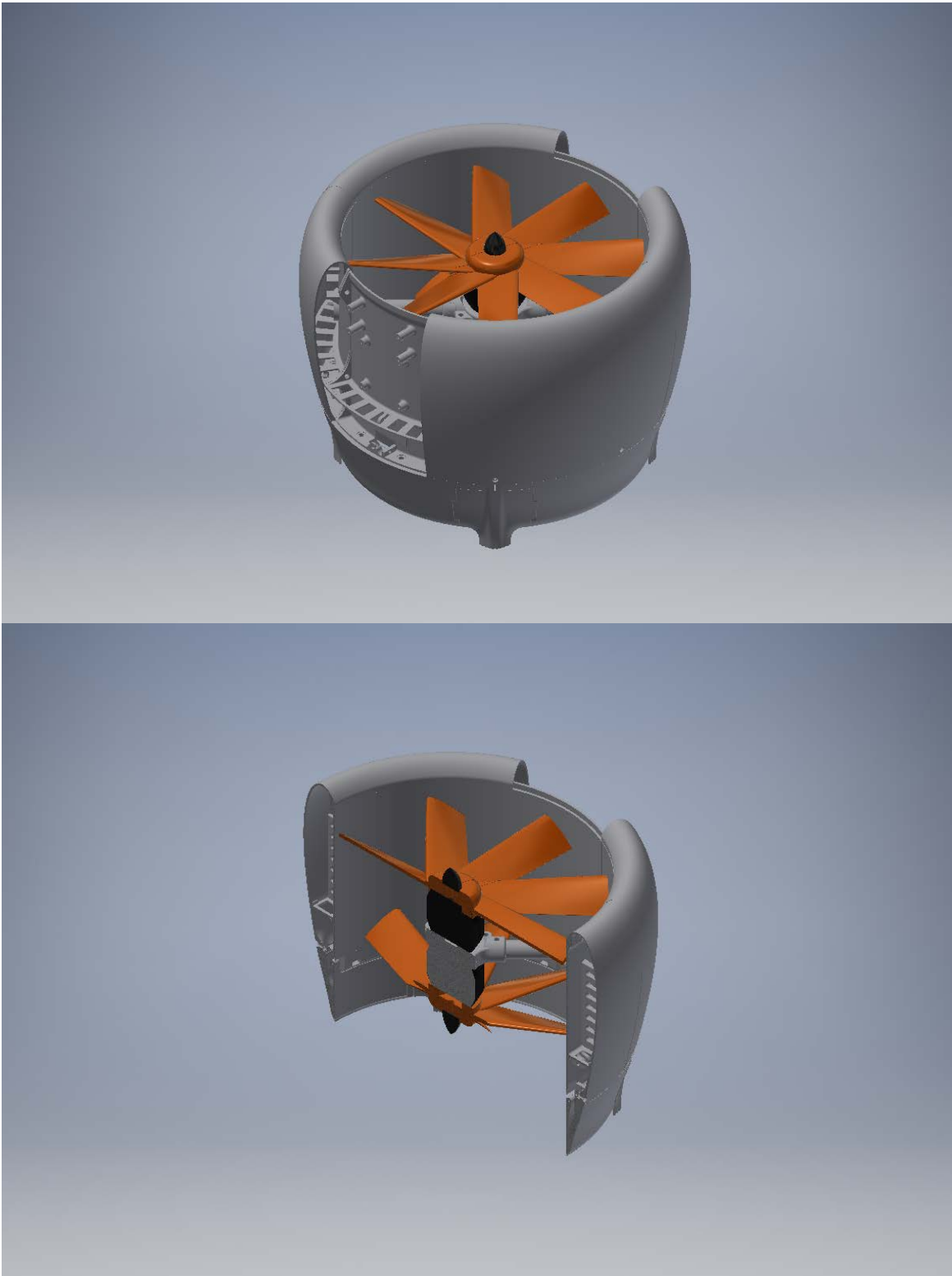


Figure A.1 - Orthographic rendering of the FR subsystem structure; full (top) and cross section (bottom). Note that the electronics and motors are not present in these drawings.

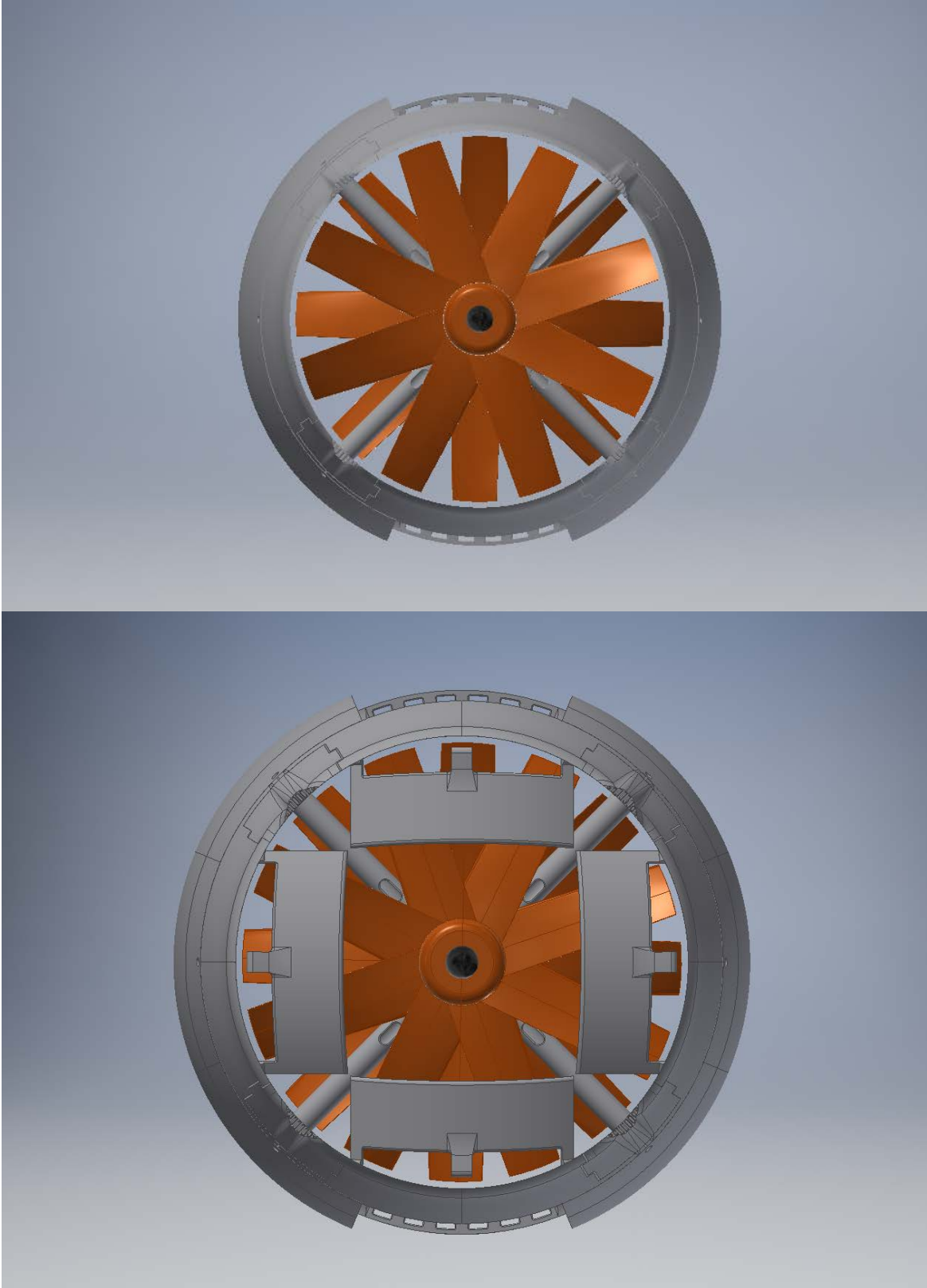


Figure A.2 - Bottom view rendering of the FR subsystem structure; flaps stowed (top) and deployed (bottom).

## Appendix B - FF Rendering

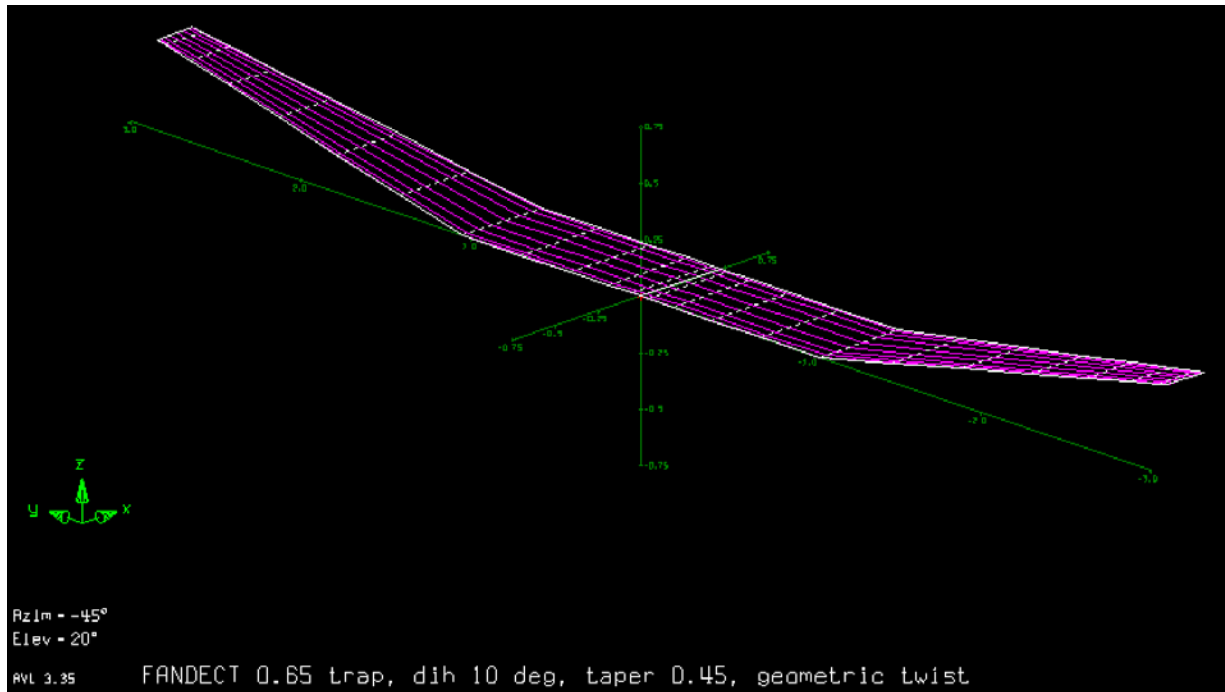


Figure B.1 - AVL geometric rendering of the FF subsystem lifting structure.

## Appendix C - Calculating FANDECT Wing Geometry with MATLAB

### Output

```
Re_root= 696829
Re_tip= 313573
b_dihedral= 5.9408
S= 2.2860
```

```
      x      y      z      c
      0      0      0  0.4680
      0  1.0500      0  0.4680
0.1287  2.9704  0.3386  0.2106
```

Elapsed time is 0.022199 seconds.

### Script

```
%% AE295, FANDECT
% AVL Parameters
% Gieser, Glen

%% Start
tic;clear all; clc

%% Constants
% Conversions
kg2lb = 2.2046; % convert kg to lb

% Air Properties
v = 22; % m/s, velocity
density_0 = 1.225; % kg/m^3, air density, 0 m MSL
density_304 = 1.19; % kg/m^3, air density, 304 m MSL
mu = 1.81e-5; % kg/(m s), dynamic viscosity, air, 15C
g = 9.81; % kg/m^2, gravity constant

% Wing Geometry
dihedral = 10; % deg, wing dihedral for trap. span
b = 6; % m, wingspan, full
b_half = b/2; % m, wingspan, half
b_trp = 0.65; % percent wing with trapezoidal profile
b_str = 1-b_trp; % percent wing with rectangular profile
taper = 0.45; % taper effect
c_r = 0.078*b; % m, chord, ro
c_t = c_r*taper; % m, chord, tip

b_dih = b-2*(b_half-b_half*b_str-b_half*b_trp*cosd(dihedral));
b_trp_dih = b_half*b_trp*cosd(dihedral);
S_half = b_half*b_str*c_r + b_trp_dih*(c_r+c_t)/2; % m^2, half wing surface area
S = S_half*2; % m^2, total wing surface area
AR = b_dih^2/S;

% Plot Geometry
Re_root = density_0*v*c_r/mu;
Re_tip = density_0*v*c_t/mu;
fprintf('Re_root=%10.0f\n',Re_root)
fprintf('Re_tip=%11.0f\n',Re_tip)
fprintf('b_dihedral=%7.4f\n',b_dih)
```

```

fprintf('S=%16.4f\n\n',S)
disp('      x      y      z      c')
x_avl = [0, 0, (c_r-c_t)/2];
y_avl = [0, b/2*b_str, b_dih/2];
z_avl = [0, 0, b_half*b_trp*sind(dihedral)];
c_avl = [c_r, c_r, c_t];

disp([x_avl,y_avl,z_avl,c_avl])

% Lift Estimation
c_l = 1.0071;          % NACA 4412, lift coefficient @aoa=5 degrees
L = 0.5*density_304*v^2*c_l*S; % N, lift generated

%% Stop
toc;

```

## Appendix D - FANDECT Wing Geometric Parameters for AVL

FANDECT 0.65 trap, dih 10 deg, taper 0.45, geometric twist

#Mach

0.0

#IYsym IZsym Zsym

0 0 0.0

#Sref Cref Bref

2.2860 0.3 5.9408

#Xref Yref Zref

0.0 0.0 0.0

#

#

#-----

SURFACE

Wing

#Nchordwise Cspace Nspanwise Sspace

8 1.0 12 1.0

#

YDUPLICATE

0.0

#

ANGLE

0.0

#

#-----

SECTION

#Xle Yle Zle Chord Ainc Nspanwise Sspace

0. 0. 0. 0.468 0.0 0 0

NACA

4412

#-----

SECTION

#Xle Yle Zle Chord Ainc Nspanwise Sspace

0. 1.05 0. 0.468 -0.5 0 0

NACA

4412

#-----

SECTION

#Xle Yle Zle Chord Ainc Nspanwise Sspace

0.1287 2.9704 0.3386 0.2106 -2.0 0 0

NACA

4412

## Appendix E - FR Script, Manual Mode

```
//main_v3: stability refinement, stability controls only work during thrust operation
//main_v2: integrate controls with sensors (yaw holding), store coefficients in matrices
//main_v1: combine control and sensor script
//imu_v4: desired xyz axis directions implemented, initial conditions refined
//imu_v3: rolling average & initial conditions implemented

//Control Libraries
#include <EnableInterrupt.h>
#include <Servo.h>
//Sensor Libraries
#include <Wire.h>
#include <Adafruit_BMP280.h>
#include <Adafruit_Sensor.h>
#include <OneWire.h>
#include "MPU9255.h"
#include <RunningAverage.h>
#define baudrate 115200

//Remote Control Definitions
#define RC_NUM_CHANNELS 4 // # of channels input
#define RC_CH1 0 // output for ch1_input
#define RC_CH2 1 // output for ch2_input
#define RC_CH3 2 // output for ch3_input
#define RC_CH4 3 // output for ch4_input
#define RC_CH1_INPUT A0 // analog pin for receiver ch3, front/back (pitch)
#define RC_CH2_INPUT A1 // analog pin for receiver ch1, left/right (roll)
#define RC_CH3_INPUT A2 // analog pin for receiver ch2, throttle
#define RC_CH4_INPUT A3 // analog pin for receiver ch4, yaw
//Delays
int dly[]={3000,1000,10}; // ESC initialization, pressure reading, end of loop
//PWM Definitions
int pwm[]={1000,1500,2000}; // PWM, servo min/center/max
int pwm_tol = 100; // PWM, dead zone tolerance at control stick origin
//Servo Definitions
Servo svo_front;
Servo svo_back;
Servo svo_right;
Servo svo_left;
int svo_pins[]={3,5,6,9}; // digital pin, output to svo front/back/right/left
int deg[]={87,0}; // degrees, servo min/max are confined by physical movement of FR flap
//Motor Definitions
Servo mtr_top;
Servo mtr_bottom;
int mtr_pins[]={10,11}; // digital pin, output to motor top/bottom
float asym = 0.925; // asymmetric RPM constant to balance motors
int deg_mtr[]={30,40,179}; // deg, motor stop/min/max signal
int deg_yaw[]={0,9}; // deg, yaw min/max signal
//Sensor Definitions
int svo_val[4][2]={{0,0},{0,0},{0,0},{0,0}}; // servo (rows:front,back,right,left) values (columns:remote
signal,drift/tilt hold): determines required flap angle
int mtr_val[2][3]={{0,0,0},{0,0,0}}; // motor (rows:top,bottom) values (columns:remote signal thrust,remote
signal yaw,yaw adjust,yaw hold): determines required motor RPM
int mtr_sum[]={0,0}; // sum of mtr_val row 1&2 columns
//Sensor Tolerance
```

```

const float a_tol[]={0.03,0.03,0.03};    // tolerable range for ax,ay,az
const float a_adj[]={5.0,5.0,1.0};      // corrective adjustment for ax,ay,az
const float w_tol[]={3.0,3.0,3.0};      // tolerable range for wx,wy,wz
const float w_adj[]={5.0,5.0,1.0};      // corrective adjustment for wx,wy,wz
//Remote Control Definitions
int prty_val[]={0,0,0};                // matrix holding pitch/roll/thrust/yaw signals
uint16_t rc_values[RC_NUM_CHANNELS];
uint32_t rc_start[RC_NUM_CHANNELS];
volatile uint16_t rc_shared[RC_NUM_CHANNELS];

//SENSOR DEFINITIONS
//Axis Direction Assignment
const float a_axis[]={-1,1,1};        //xyz accel direction. align to +x fwd, +y right, +z down output
const float w_axis[]={1,-1,-1};      //pitch roll yaw direction. align to +y up, +x right, +z right output
//Sensor Definitions
int16_t accelCount[3];
int16_t gyroCount[3];
int16_t magCount[3];
int16_t tempCount;
float f_accelCount[3];
float f_gyroCount[3];
float f_magCount[3];
float AccelScale, GyroScale, MagScale;
float temperature;
int doklG = 250;                       // degrees/sec, accuracy for gyro sensor
int doklA = 2;                          // +- 2g - accuracy for accelerometer
int doklM = 6;                          // 0.6 mGauss - accuracy for magnetometer
float approxGndPress;
Adafruit_BMP280 bmp;
MPU9255 mpu(12, doklG, doklA, doklM);
//Initial Sensor Condition Variables
const float d_a[3]={0.045,-0.015,-0.05}; //ax,ay,az
const float d_w[3]={0.06,1.44,0.02};    //wx,wy,wz
const float d_m[3]={0,0,0};            //mx,my,mz
const float d_tpa[3]={0,0,8.9};        //temp,pressure,altitude
//Running Average Definitions
uint32_t RA1_size=4;                   //number of recent readings to average for accel, gyro, compass
RunningAverage ax(RA1_size);
RunningAverage ay(RA1_size);
RunningAverage az(RA1_size);
RunningAverage wx(RA1_size);
RunningAverage wy(RA1_size);
RunningAverage wz(RA1_size);
RunningAverage mx(RA1_size);
RunningAverage my(RA1_size);
RunningAverage mz(RA1_size);
uint32_t RA2_size=50;                   //number of recent readings to average for temp, pressure
RunningAverage temp(RA2_size);
RunningAverage pres(RA2_size);
RunningAverage alt(RA2_size);

//FUNCTIONS
//PWM Function, Read Input
//void rc_read_values() {
void rc_read_values() {
    noInterrupts();

```

```

memcpy(rc_values, (const void *)rc_shared, sizeof(rc_shared));
interrupts();
}

//Remote Control Function, Calculate Output
void calc_input(uint8_t channel, uint8_t input_pin) {
  if (digitalRead(input_pin) == HIGH) {
    rc_start[channel] = micros();
  }
  else {
    uint16_t rc_compare = (uint16_t)(micros() - rc_start[channel]);
    rc_shared[channel] = rc_compare;
  }
}
void calc_ch1() { calc_input(RC_CH1, RC_CH1_INPUT); }
void calc_ch2() { calc_input(RC_CH2, RC_CH2_INPUT); }
void calc_ch3() { calc_input(RC_CH3, RC_CH3_INPUT); }
void calc_ch4() { calc_input(RC_CH4, RC_CH4_INPUT); }

void setup(){
  //Comm
  Wire.begin();           // initialize I2C protocol
  TWBR = 24;
  Serial.begin(baudrate);

  //Control
  //Servo
  svo_front.attach(svo_pins[0]);
  svo_back.attach(svo_pins[1]);
  svo_right.attach(svo_pins[2]);
  svo_left.attach(svo_pins[3]);
  // Motor
  mtr_top.attach(mtr_pins[0]);
  mtr_bottom.attach(mtr_pins[1]);
  mtr_top.write(deg_mtr[0]);      // ESC arm command, 0 RPM
  mtr_bottom.write(deg_mtr[0]);   // ESC arm command, 0 RPM
  delay(dly[0]);                  // ESC initialization delay
  // Remote Control
  pinMode(RC_CH1_INPUT, INPUT);
  pinMode(RC_CH2_INPUT, INPUT);
  pinMode(RC_CH3_INPUT, INPUT);
  pinMode(RC_CH4_INPUT, INPUT);
  enableInterrupt(RC_CH1_INPUT, calc_ch1, CHANGE);
  enableInterrupt(RC_CH2_INPUT, calc_ch2, CHANGE);
  enableInterrupt(RC_CH3_INPUT, calc_ch3, CHANGE);
  enableInterrupt(RC_CH4_INPUT, calc_ch4, CHANGE);

  //Sensor
  mpu.initMPU9250();             // initialize accelerometer/gyroscope
  float magCalibration[3];
  mpu.initAK8963(magCalibration); //initialize magnetometer
  if (!bmp.begin()){
    Serial.println("Pressure Sensor (BMP280) not present.");
    while (1);
  }
  for(int i=0;i<5;i++){

```

```

    approxGndPress+=bmp.readPressure();
    delay(dly[1]);
}
approxGndPress/=5;
switch (dokIG){
    case 250: GyroScale = 131.0; break;
    case 500: GyroScale = 65.5; break;
    case 1000: GyroScale = 32.8; break;
    case 2000: GyroScale = 16.4; break;
    default: GyroScale = 131.0; break;}
switch (dokIA){
    case 2: AccelScale = 16384.0; break;
    case 4: AccelScale = 8192.0; break;
    case 8: AccelScale = 4096.0; break;
    case 16: AccelScale = 2048.0; break;
    default: AccelScale = 16384.0; break;}
switch (dokIM){
    case 6: MagScale=0.6; break;
    case 15: MagScale=0.15; break;
    default: MagScale =1; break;}
//Running Average
ax.clear();ay.clear();az.clear();
wx.clear();wy.clear();wz.clear();
mx.clear();my.clear();mz.clear();
temp.clear();pres.clear();alt.clear();
}

void loop(){
//SENSOR: Acceleration (xyz g's), Angular Velocity (xyz deg/s), Magnetic Direction, Temperature, Pressure,
Altitude
mpu.readAccelData(f_accelCount);
mpu.readGyroData(f_gyroCount);
mpu.readMagData(f_magCount);
temp.addValue(mpu.readTempData()+d_tpa[0]);
pres.addValue(bmp.readPressure()+d_tpa[1]);
alt.addValue(bmp.readAltitude(1019.0)+d_tpa[2]);
for (int i=0;i<3;i++) f_accelCount[i]/=AccelScale;
for (int i=0;i<3;i++) f_gyroCount[i]/=GyroScale;
for (int i=0;i<3;i++) f_magCount[i]/=MagScale;
ax.addValue(a_axis[0]*f_accelCount[0]+d_a[0]);
ay.addValue(a_axis[1]*f_accelCount[1]+d_a[1]);
az.addValue(a_axis[2]*f_accelCount[2]+d_a[2]);
wx.addValue(w_axis[0]*f_gyroCount[0]+d_w[0]);
wy.addValue(w_axis[1]*f_gyroCount[1]+d_w[1]);
wz.addValue(w_axis[2]*f_gyroCount[2]+d_w[2]);
mx.addValue(f_magCount[0]+d_m[0]);
my.addValue(f_magCount[1]+d_m[1]);
mz.addValue(f_magCount[2]+d_m[2]);
float a_avg[]={ax.getAverage(),ay.getAverage(),az.getAverage()};
float w_avg[]={wx.getAverage(),wy.getAverage(),wz.getAverage()};
float m_avg[]={mx.getAverage(),my.getAverage(),mz.getAverage()};
float tpa_avg[]={temp.getAverage()/100,pres.getAverage()/100,alt.getAverage()};
float direction=atan2(m_avg[1],m_avg[0]);
if(direction<0) direction+=2*PI;
float direction_deg = direction * 180/PI;

```

```

//CONTROL
rc_read_values();
prty_val[0]=rc_values[0]; //pitch
prty_val[1]=rc_values[1]; //roll
prty_val[2]=rc_values[2]; //throttle
prty_val[3]=rc_values[3]; //yaw

//Controller Input
//Pitch
if(abs(prty_val[0]-pwm[1])>=pwm_tol){
//Pitch Down (svo_val: flap input,long/pitch hold)
if (prty_val[0]>=pwm[1]+pwm_tol){
svo_val[0][0] = map(prty_val[0], pwm[1]+pwm_tol, pwm[2], deg[0], deg[1]);
svo_val[1][0] = deg[0];
}
//Pitch Up
else if (prty_val[0]<=pwm[1]-pwm_tol){
svo_val[0][0] = deg[0];
svo_val[1][0] = map(prty_val[0], pwm[0], pwm[1]-pwm_tol, deg[1], deg[0]);
}
}
else{
svo_val[0][0]=deg[0];
svo_val[1][0]=deg[0];
}

//Roll
if(abs(prty_val[1]-pwm[1])>=pwm_tol){
//Roll Right: (svo val: flap input,lat/roll hold)
if (prty_val[1]>=pwm[1]+pwm_tol){
svo_val[2][0] = map(prty_val[1], pwm[1]+pwm_tol, pwm[2], deg[0], deg[1]);
svo_val[3][0] = deg[0];
}
//Roll Left
else if (prty_val[1]<=pwm[1]-pwm_tol){
svo_val[2][0] = deg[0];
svo_val[3][0] = map(prty_val[1], pwm[0], pwm[1]-pwm_tol, deg[1], deg[0]);
}
}
else{
svo_val[2][0]=deg[0];
svo_val[3][0]=deg[0];
}

//Thrust
if(prty_val[2]>=pwm[0]+pwm_tol){
mtr_val[0][0] = map(prty_val[2], pwm[0]+pwm_tol, pwm[2], deg_mtr[1], deg_mtr[2]);
mtr_val[1][0] = mtr_val[0][0]*asym;

//Yaw
if(abs(prty_val[3]-pwm[1])>=pwm_tol){
//Yaw Right Input
if (prty_val[3]>=pwm[1]+pwm_tol){
mtr_val[0][1]=0;
mtr_val[1][1]=-map(prty_val[3], pwm[1]+pwm_tol, pwm[2], deg_yaw[0], deg_yaw[1]);
}
}
}

```

```

//Yaw Left Input
else if (prty_val[3]<=pwm[1]-pwm_tol){
  mtr_val[0][1]=-map(prty_val[3], pwm[1]-pwm_tol, pwm[0], deg_yaw[0], deg_yaw[1]);
  mtr_val[1][1]=0;
}
}
else{
  mtr_val[0][1]=0;
  mtr_val[1][1]=0;
}

```

```

//Thrust (Dependent on Yaw)
mtr_sum[0]=mtr_val[0][0]+mtr_val[0][1];
mtr_sum[1]=mtr_val[1][0]+mtr_val[1][1];
if (mtr_sum[0]>deg_mtr[2] || mtr_sum[1]>deg_mtr[2]){
  if(mtr_sum[0]>mtr_sum[1]){
    mtr_sum[0]=deg_mtr[2];
    mtr_sum[1]=deg_mtr[2]-abs(mtr_sum[0]-mtr_sum[1]);
  }
  else if(mtr_sum[0]<mtr_sum[1]){
    mtr_sum[0]=deg_mtr[2]-abs(mtr_sum[0]-mtr_sum[1]);
    mtr_sum[1]=deg_mtr[2];
  }
}
else if (mtr_sum[0]<deg_mtr[1] || mtr_sum[1]<deg_mtr[1]){
  if(mtr_sum[0]>mtr_sum[1]){
    mtr_sum[0]=deg_mtr[1]+abs(mtr_sum[0]-mtr_sum[1]);
    mtr_sum[1]=deg_mtr[1];
  }
  else if(mtr_sum[0]<mtr_sum[1]){
    mtr_sum[0]=deg_mtr[1];
    mtr_sum[1]=deg_mtr[1]+abs(mtr_sum[0]-mtr_sum[1]);
  }
}
}

```

```

//Auto Stability
//Front&Back Hold
if (abs(prty_val[0]-pwm[1])<pwm_tol){
  //Longitudinal Drift Check
  if (abs(a_avg[0])>=a_tol[0]){
    svo_val[0][0]=deg[0];
    svo_val[1][0]=deg[0];
    //Stop Longitudinal Drift Front
    if(a_avg[0]>=a_tol[0]){
      if(svo_val[0][1]<0){
        svo_val[0][1]+=a_adj[0];
        svo_val[1][1]=0;
      }
      else if (svo_val[0][1]>=0){
        svo_val[0][1]=0;
        if (svo_val[1][1]-a_adj[0]<=deg[1]-deg[0]) svo_val[1][1]=deg[1]-deg[0];
        else svo_val[1][1]=-a_adj[0];
      }
    }
  }
  //Stop Longitudinal Drift Back

```

```

else if (a_avg[0]<=-a_tol[0]){
  if (svo_val[1][1]<0){
    svo_val[0][1]=0;
    svo_val[1][1]+=a_adj[0];
  }
  else if (svo_val[1][1]>=0){
    svo_val[1][1]=0;
    if(svo_val[0][1]-a_adj[0]<=deg[1]-deg[0]) svo_val[0][1]=deg[1]-deg[0];
    else svo_val[0][1]=-a_adj[0];
  }
}
}
//Pitch Drift Check
if (abs(w_avg[1])>=w_tol[1]){
  svo_val[0][0]=svo_val[0][0];
  svo_val[1][0]=svo_val[1][0];
  //Stop Pitch Down
  if(w_avg[1]>=w_tol[1]){
    if(svo_val[0][1]<0){
      svo_val[0][1]+=w_adj[1];
      svo_val[1][1]=0;
    }
    else if (svo_val[0][1]>=0){
      svo_val[0][1]=0;
      if (svo_val[1][1]-w_adj[1]<=deg[1]-deg[0]) svo_val[1][1]=deg[1]-deg[0];
      else svo_val[1][1]=-w_adj[1];
    }
  }
  //Stop Pitch Up
  else if (w_avg[1]<=-w_tol[1]){
    if (svo_val[1][1]<0){
      svo_val[0][1]=0;
      svo_val[1][1]+=w_adj[1];
    }
    else if (svo_val[1][1]>=0){
      svo_val[1][1]=0;
      if(svo_val[0][1]-w_adj[1]<=deg[1]-deg[0]) svo_val[0][1]=deg[1]-deg[0];
      else svo_val[0][1]=-w_adj[1];
    }
  }
}
}
}

//Right&Left Hold
if(abs(prty_val[1]-pwm[1])<pwm_tol){
  //Lateral Drift Check
  if (abs(a_avg[1])>=a_tol[1]){
    svo_val[2][0]=deg[0];
    svo_val[3][0]=deg[0];
    //Stop Lateral Drift Right
    if(a_avg[1]>=a_tol[1]){
      if(svo_val[2][1]<0){
        svo_val[2][1]+=a_adj[1];
        svo_val[3][1]=0;
      }
      else if (svo_val[2][1]>=0){

```

```

    svo_val[2][1]=0;
    if (svo_val[3][1]-a_adj[1]<=deg[1]-deg[0]) svo_val[3][1]=deg[1]-deg[0];
    else svo_val[3][1]=-a_adj[1];
  }
}
//Stop Lateral Drift Left
else if (a_avg[1]<=-a_tol[1]){
  if (svo_val[3][1]<0){
    svo_val[2][1]=0;
    svo_val[3][1]+=a_adj[1];
  }
  else if (svo_val[3][1]>=0){
    svo_val[3][1]=0;
    if(svo_val[2][1]-a_adj[1]<=deg[1]-deg[0]) svo_val[2][1]=deg[1]-deg[0];
    else svo_val[2][1]=-a_adj[1];
  }
}
}
//Roll Drift Check
if (abs(w_avg[0])>=w_tol[0]){
  svo_val[2][0]=svo_val[2][0];
  svo_val[3][0]=svo_val[3][0];
  //Stop Roll Right
  if(w_avg[0]>=w_tol[0]){
    if(svo_val[2][1]<0){
      svo_val[2][1]+=w_adj[0];
      svo_val[3][1]=0;
    }
    else if (svo_val[2][1]>=0){
      svo_val[2][1]=0;
      if (svo_val[3][1]-w_adj[0]<=deg[1]-deg[0]) svo_val[3][1]=deg[1]-deg[0];
      else svo_val[3][1]=-w_adj[0];
    }
  }
}
//Stop Roll Left
else if (w_avg[0]<=-w_tol[0]){
  if (svo_val[3][1]<0){
    svo_val[2][1]=0;
    svo_val[3][1]+=w_adj[0];
  }
  else if (svo_val[3][1]>=0){
    svo_val[3][1]=0;
    if(svo_val[2][1]-w_adj[0]<=deg[1]-deg[0]) svo_val[2][1]=deg[1]-deg[0];
    else svo_val[2][1]=-w_adj[0];
  }
}
}
}
}

//Yaw Hold
if (abs(prty_val[3]-pwm[1])<pwm_tol){
  //Stop Yaw
  mtr_val[0][1] = 0;
  mtr_val[1][1] = 0;
  //Stop Yaw Right (cw)
  if(w_avg[2]>=w_tol[2]){

```

```

    mtr_val[0][2]+=-w_adj[2];
    mtr_val[1][2]+=-w_adj[2];
  }
  //Stop Yaw Left (ccw)
  else if(w_avg[2]<=-w_tol[2]){
    mtr_val[0][2]+=-w_adj[2];
    mtr_val[1][2]+=-w_adj[2];
  }
}
mtr_sum[0]=mtr_val[0][0]+mtr_val[0][1]+mtr_val[0][2];
mtr_sum[1]=mtr_val[1][0]+mtr_val[1][1]+mtr_val[1][2];
}
//No Thrust Input, No Control Response (mtr_val: thrust input,yaw input,yaw hold)
else{
  svo_val[0][1]=0;
  svo_val[1][1]=0;
  svo_val[2][1]=0;
  svo_val[3][1]=0;
  mtr_sum[0]=deg_mtr[0];
  mtr_sum[1]=deg_mtr[0];
}

//Send values to components
svo_front.write(svo_val[0][0]+svo_val[0][1]);
svo_back.write(svo_val[1][0]+svo_val[1][1]);
svo_right.write(svo_val[2][0]+svo_val[2][1]);
svo_left.write(svo_val[3][0]+svo_val[3][1]);
mtr_top.write(mtr_sum[0]);
mtr_bottom.write(mtr_sum[1]);

//Display
// Serial.print("\tCH1:\t"); Serial.print(prty_val[0]); Serial.print("\t");
// Serial.print("\tCH2:\t"); Serial.print(prty_val[1]); Serial.print("\t");
// Serial.print("\tCH3:\t"); Serial.print(prty_val[2]); Serial.print("\t");
// Serial.print("\tCH4:\t"); Serial.print(prty_val[3]);
// Serial.print("\tThrust Top\t"); Serial.print(mtr_sum[0]);
// Serial.print("\tThrust Btm\t"); Serial.println(mtr_sum[1]);
Serial.print("\tax\t"); Serial.print(a_avg[0],2);
Serial.print("\tay\t"); Serial.print(a_avg[1],2);
Serial.print("\taz\t"); Serial.print(a_avg[2],2);
Serial.print("\ta\t"); Serial.print(sqrt(sq(a_avg[0]) + sq(a_avg[1]) + sq(a_avg[2])),2);
Serial.print("\twx\t"); Serial.print(w_avg[0],2);
Serial.print("\twy\t"); Serial.print(w_avg[1],2);
Serial.print("\twz\t"); Serial.print(w_avg[2],2);
Serial.print("\tw\t"); Serial.print(sqrt(sq(w_avg[0]) + sq(w_avg[1]) + sq(w_avg[2])),2);
//Serial.print("\tmx\t"); Serial.print(m_avg[0],0);
//Serial.print("\tmy\t"); Serial.print(m_avg[1],0);
//Serial.print("\tmz\t"); Serial.print(m_avg[2],0);
Serial.print("\tdirection "); Serial.print(direction_deg,2);
Serial.print("\tT(C)\t"); Serial.print(tpa_avg[0],1);
Serial.print("\tP(hPa)\t"); Serial.print(tpa_avg[1],0);
Serial.print("\tAlt(m)\t"); Serial.println(tpa_avg[2],1);

delay(dly[2]);
}

```